Mechanics of Immersed Collision and Granular Systems

A Thesis

Submitted to the

Tata Institute of Fundamental Research, Mumbai

for the Degree of

DOCTOR OF PHILOSOPHY
IN PHYSICS

by

SUMIT KUMAR BIRWA

INTERNATIONAL CENTRE FOR THEORETICAL SCIENCES
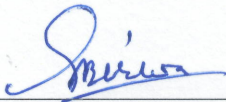TATA INSTITUTE OF FUNDAMENTAL RESEARCH
Bangalore − 560 089

August, 2019
Final version submitted: November, 2019
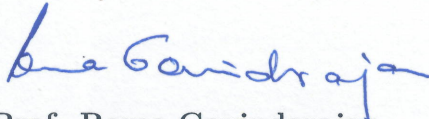
DECLARATION

This thesis is a presentation of my original research work. Wherever contributions of others are involved, every effort is made to indicate this clearly, with due reference to the literature, and acknowledgement of collaborative research and discussions.

The work was done under the guidance of **Prof. Rama Govindarajan** and **Prof. Narayanan Menon**, at the International Center for Theoretical Sciences, Tata Institute of Fundamental Research, Bengaluru, India.

Sumit Kumar Birwa

In my capacity as supervisor of the candidate's thesis, I certify that the above statements are true to the best of my knowledge.

Prof. Rama Govindarajan
Date: Novemeber 14, 2019

Prof. Narayanan Menon
Date: Novemeber 14, 2019

Acknowledgements

You will never know if you can fly, unless you take the risk of falling – Nightwing (*Secret Origins*).

I will like to start by thanking my parents Mr. Prakash Narayan Birwa and Mrs. Savitri Birwa for always believing in me and for trusting me to make my own life decisions. My brother Puneet Kumar Birwa and my sister-in-law Anshu Agarwal have been pillars of support throughout this journey and I will always be in debt to them for their help. And thank you Aarav (aka Dumbo) for always bringing a smile to my face with your antics.

Every superhero has an origin story and my story started when I first came in contact with Prof. Rama Govindarajan in 2011. She has been guiding me long before I even joined for Ph.D. She helped me every step of the way and made this journey much easier. My discussions with her about science and many other issues made me a better researcher and person. She will always be more than a Ph.D. advisor to me.

Unlike Nightwing [DC comic], I was lucky to have two advisors during this journey. Prof. Narayanan Menon is unlike any other person I have ever met. He introduced me to experimental physics and for that, I will be forever grateful to him. He was always there when I needed him for technical questions or Bihari dhaba's aaloo paratha. I learned a lot from every interaction I had with him. Rama and Narayanan are two of the sharpest and most humble people I have ever known, and always taught me a lesson on humility. On the scientific front, they taught me how to question everything and be particular in my approach.

I started working with Shubha Tewari in 2013 and she introduced me to the fascinating world of granular materials. I learned a lot while working with her. I am grateful for her encouragement and continuous support throughout this journey. I still remember my parents worrying a lot when I first traveled to the United States. They finally calmed down when I told them about Narayanan and Shubha and how helpful they are. On that note, I will also like to thank Kabir and Achala for their support and help. Bulbul Chakraborty has been an important part of my Ph.D. journey and I greatly benefited

from her guidance. It was a great learning experience working with Carl Merrigan, Nalini Easwar and Neil Shah.

Jason Ryan Picardo has been a friend and a mentor to me for the last two years. I still remember meeting him for the first time. He was wearing his signature Superman's attire. He has always pushed me to become better and his level of excellence is what I hope to achieve someday. I would like to thank him for helping me with me the work and codes. He was always ready for a scientific discussion. Our daily discussions on superheroes and cricket brought color to otherwise boring social life.

Dr. Ganga Prasath and soon to be Dr. Rahul Chajwa have been amazing lab mates, colleagues and more importantly friends throughout this journey. Doctorate students do not have an active social life, especially if you are living an hour away from the city. In such situations, your lab mates are your best friends and your confidante. Ganga and Rahul were more than anyone I could have hoped for. I am thankful to them for always being there for me and helping me in the lab.

G. Rajalakshmi was my mentor in my first two years of Ph.D. in TIFR Hyderabad. I learned a lot from her about experiments and analysis. She helped me a lot during my time in Hyderabad and without her guidance, I would not have been at this stage. I will also like to thank all my teachers on this journey — Vijaykumar Krishnamurthy, Samarjit Karmakar, Prasad Perlekar, Hari Dass, Subodh Shenoy, Sriram Ramaswamy. They all encouraged me to reach this goal. I also express my gratitude to Samriddhi Sankar Ray for his continuous support.

Sharath Jose has been a mentor and a friend in this journey. He was always there with constant words of encouragement and was ready to help. He is one of those people who always wants to help and will always ask if you need any help. I am grateful to Croor Singh for always being helpful and suggesting me to join TIFR Hyderabad. Manpreet Singh and Saaransh Singhal have been good friends and have helped me a lot with my work. Priyanka Maity has been a pillar of continuous support and a good friend. She was always there with suggestions and encouragement. Other friends who made my stay in TIFR Hyderabad and ICTS memorable are Ritabrata Singh, Rahul Gupta, Dheeraj Singh, Mohit Gupta, and Devang Falor. I will also like to express my gratitude to Anshul Deep Singh Parmar, Suraj Singh, Harsh Soni, Vinutha, Pankaj Popli, Rashmi Ramaadugu, Rayan Chatterjee, Shubhadeep Pal, and Debabrata for their help in my earlier years of Ph.D. and for being such good friends.

Deepak Kumar and Lee Walsh were more than colleagues in UMass. I greatly gained from being in their company. Both of them helped me in and out of the lab many times. Cooking with Deepak was always a great experience as my role was to sit on the couch

and wait for the food to be served. Vahini Reddy Nareddy is another important friend who made my time in the United States easier. I am also grateful to Zhejun Shen, Nuoya Zhou, Jooyoung Chang, Alyssa Conway and Guangfeng Yu for their help in UMass.

Synopsis

Motivation

Natural and industrial dense suspensions are studied by incorporating both lubrication force and frictional interaction between the particles while assuming these forces to be independent of each other. However, contact friction can only occur when physical contact has been made, and lubrication theory suggests that physical contact between the particles in a fluid takes infinite time with an exponentially decaying relative velocity. Therefore, to understand suspensions one needs to separately analyze collision dynamics between two spheres or a sphere and a wall in a viscous medium; the effect of contact friction in dry multi-particle systems, and then combine the understanding of both these interactions. This thesis presents an attempt to understand lubrication in a two-particle system and the role of frictional forces in a static many-body assembly of particles. In the next three sections, we will discuss the contact mechanics of normal collisions between a solid sphere and a bottom wall in a viscous medium and will seek to understand this dynamics both analytically and experimentally. After that we will investigate granular packing and the pressure variation in the bulk of a 2D granular column-filled with monodisperse frictional spheres, using numerical simulations. Finally, we will present an experimental study of granular packing in a 2D fluid-immersed system.

I will start by asking a very fundamental question: Is there solid-on-solid contact when a sphere falls toward a solid plane under gravity in a viscous medium. Normal collisions in a viscous medium involving curved surfaces have an inbuilt singularity of point contact, which makes it difficult to solve by traditional tools, either computationally or experimentally. Computationally one runs into the problem of grid size - the computational cost associated with resolving a contact is very high. Experimentally it is difficult to spatially and temporally resolve a contact during a collision. I will address this complicated problem first experimentally by using an electrical set-up and then analytically by developing a formulation that goes beyond lubrication theory, to compute hydrodynamic drag force on the sphere as it is approaching the bottom wall. Finally, I

will try to understand the electrical measurements taken earlier by tracking the sphere using a high-speed camera.

In granular systems, measuring pressure in the bulk is difficult experimentally. Usually one tries to infer the bulk pressure from measurements of stress on the wall, and by assuming the isotropy and homogeneity of stresses in the bulk. These assumptions might not always be true. Since granular systems are known to be history-dependent, the internal structure and stresses can depend on how the granular column was created. To test these assumptions, I use molecular dynamics simulations in Chapter 5 to measure stress in the bulk of a 2D granular column and see how these stresses vary by changing the protocols by which the granular column is created. I will also show that qualitatively different protocol-dependent stress profiles are possible in the bulk, though counter-intuitive. This work was done in collaboration with Professor Bulbul Chakraborty from Brandeis University.

Two-dimensional (2D) random packings of monodisperse spheres or disks are quite unstable and crystallize easily. For this reason, monodisperse disordered packings in a 2D system are not well-studied and bidisperse mixtures of spheres are often used in the granular community to study amorphous 2D systems. However, inter-particle friction can stabilize non-crystalline arrangements of grains. In Chapter 6, I will present an experimental protocol to create disordered packings of frictional, mono-disperse spheres in the 2D systems.

Is there a contact in normal collisions?

The circumstances under which collisions between solid particles occur in viscous fluids are relevant to many phenomena such as sedimentation, filtration, suspension flows, smoke, and fog formation by aerosols. To my knowledge, the first study of two-sphere collisions in a viscous fluid, where spheres were allowed to deform, was done by Davis et al. (1986) within an elastohydrodynamic framework. Working within the lubrication approximation, they suggested that pressure in the thin fluid film between the spheres is large enough to elastically deform them. The stored elastic strain energy is released as kinetic energy, causing the particles to rebound without solid-on-solid contact. This idea is hard to reconcile with our everyday experience with acoustic emission and dents when solids collide with each other, while immersed in a fluid.

To address the existence and influence of solid-on-solid contact in a sphere-wall collision in a viscous medium, we use an electrical setup to investigate kinematics very close to the moment of impact. It is now recognized that dynamics of such a collision is

controlled by the Stokes number St, which compares a particle's inertia to its viscous forces and is defined as (Gondret et al., 1999, 2002; Joseph et al., 2001; Zenit and Hunt, 1999):

$$St = \frac{1}{9}\frac{\rho_s v_c D}{\mu} = \frac{2}{9}\frac{\rho_s}{\rho_f} Re,$$ (1)

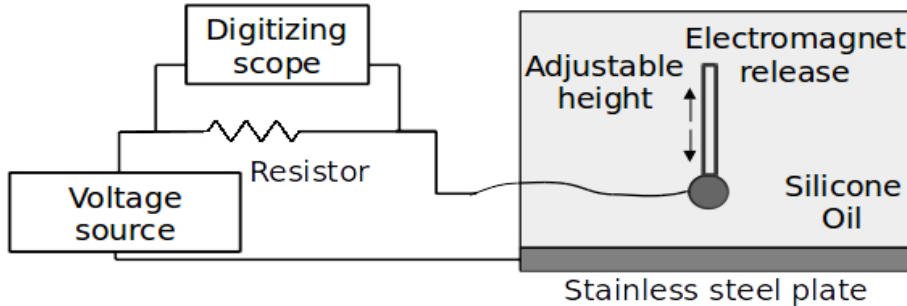where D, ρ_s, and Re are the diameter, density, and Reynolds number of the sphere

Fig. 1 Schematic diagram of the experimental set-up. The voltage is measured across a resistor (R_s) of 220 kΩ. Stokes number is varied by changing the height from which the sphere is being dropped.

and ρ_f and μ are the density and dynamic viscosity of the fluid respectively. Here v_c is the velocity the sphere would have had at $h_o = 0$, if the other body (another sphere or bottom wall) was not present. The elastohydrodynamic lubrication theory predicts a critical Stokes number St_c (Davis et al., 1986), below which a collision between smooth spheres does not result in a bounce, and the solids remain in contact. Experiments on sphere-wall collisions by Barnocky and Davis (1988), Gondret et al. (1999, 2002), Zenit and Hunt (1999), and Joseph et al. (2001) measure, by video imaging, the coefficient of restitution, which is the ratio of the velocity just after impact to the velocity just before impact. They found, by plotting the coefficient of restitution as a function of St, that there is a transition from settling to bouncing at St_c ranging from about 8 to 15. There is only a modest variation of St_c with the material of the sphere/wall as seen in the work of Gondret et al. (2002) and Zenit and Hunt (1999).

Surface roughness can play a role when the separation between the solids becomes comparable to roughness. Davis (1987) and Barnocky and Davis (1988) accounted for this theoretically by implementing an inelastic collision at a cutoff distance set by the roughness. Joseph et al. (2001) used spheres with well-characterized roughness and argued that the scatter in their data could be explained by surface roughness. Lecoq et al. (2004), Mongruel (2012), and Chastel and Mongruel (2016) concluded that artificial roughness can indeed increase the approach velocity before impact. Cawthorn and

Balmforth (2010) argue that an object falling under gravity will make contact with the bottom wall if the object has sharp roughness. Whether contact occurs before the
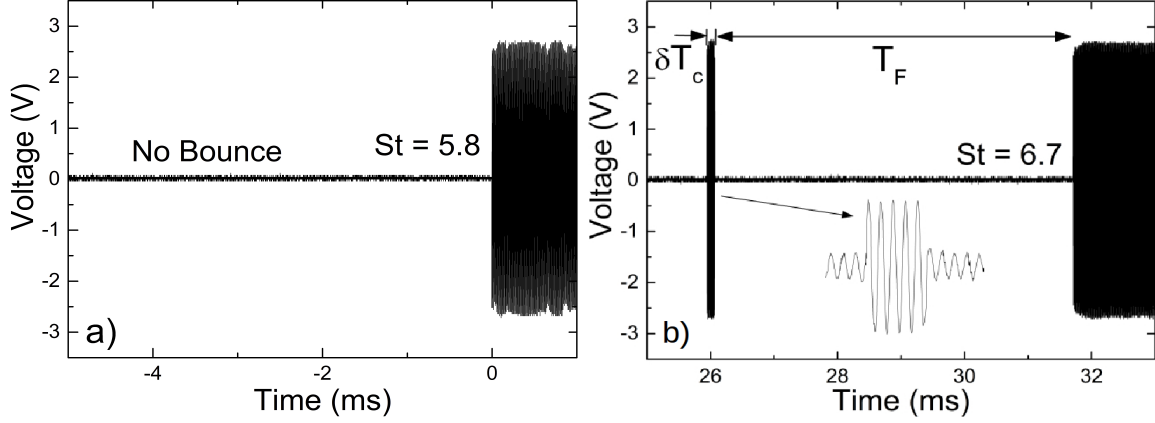

Fig. 2 Voltage versus time graphs for increasing St with AC and DC voltages. (a) At $St = 5.8$ with an AC applied voltage, no bounce occurs, but electrical contact is made in a finite time. This is the generic behavior for $St < St_c$. (b) At $St = 6.7$ with DC and AC voltages, respectively, we see a collision, and then a period of no contact, followed by permanent contact. The contact has much lower resistance than the series resistance i.e. $R_c \ll R_s$. This is the generic behavior for $St > St_c$ (Birwa et al., 2018).

rebound was still not completely established and understood. It is difficult with video techniques to resolve contact dynamics, spatially or temporally, as attempted in earlier works (Gondret et al., 1999, 2002; Joseph et al., 2001; Zenit and Hunt, 1999). So, we decided to answer this question using an electrical set-up where a conducting sphere was dropped on a conducting plate from a given height and a voltage was applied between them as shown in Figure 1. When the sphere makes (or breaks) electrical contact with the plate, the circuit closes (or opens). We observed that there is a critical Stokes number St_c for collision below which the sphere does not bounce and here the first electrical contact persists for all time as shown in Figure 2 (a). I will refer to this as the settling regime.

For larger values of St, as shown in Figure 2 (b), the ball makes metallic contact for a finite contact time δT_c. It then breaks contact and is in the fluid for a flight time T_F before settling into permanent electrical contact. I will refer to this as the bouncing regime. The sphere can have multiple bounces depending on the magnitude of St. The experiments were conducted using DC and AC supply and at different voltages. It was observed that all contacts (for both settling and bouncing regimes) were purely resistive and the duration of contact and other properties were found to be independent of the applied voltage.

The contact time δT_c decreases as the Stokes number is increased above St_c. The relatively small change of δT_c is consistent with the calculations for a Hertzian elastic impact, see Landau and Lifshitz (1986), which predicts a very weak dependence of contact time on velocity $\delta T_c \propto (UR_{eff})^{-1/5}$,where R_{eff} is the effective radius at the point of contact. For perfectly smooth spheres, $R_{eff} = R$, whereas R_{eff} will be smaller when a bump on the sphere is presented to the plane. The duration between the bounce and the next collision, which we refer to as the flight time, T_F, is a measure of the kinetic energy with which the ball rebounds from the plate. As expected, this is an increasing function of $St - St_c$. Our experiments not only resolve the question of contact but also provide information on the nature of the contact and the energy dissipation during such contacts.

We find a broad distribution of contact times, varying by an order of magnitude, for a fixed value of St. Presumably this reflects the variation in the local topography of the sphere (more information about the roughness of the spheres used, is in the thesis). We, however, find much smaller variability in the flight time, particularly at larger St. Thus the total energy dissipation in the sphere-wall encounter, as reflected by the flight time, is not strongly affected by the duration of solid-on-solid contact. This indicates that despite solid contact, the bulk of kinetic energy lost is due to fluid drag.

Even though solid dissipation does not play a prominent role, our result that solid-to-solid contact does occur is of significance in contexts such as wear, charge transfer, or chemical reactivity of solids in suspension. By analyzing the dent size, we also showed that the contact is not a result of a few asperities touching the surfaces.

An article describing the above findings has been published in *Physical Review Fluids* (Birwa et al., 2018)).

Going beyond lubrication theory

Our electrical measurements show that solid-on-solid contact does occur during a normal collision between a sphere and a wall in a viscous medium. However, elastohydrodynamic lubrication theory suggests that a sphere will rebound without making physical contact with the bottom wall. To understand the contradiction between our electrical measurements and theory, we revisited lubrication theory with a goal of releasing some of the assumptions it is based upon. Lubrication theory was derived by Reynolds (1886) and is used to obtain the pressure distribution across a thin film between two solid bodies. The theory exploits the disparity in the lateral and longitudinal length scales in the problem and as a consequence neglects the inertial terms in the Navier-Stokes equation. This leads to the theory obtaining a parabolic profile for the radial velocity between the two

solid bodies. The result is an equation for the radial pressure gradient commonly referred to as Reynolds's equation, which was a revolutionary equation in tribology, and can also be used for a normal collision between a sphere and a wall in a viscous medium. In the latter case, this equation may be used to update the vertical force, and therefore the dynamics. This problem is solvable analytically.
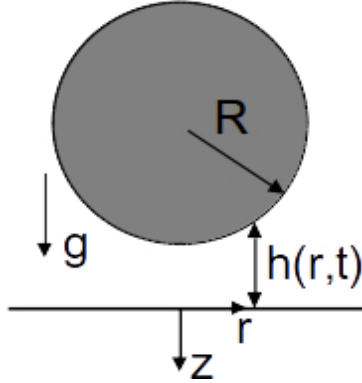

Fig. 3 A sphere approaching a plane, where r, z are the radial and vertical directions, $D = 2R$ is the diameter of the sphere, g is the acceleration due to gravity, and $h(r, t)$ is the time-dependent distance between sphere and the bottom wall.

For small $h(r = 0, t)$ (less than $\sim 0.01R$), this theory gives us the lubrication drag force also known as Taylor's formula:

$$F = \frac{6\pi\mu R^2}{h_o} \frac{dh_o}{dt} \tag{2}$$

where h_o is $h(r = 0, t)$, see Figure 3. This equation predicts that a falling sphere will approach the bottom wall infinitely slowly. While the decelerating force diverges as $h_o \to 0$, the velocity in the numerator also decreases, and the ratio produces this result.

From our daily experience, we know that a falling sphere does not take infinite time to make contact with the bottom wall and therefore, one needs to look closely at lubrication theory. In the lubrication approximation, streamwise gradients in everything except pressure are dropped, since they are assumed to be far smaller than gradients normal to the wall. In our current analysis (explained below), we retain streamwise gradients to the first order. In other words, we make a boundary layer approximation and allow for weak departures from the similarity profile of the velocity. Our approximation is still not valid for $r \sim O(h_o)$ or smaller, and when $r \sim R$. Since we are interested in the dynamics of the sphere when it is very close to the plate, h_o is very small, and the region $r \leq O(h_o)$ constitutes an extremely small fraction of the spherical area over which pressure acts. Its

force contributions can be neglected due to this, and also because the pressure maximum happens not to lie in this region. When $r \sim R$ too, the pressure contribution is very small because of the large gap size. Thus the region where $h_o \ll r \ll R$, gives most of the contribution to the pressure force. Our analysis describes the flow very well for this region. We obtain a single parametric differential equation which provides the velocity profiles at different radii at a given time. These are then used to solve for the pressure and the sphere's acceleration. By defining an appropriate non-orthogonal coordinate system, we are able to solve it as a succession of parametric ordinary differential equations.

We start with the axisymmetric Navier-Stokes equation written in cylindrical coordinates in terms of the streamfunction (ψ) and vorticity (ω), and non-dimensionalize it in a way that allows us to obtain solutions, which are not self-similar, for the radial velocity $u = \psi_z/2\pi r$ of the squeezed flow,

$$\eta = \frac{z}{h(r,t)}; \quad d\zeta = \frac{dr}{h(r,t)}; \quad t = t_d \frac{v_c}{R}; \quad \psi = \frac{\psi_d}{Q}; \quad \omega = \omega_d \frac{h}{U} = \frac{\omega_d}{f}, \qquad (3)$$

where Q is the flow rate and U is the average radial velocity at a given r and t.

After non-dimensionalization, we make the assumptions that h/R and r^2/R^2 are small. This is a fair assumption at $r \ll R$. Further, neglecting all except the first derivative in ζ, we get the final equation:

$$\left[\frac{h\dot{\zeta}}{\dot{h}_o} \psi_{\eta\eta\zeta} - \eta\psi_{\eta\eta\eta} + \frac{h}{\dot{h}_o}\psi_{t\eta\eta} + \left(\frac{\ddot{h}_o h}{\dot{h}_o^2} - 2 \right)\psi_{\eta\eta} - \frac{(h-h_o)}{rh}(\psi_\eta\psi_{\eta\eta\zeta} - \psi_\zeta\psi_{\eta\eta\eta}) \right.$$
$$\left. - \left(\frac{h'}{r}\frac{2h_o - h}{h} - \frac{2(h-h_o)}{r^2} \right)\psi_{\eta\eta}\psi_\eta + \frac{h'}{r}\psi\psi_{\eta\eta\eta} \right] = \frac{1}{Re}\left[\frac{1}{h\dot{h}_o}\psi_{\eta\eta\eta\eta} \right], \qquad (4)$$

where $Re = \rho_f v_c R/\mu$ and the dots represent partial or total derivatives in time. The boundary conditions for this equation are:

$$\psi(\eta = 0, \zeta, t) = 0; \quad \psi(\eta = 1, \zeta, t) = 1;$$
$$\psi_\eta(\eta = 0, \zeta, t) = 0; \quad \psi_\eta(\eta = 1, \zeta, t) = 0. \qquad (5)$$

Thus, apart from allowing for first-order variations in the streamwise direction, we explicitly include the effect of the acceleration of the body. These improvements constitute "going beyond" lubrication theory. We use a double shooting method, described in the thesis, for numerically solving equation 3.30, using which we compute the dynamics of the sphere.

This method provides a novel way to obtain the hydrodynamic force on the sphere without neglecting unsteady and inertial terms. The pressure profiles and force obtained are however similar to those obtained under the lubrication approximation. This is because we find that the deviations from a parabolic velocity profile are significant only at large r, where the contribution to upward pressure force is minimal. What then is causing the difference between theory and experiment? It will be shown in the thesis that even within the lubrication approximation, where pressure diverges as $h_o \to 0$, the velocity of approach is significant at height of the sphere as small as 1 nm, for large enough St. Based on this, one can argue that even a non-deformable sphere with an atomic-scale roughness should be expected to make contact with the plate, even going by the lubrication approximation. Besides this, other effects like those of higher-order streamwise derivatives, surface roughness, and deformation could be contributing.

Tracking the sphere

Our electrical experiments have shown that a sphere falling under gravity in a viscous medium will make physical contact with the bottom wall before bouncing, in contradiction to the elastohydrodynamic theory which suggests the sphere will rebound without making a physical contact with the bottom wall due to the heavy pressure build up in the gap between the two. To understand this discrepancy, we tracked the sphere just before and after it makes the contact with the bottom plate and observed deviations from the lubrication theory.

Earlier experiments done by Barnocky and Davis (1988), Gondret et al. (1999, 2002), Zenit and Hunt (1999), and Joseph et al. (2001) to understand the trajectory of the sphere before and after collision have used high-speed cameras, but have failed to resolve the near-collision dynamics. Lecoq et al. (1993) and Mongruel et al. (2010) tried to resolve the dynamics just before the collision for a settling sphere using interferometric techniques. But, there still remains a need to understand the dynamics, before and after the collision, in the bouncing regime. This led us to modify our previous experimental set-up and closely observe this part of the dynamics of the sphere.

We use our electrical set-up to trigger a high-speed camera. We observe a 1 mm dot marked on the sphere, as the sphere falls towards the bottom wall. When the sphere makes contact with the bottom wall, the electrical circuit is complete and a signal is sent to the high-speed camera. This signal triggers the camera, operating at 50000 frames/sec, to save a number of frames before and after this frame. We define the height at which the contact is initiated as the zero height. The Stokes number is varied by changing the

release height, which in turn affects the impact velocity. A sample trajectory is shown in Figure 4, and as can be seen, we are able to resolve up to a few micrometers above the bottom wall with the help of a macro lens and a bellow.

Using these trajectories, we obtain the variation of the vertical velocity with height and test for the ability of lubrication theory to obtain the dynamics. We observe that the lubrication theory correctly describes the experimental curves for a sphere approaching a plate up to $\sim 50\ \mu$m above the bottom wall. After that, lubrication theory predictions are seen to always lie below the experimental data, i.e., in experiments we observe the sphere to have a larger downward velocity at a given height compared to theory. These deviations become larger as the sphere advances towards the plate.
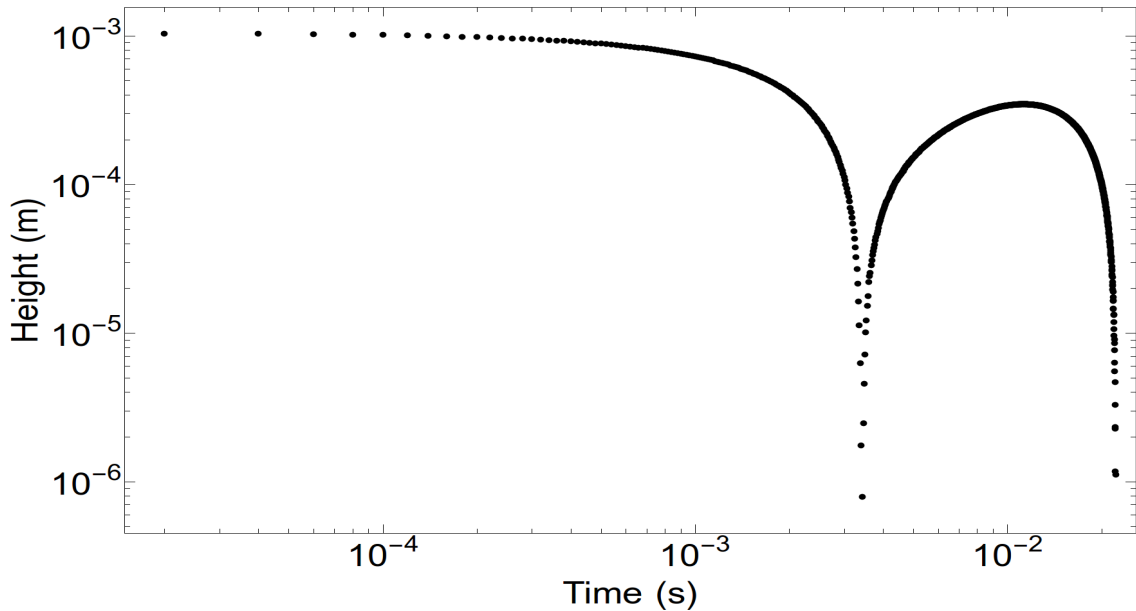

Fig. 4 A sample trajectory (height vs time) obtained for $St = 15$ by observing a dot of 1 mm on the sphere at 50000 frames/sec.

This experimental set-up allows us to track the sphere after collision too. It is comparatively easy to observe the rebound dynamics at larger St. The rebound trajectories for these large St, barring a small deviation at small heights (similar to first impact curves), follow the dynamics predicted by lubrication theory. The second impact dynamics for these St is similar to the dynamics of the first impact for smaller St. In fact, at large Stokes number, the approach curves for the second impact overlap with those of the first impact for a corresponding smaller Stokes number. This observation of rebound curves and second impact dynamics suggests that disturbances created due to first impact (or

rebound after the first impact) might not be important in such systems and die quite rapidly.

Stresses inside a granular column

Once the contact between the spheres is established, the friction between the surfaces takes over and it is important to study the structure that these frictional contacts can create and the stresses they carry as such structures are prevalent in the world at all scales. These structures are heavily controlled by frictional contacts and the literature on granular matter deals with such systems in zero resistance medium.

Stresses inside a static granular structure have been a subject of study for years now, see e.g. Nedderman (2005). Janssen (1895) showed that pressure at the bottom of a granular column, filled with grains, saturates with the fill-height of the container. He predicted that the vertical stress (σ_{yy}) for a 2D column at a height y decays exponentially with fill-height h and is given by:

$$\sigma_{yy}(y) = \frac{\rho g W}{2K\mu_w}(1 - e^{-\frac{2K\mu_w}{W}(h-y)}) \tag{6}$$

where g is the acceleration due to gravity, W is the width of the granular column, K is the ratio of the lateral to the vertical stress (Janssen's constant), μ_w is the coefficient of wall friction and ρ is the bulk density. This behavior of a granular column is different from that of a column filled with liquid. To test Janssen's prediction, the vertical stress at the bottom of a granular column has been widely documented for both 2D and 3D cases, see e.g. Vanel and Clément (1999), Vanel et al. (2000), Ovarlez et al. (2003), and Landry et al. (2003, 2004). Saturation of vertical stress, namely, no increase in σ_{yy} beyond a certain fill-height, has been observed at large heights. A common explanation for this saturation is that the walls of the column bear some of the load of the granular pile with the help of wall-friction. Hence, filling the container beyond a certain height merely increases the load on existing force chains and helps in creating new chains, while the load at the bottom of the container remains unaffected.

Despite a large number of studies on measuring pressure at the bottom of a granular pile, it is still not clear how the vertical stress varies with vertical coordinate in the bulk of the column. In particular, how close is it to Janssen's prediction? To understand this, we performed LAMMPS-based molecular dynamics simulations, (https://lammps.sandia.gov/) Plimpton (1995). LAMMPS is an open-source code which I have used in other studies too (Merrigan et al., 2018; Shah et al., 2017). The computa-
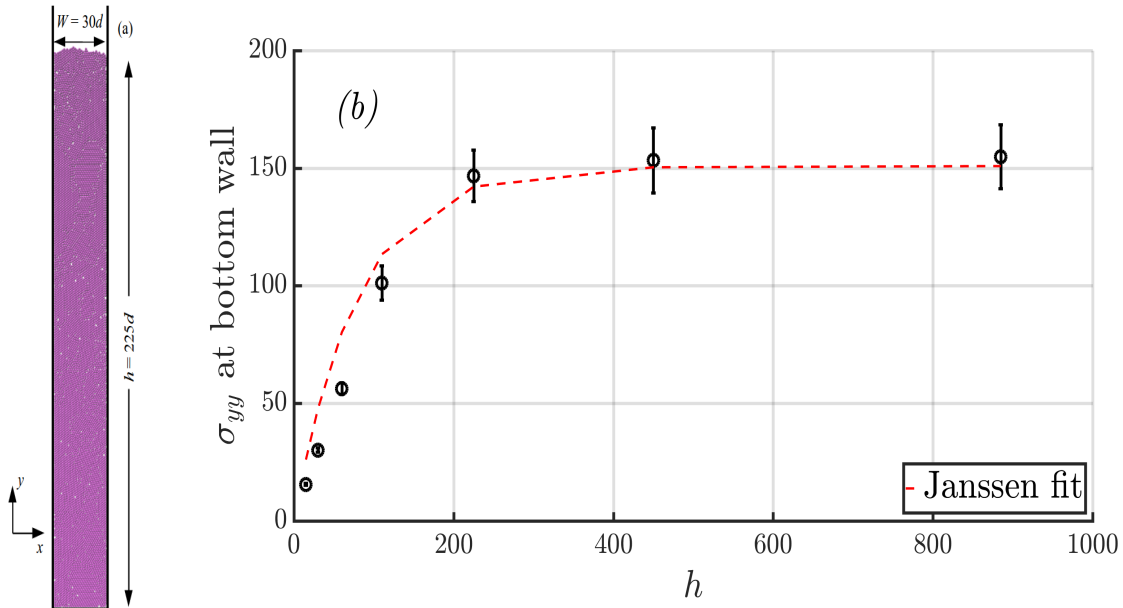
Fig. 5 (a) A sample geometry used in our quasi-2D computational study. The domain here has width $W = 30$, height $h = 225$, and is filled with ~ 7500 monodisperse soft spherical grains. Gravity is pointing downwards. Our analysis has been done on widths $W = 30, 60$ and 90 and heights $h = 225, 450$ and 900. (b) Vertical stress, σ_{yy}, on the bottom wall, created by the S2 method, as a function of fill-heights for $W = 30$ and μ_w $= 0.5$. Error bars are the standard deviation obtained by running 20 different ensembles at each height. The red dashed line is the best fit obtained by the Janssen model for a $K = 0.203$.

tional domain in the present study is a quasi-2D rectangular box as shown in Figure 5 (a) filled with monodisperse particles of diameter 1 and mass 1, i.e., all lengths and masses are measured in units of the diameter d and mass M, respectively. Stress has been non-dimensionalized by Mg/d^2. We construct our granular column in four different ways. S1, Sedimentation: Creating all the grains at once, randomly placing them in a non-overlapping fashion over the complete space within the column, and then letting them settle under gravity till the kinetic energy of the whole system becomes less than 10^{-12}. S2: We start in the same way as S1. But in this protocol, a high viscous damping force that is proportional to the velocity of the grains is applied to each particle to drain kinetic energy promptly, after the particles have settled under gravity for a while in vacuum. V1, Vibration: Vibrating the final S2 system laterally for some time and then letting it relax. P1, Pouring: Pouring a fixed number of grains from a fixed height above the granular column at fixed time intervals until the total number of grains in the column is equal to the desired value. One of the main assumptions in Janssen's theory is that all

the grains at the side-walls are fully mobilized. So, we studied the S2 protocol before and after mobilizing the grains.

All these protocols for creating the granular column are widely used in the literature (Landry et al., 2003, 2004) and we study how the stresses in the bulk vary in a 2D monodisperse system with these protocols. The vertical stress on the bottom wall agrees with the Janssen model for $K = 0.203$ as shown in Figure 5 (b). However, in the bulk different protocols give different vertical stress profiles, some representing significant departure from Janssen's model. These differences and the different types of static columns which emerge will be discussed in the thesis.

Immersed granular packing

The packing arrangements of multi-particle systems can be completely different inside a fluid and can depend on many parameters [like buoyancy forces and St, if the packing is created by sedimenting particles in a fluid (Farrell et al., 2010; Onoda and Liniger, 1990)]. This makes it interesting and important to understand how such packings come about and if it can be exploited to understand the jamming transition O'Hern et al. (2002).

In a two-dimensional system, the highest packing arrangement for spheres is obtained by hexagonal crystalline packing and the volume fraction is around $\phi_{hex} = 0.907$. A disordered or amorphous packing has a much smaller volume fraction. Random close packing, the largest disordered packing fraction achievable without introducing crystalline structures, is typically quoted for three dimensional systems to be ~ 0.64 (Bernal and Mason, 1960). However, the existence of disordered packing in a 2D system is a subject of debate as monodisperse 2D packings crystallize and therefore bidisperse spheres are used in the granular community to study the 2D systems.

We have developed an experimental protocol to create disordered packings of frictional, mono-disperse spheres in 2D systems. Our goal is to use the principles learned earlier in this thesis to deposit particles at Stokes numbers below a critical value, so that every new particle incident on a packing delivers no momentum to the particles beneath. In the protocol developed, spheres are allowed to roll downhill within a viscous fluid to create disordered packings as shown in Figure 6. The particles are scattered initially to occupy the whole space of the container. Then, one edge of the container is lifted slowly to a finite angle which allows particles to roll towards the opposite side and create a weakly packed structure. This method leads to packing with a nearly horizontal interface [Figure 6 (a)]. For obtaining a packing with an inclined interface as shown in [Figure 6

(b)], the particles, after being scattered, are first allowed to roll towards one of the longer sides and then towards the short side.
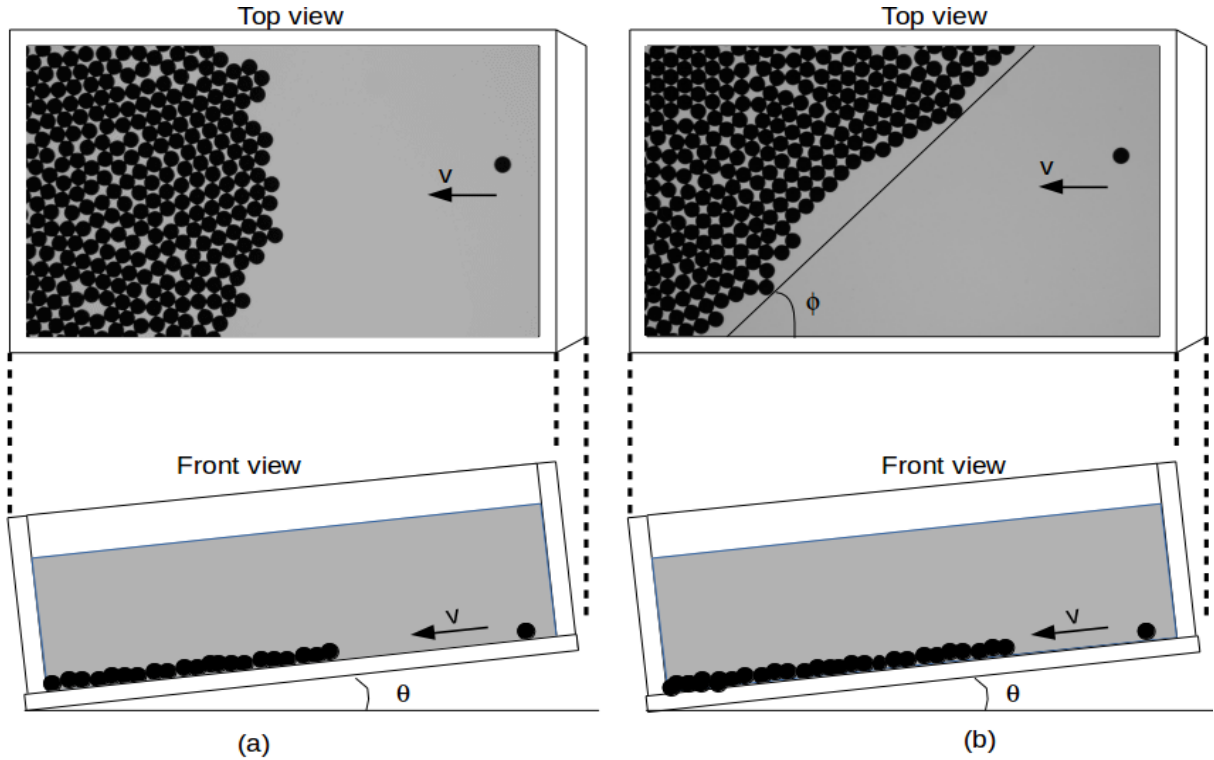

Fig. 6 Top and front view of two different types of immersed packing. Packing (a) and (b) are generated by different initial conditions. In both cases, the left side of the box is lower than the right side and particles settle under gravity to prepare the initial packing. Individual spheres are then rolled downhill to collide with the packing to study the disturbances created by such impacts.

Packing has been observed at four different inclination angles, θ, of the substrate: 5°, 7°, 10° and 15°. The packing density decreases with the lowering of this angle as shown in Figure 7. Here, the packing density has been measured using three different radii as we found out that determining the exact radius for hard particles in contact is difficult. How we choose these three radii has been discussed in detail in the thesis. In a further experiment, individual spheres are rolled downhill on a packing prepared either as in Figure 6 (a) or as in Figure 6 (b). To understand the stability of the packing, the spatial size of the resulting disturbance due to individual impacts was measured. Our data suggest that under these conditions of the impact, the collisions are below the critical Stokes number for rolling impacts. In this thesis, we study the disordered packings as a
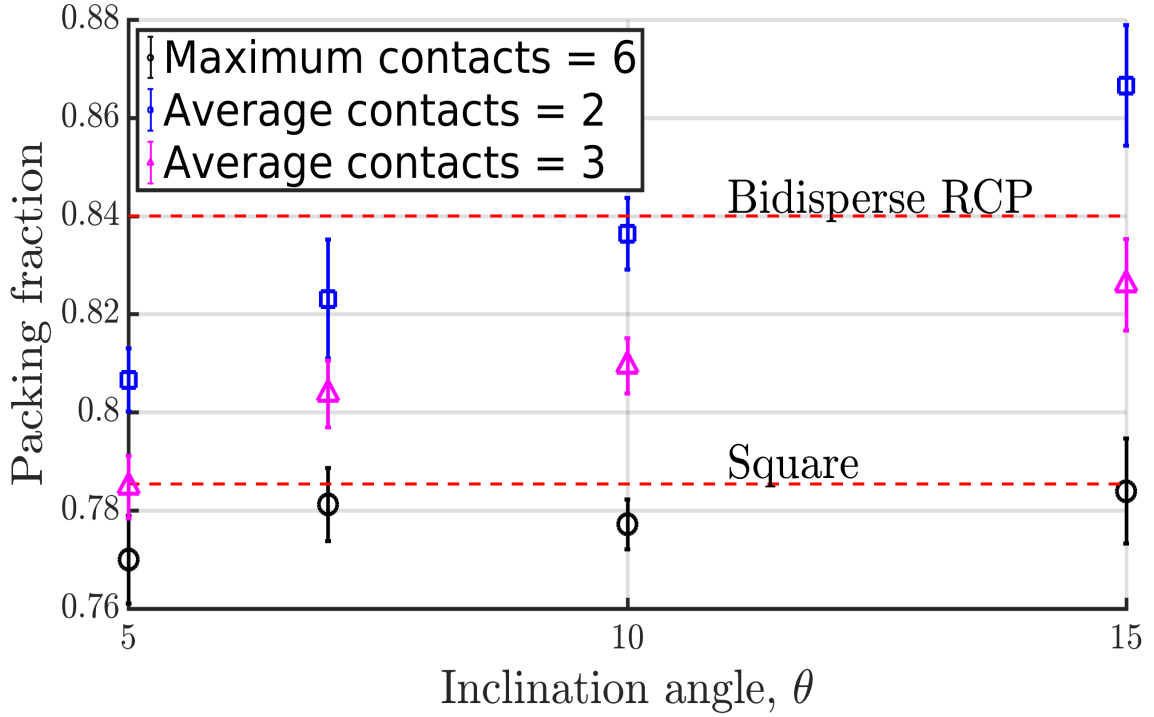
Fig. 7 Packing density is found to increase with the inclination angle, θ, of the box. The packing density has been measured for the packed structure with a horizontal interface by choosing three different radii. Black circle symbol corresponds to an average radius which gives only one particle with 6 contacts in the packing. Magenta triangle symbol and red square symbol corresponds to the radii at which the packing has coordination number = 2 and 3, respectively. Error bars are the standard deviations of packing densities measured from different trials at a fixed inclination angle.

function of deposition conditions and the changes in local packing following individual impacts.

Main findings

Immersed normal collision: In agreement with previous observations and with elastohydrodynamic theory, we found that there is indeed a critical Stokes number (around 7), marking the transition from settling regime to bouncing regime in immersed collisions. However, in contradiction with lubrication theory, we observed direct mechanical contact for 10-100 microseconds before bouncing. The duration of this contact was found to be independent of the experimental parameters and weakly dependent on impact velocity,

which is consistent with Hertzian elastic theory. From observing the scatter in contact times and flight times for different trials at each *St*, we concluded that the total dissipation in the sphere-wall encounter is not strongly affected by the duration of solid-on-solid contact at large Stokes number indicating that despite solid contact, most of the loss of kinetic energy in this process is due to fluid dissipation.

We analytically went beyond the lubrication theory by including unsteady terms and inertial terms, which were neglected in lubrication theory. We derived a boundary layer equation to describe the flow and solved it by a novel method. This allowed us to obtain the radial velocity profile below the sphere. However, the deviations in the net force from the lubrication theory were found to be very small and are not enough to explain our electrical measurements.

We also found that the actual approach velocity is slightly faster than predicted by lubrication theory at smaller heights by coupling a high-speed camera with our earlier electrical set-up. Rebound and second impact dynamics behavior were found to be similar to lubrication theory predictions, up to a point close to contact.

Granular packing: A numerical study in a mono-disperse 2D static granular column showed us that the bulk stress profile can be very different from Janssen's predictions depending on the aspect ratio of the column and the protocol followed to prepare the granular column.

Immersed packing: An experimental study of granular packing in an inclined 2D immersed system where monodisperse spheres roll downhill to create a disordered packing of grains showed us that the packing density decreases with the decrease in angle of inclination of the substrate. By observing individual spheres rolling downhill and colliding with the packing, we concluded that our experiment is below a critical Stokes number for rolling impacts as we do not see any rebound of impacting particles.

Table of contents

List of figures

List of tables

Publications

- S. K. Birwa, G. Rajalakshmi, R. Govindarajan, and N. Menon. Solid-on-solid contact in a sphere-wall collision in a viscous fluid. *Physical Review Fluids*, 3(4):044302, 2018.

- C. Merrigan, S. K. Birwa, S. Tewari, and B. Chakraborty. Ergodicity breaking dynamics of arch collapse. *Physical Review E*, 97(4):040901, 2018.

Preprint

- N. Shah, B. Carballo-Ramirez, S. K. Birwa, N. Easwar, and S. Tewari. Effect of wall friction on 2D hopper flow. *Granular Matter*, to be submitted.

Under preparation

- S. K. Birwa, N. Menon and R. Govindarajan. A boundary layer theory for near-collision dynamics of axisymmetric solids.

- S. K. Birwa, L. Lacaze, R. Govindarajan and N. Menon. High-speed imaging of near-collision dynamics.

- S. K. Birwa, B. Chakraborty and R. Govindarajan. Non-monotonic vertical stress in a 2D granular column.

- S. K. Birwa and N. Menon. Disordered packing in 2D immersed system.

Chapter 1

Introduction

1.1 Motivation

Natural and industrial liquid-solid flows like dense suspensions, landslides, sediment transport, etc. are studied by incorporating both lubrication force and frictional interaction between the particles, often assuming these forces to be independent of each other. However, contact friction can only occur when physical contact has been made, and lubrication theory suggests that physical contact between the particles in a fluid takes infinite time with an exponentially decaying relative velocity (Leal, 2007). Therefore, to understand the physics of such systems one needs to separately analyze (a) collision dynamics between two spheres or a sphere and a wall in a viscous medium, and (b) the effect of contact friction in dry multi-particle systems. Only thereafter both the interactions can be combined to study the coupling between the two. This thesis follows such an approach and presents an attempt to understand normal collision in a fluid-immersed two-particle system and the role of frictional forces in a static many-body assembly of particles in a medium of negligible resistance. Finally, we present an experimental study of multi-particle packing in a 2D fluid-immersed system.

This thesis thus revolves around two broad topics: immersed normal collisions (Chapters 2-4) and granular packing (Chapters 5-6). I start by asking a fundamental question: is there solid-on-solid contact when a sphere falls under gravity towards a solid plane in a viscous medium? Normal collisions involving curved surfaces in a viscous medium have an inbuilt singularity at the point of contact, which makes this problem difficult to solve using traditional tools, either computational or experimental. Computationally, one runs into the problem of grid size — the computational cost associated with resolving a contact event is very high. Experimentally, it is not trivial to spatially and temporally resolve a contact during a collision. I address this complicated

problem first experimentally by using an electrical set-up (described in Chapter 2). The problem is then approached analytically by developing a formulation that goes beyond lubrication theory to compute hydrodynamic drag force on the sphere as it is approaching the bottom wall (Chapter 3). Finally, I try to understand the electrical measurements obtained experimentally by tracking the sphere using a high-speed camera (shown in Chapter 4).

In granular systems, experimentally measuring pressure in the bulk is difficult. Usually one tries to infer the bulk pressure from measurements of stress on the wall, and by assuming isotropy and homogeneity of stresses in the bulk. However, these assumptions might not always be true. Since granular systems are known to be history-dependent, the internal structure and stresses can depend on how the granular column was created. To test these assumptions, I use molecular dynamics simulations in Chapter 5 to calculate stress in the bulk of a 2D granular column and see how these stresses vary on changing the protocols by which the granular column is created. For some protocols, we find stress-profiles which are counter-intuitive and does not follow Janssen's model (Janssen, 1895; Sperl, 2006).

Two-dimensional (2D) random packings of monodisperse spheres or disks are quite unstable and crystallize easily. For this reason, monodisperse disordered packings in a 2D system are not well-studied and bidisperse mixtures of spheres are often used in the granular community to study amorphous 2D systems. However, inter-particle friction is known to stabilize non-crystalline arrangements of grains (Dong et al., 2006; Farrell et al., 2010; Jerkins et al., 2008; O'Hern et al., 2002; Zhang et al., 2001). In Chapter 6, I will present an experimental protocol to create disordered packings of frictional, mono-disperse spheres in 2D systems.

1.2 Immersed collisions

The circumstances under which collisions between solid particles occur in a viscous fluid are relevant to many phenomena such as sedimentation, filtration, suspension flows, smoke, and fog formation by aerosols (Davis, 1984; Farrell et al., 2010; Gal et al., 1985; Löffler, 1980; Payatakes and Gradoń, 1980). Energy losses in particle collisions arise primarily either from viscous dissipation of the surrounding fluid or inelastic losses within the solids or both. Heinrich Hertz in 1882 studied the normal collision between two particles in an inviscid fluid. Hertz described the local stresses developed when two elastic curved surfaces come in contact under a given load (Landau and Lifshitz, 1986). This is famously known as Hertzian contact theory and can be used to obtain the contact

area and duration of contact for an elastic collision if the velocity of impact is known. Dahneke (1971, 1973) developed a particle beam apparatus to study inelastic collisions and determine the sticking probability and coefficient of restitution of particle collisions in a medium of negligible resistance. They found out that there is a critical velocity below which the coefficient of restitution is zero and the particle sticks to the substrate. Inter-particle adhesion plays a big role here (Dahneke, 1971, 1972, 1973; Löffler, 1980) and, therefore, the physics in these collisions is very different from what we will be discussing in this thesis.

1.2.1 Lubrication theory

Studies to understand collisions between rigid solids in a viscous fluid started by Reynolds (1886), who derived a differential equation to obtain the pressure distribution across a thin film between two solid bodies. The assumptions used in this derivation are referred to as the lubrication approximation and it proved to be a revolutionary idea in the field of tribology. Martin in 1916 (Hamrock, 1991) solved the Reynolds equation for a thin film between two rigid cylinders and stimulated many other theoretical studies (Dowson and Whomes, 1966; Grubin, 1949; Hamrock, 1991; Merritt, 1935). Martin's solution for the film thickness was found to be less than the surface roughness of the gear teeth that they were studying and was later discovered to be inaccurate as they neglected elastic deformations. The original work of Martin is not in English and Hamrock (1991) discussed the results of this study in their publication.
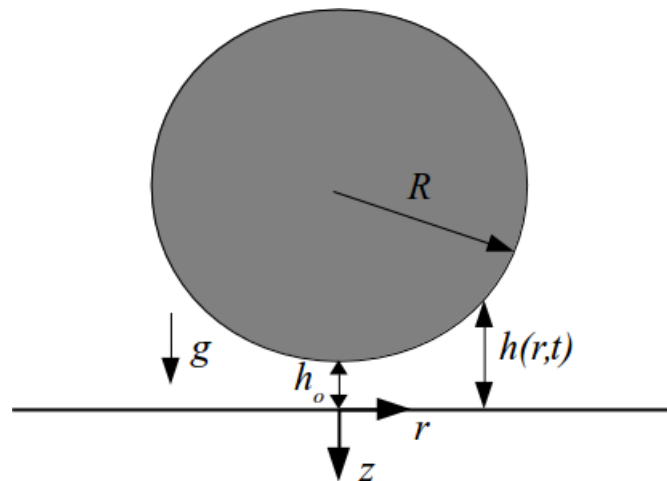
Fig. 1.1 A sphere approaching a plane, where r, z are the radial and vertical directions, $D = 2R$ is the diameter of the sphere, g is the acceleration due to gravity, and $h(r, t)$ is the time-dependent distance between sphere and the bottom wall.

Reynolds equation can also be used for studying normal collision between a sphere and a wall in a viscous medium as shown in Figure 1.1. The theory exploits the disparity between the vertical and lateral length scales in the problem and as a consequence neglects the inertial terms in the Navier-Stokes equation. In the lubrication approximation, streamwise (radial) gradients in every dynamical quantity except pressure are dropped, since they are assumed to be far smaller than the gradients normal to the wall. This leads to a parabolic profile across the gap at every radial location for the radial velocity between the two solid bodies. Reynolds equation in cylindrical coordinates reads as:

$$\frac{1}{12\mu r}\frac{\partial}{\partial r}\left[rh(r,t)^3\frac{\partial p(r,t)}{\partial r}\right] = \frac{\partial h(r,t)}{\partial t} \tag{1.1}$$

where r and t are the radial and time coordinates, μ is the dynamic viscosity of the surrounding fluid, $p(r,t)$ is the pressure between the sphere and the bottom plane, and $h(r,t)$ is the height of the sphere above the bottom plane as shown in Figure 1.1. Solving equation 1.1 gives the pressure as a function of the radial coordinate r (under the approximation that the profile of the sphere can be treated as a paraboloid for $r \ll R$) in the film to be:

$$p = \frac{3\pi\mu R\dot{h_o}}{(h_o + r^2/2R)^2} \tag{1.2}$$

where h_o is $h(r = 0, t)$ and R is the radius of the sphere. The velocity of the sphere $\dot{h_o}$ at a time t is given by $\partial h/\partial t$. For small h_o (less than $0.01R$), this theory gives us the lubrication drag force also known as Taylor's formula (Brenner, 1961; Cox and Brenner, 1967):

$$F = \frac{6\pi\mu R^2}{h_o}\dot{h_o} \tag{1.3}$$

This equation predicts that a falling sphere will not make contact with the bottom wall in finite time. While the decelerating force diverges as $h_o \to 0$, the velocity in the numerator also decreases, and the ratio produces this result.

Cox and Brenner (1967) gave a correction for the hydrodynamic force on a rigid sphere approaching a plane wall in a viscous medium, taking into account the first-order effects of fluid inertia. They obtained a solution by incorporating small Reynolds number effects and by employing the singular perturbation technique:

$$F = 6\pi\mu R\dot{h_o}\left[\frac{R}{h_o} + \frac{1}{5}\left(1 + \frac{1}{2}Re\right)\ln\frac{R}{h_o}\right]. \tag{1.4}$$

Cox and Brenner (1967) defined Reynolds number Re using the instantaneous velocity of the sphere, $Re = \rho_f h_o \dot{h}_o / \mu$. Where ρ_f is the density of the fluid. At $h_o/R \ll 1$ and $Re \to 0$, equation 1.4 reduces to the expression for the lubrication force (equation 1.3). Equation 1.4 still suggests that a falling sphere will not come in contact with the bottom wall within a finite time. Our experiments in Chapter 2 will show that this is not true and that there is a vital need for a theoretical framework that allows for inertial effects in their entirety. Such a framework has been attempted and discussed in Chapter 3. However, the new theory also does not directly predict contact in finite time. We will see, however, that all these theories predict a large downward velocity within nanometers of the contact, where the continuum approximation is no longer valid. So, it may be presumed that contact will occur.

1.2.2 Elastohydrodynamic lubrication

Following Martin's work, Grubin in 1949 (Hamrock, 1991) included the elastic deformations and provided a solution for line contacts under load. The original work of Grubin is not in English and Hamrock (1991) discussed the results of this investigation. The so-called elastohydrodynamic lubrication solution assumed the deformation between solids to be Hertzian and similar to what is produced in dry contacts. Grubin's result is considered to be an improvement on Martin's work as their analysis predicted film thickness one or two orders of magnitude greater than that predicted for a rigid cylinder pair.

To the best of my knowledge, the first study of two-sphere collisions in a viscous fluid where the spheres are allowed to deform was done by Davis et al. (1986) within an elastohydrodynamic framework. Working within the lubrication approximation, they suggested that the pressure in the thin fluid film between the spheres is large enough to elastically deform them. The stored elastic strain energy is released as kinetic energy, causing a rebound of the particles without solid-on-solid contact, at large enough inertia. This idea must be reconciled with our everyday experience of acoustic emission and dents which occur when solids collide within fluids. Since collisions of this sort are encountered in our daily lives and industries regularly, it is very important to understand them.

It is now recognized (Gondret et al., 1999, 2002; Joseph et al., 2001; Yang and Hunt, 2006; Zenit and Hunt, 1999) that the dynamics of such a collision is controlled by the Stokes number St, which is the ratio of a sphere's inertia to viscous forces and is defined as:

$$St = \frac{2}{9}\frac{\rho_s v_c R}{\mu} = \frac{2}{9}\frac{\rho_s}{\rho_f}Re; \quad Re = \frac{\rho_f v_c R}{\mu}, \tag{1.5}$$

where ρ_s and Re are, respectively, the density and the Reynolds number of the sphere and ρ_f is the density of the fluid. Here v_c is the velocity the sphere would attain at $h_o = 0$, if the other body (sphere or bottom wall) was not present and lubrication forces would not have come into action. For a falling sphere, a large St means that the dynamics is dominated by gravity. Small St means that the viscous forces dominate the dynamics of the sphere. Similarly, for two spheres colliding in a viscous medium, a large St implies that the dynamics is dominated by the inertia of the spheres. In general, for a particle in an arbitrary background flow, a large St means that the particle trajectory will appear to be uncorrelated to the background flow and $St = 0$ means that the particle will just act as a tracer and follow the flow.

The elastohydrodynamic lubrication theory predicts a critical Stokes number St_c (Davis et al., 1986), below which a collision between smooth spheres or a sphere and a wall does not result in a bounce. Experiments on sphere-wall collisions by Barnocky and Davis (1988), Gondret et al. (1999, 2002), and Joseph et al. (2001) measure the coefficient of restitution (by video imaging), which is the ratio of the velocity just after impact to the velocity just before impact. They found, by plotting the coefficient of restitution as a function of St, that there is a transition from settling to bouncing at St_c ranging from about 8 to 15. There is only a modest variation of St_c with the material of the sphere/wall (Gondret et al., 2002; Joseph et al., 2001). E.g., Gondret et al. (2002) found similar St_c for teflon (Young's modulus $E = 0.5GPa$) and tungsten carbide ($E = 534GPa$).

Surface roughness can play a role when the separation between the solids becomes comparable to the roughness. Davis (1987) and Barnocky and Davis (1988) accounted for this in their calculation by imposing an inelastic collision at a cutoff distance set by the roughness. Joseph et al. (2001) used spheres with well-characterized roughness and argued that the scatter in their data could be explained by the surface roughness. Lecoq et al. (2004), Mongruel (2012), and Chastel and Mongruel (2016) concluded that artificial roughness can indeed increase the approach velocity before impact. Cawthorn and Balmforth (2010) studied a two-dimensional (2D) wedge falling under gravity in a viscous medium and predicted an upward drag force on the wedge which diverges logarithmically with the minimum separation between the wedge and the bottom wall. Based on this, they suggested that an object falling under gravity will approach the bottom wall faster if the object has sharp asperities. They agreed that studying the descent of a cone under gravity will be more relevant — we will present the study of a cone falling under gravity in Chapter 3.

Barnocky and Davis (1989) studied the effect of pressure-dependent viscosity in the elastohydrodynamic framework of Davis et al. (1986) by including the relation for viscosity

proposed by Chu (1962). They concluded that the effect of this dynamic increase in viscosity was weak and decreases St_c by a small amount. Donahue et al. (2010) suggested that in a two-sphere collision, the rebound will occur when the sphere encounters the largest of the three length scales below:

1. Elastohydrodynamic length scale (Davis et al., 1986, 2002)

   Davis et al. (2002) derived the elastohydrodynamic length scale x_e by using a scaling argument and suggested that under the elastohydrodynamic lubrication framework the sphere will rebound when the gap between the solid surfaces is equal to this length scale:

$$x_e = \left(\frac{3\pi\theta_0\mu R^{3/2}v_o}{\sqrt{2}} \right)^{2/5} \tag{1.6}$$

   where v_o is the relative velocity between the two spheres in the Davis et al. (1986) framework and can be taken as the terminal velocity for a sphere approaching a bottom wall. θ_0 is given by

$$\theta_0 = \sum_{i=1,2} \frac{1-\nu_i^2}{\pi E_i} \tag{1.7}$$

   where ν_i and E_i are the Poisson ratio and Young modulus of elasticity of the ith sphere. This new length scale is very similar to the length scale obtained by Davis et al. (1986), $x_1 = 4\theta_0\mu R^{3/2}v_o$.

2. Roughness scale (Barnocky and Davis, 1988; Davis, 1987; Davis et al., 2002)

   If the sphere has sufficiently large asperities, then physical contact and rebound can be presumed to occur when the gap between the solid surfaces has decreased to the height of these roughness bumps.

3. Glass-transition length scale (Donahue et al., 2010).

   In this condition, once the pressure in the gap (equation 1.2) has risen to the glass transition pressure of the fluid p_{gt}, the sphere will rebound.

$$x_{gt} = \sqrt{\frac{3\mu R \dot{h_o}}{p_{gt} - p_o}}; \tag{1.8}$$

   where p_o is the hydrostatic pressure of the fluid. There is a lack of well-established data for p_{gt} for most of the fluids. Donahue et al. (2010) used 0.55 GPa as the glass transition pressure for silicone oil in their analysis based on their private discussions with Scott Bair of Center for High-Pressure Rheology and the study of Angel et al. (2007).

Short-range forces such as Van der Waals forces could conceivably play a role close to contact but are not considered in these studies of bouncing. Whether contact occurs during rebound is still not established. It is difficult with video imaging techniques to resolve contact dynamics spatially or temporally. In our experiments in Chapter 2, we directly address the question of the existence of solid-on-solid contact using an electrical set-up and in Chapter 4 we investigate kinematics very close to the moment of impact. In Chapter 3 we try to compare our experimental observations to a more detailed theoretical calculation by going beyond the lubrication theory.

1.3 Granular structure

Once the contact between the spheres is established, the friction between the surfaces takes over. It is therefore important to study the structures that these frictional contacts can create and the stresses they carry, as such structures are prevalent in the world at all scales. These structures are heavily controlled by frictional contacts and a majority of the literature on granular matter deals with such systems in a medium of zero resistance. Stresses inside a static granular column have been a subject of study for years now, see e.g. Nedderman (2005). Janssen (1895) showed that pressure at the bottom of a container, filled with grains, saturates with the fill-height of the container (Sperl, 2006). The major assumptions in Janssen's theory can be summarised as:

1. The vertical component of the stress σ_{yy} is uniform across the cross-section.

2. The Coulomb friction at the wall is fully mobilized, i.e., shear stress, $\tau = \sigma_{xz} = \mu_w \sigma_{xx}$, where μ_w is the coefficient of friction at the side walls of the column and σ_{xx} is the horizontal normal stress.

3. Horizontal normal stress, σ_{xx}, is proportional to vertical stress, $\sigma_{xx} = K\sigma_{yy}$. Where K is the proportionality constant and is also referred to as Janssen's constant.

Using these predictions, Janssen suggested that the vertical stress (σ_{yy}) at a height y decays exponentially with fill-height h and is given by:

$$\sigma_{yy}(y) = \rho g s \left(1 - e^{-\frac{(h-y)}{s}}\right), \tag{1.9}$$

where g is the acceleration due to gravity, and ρ is the bulk density. s is referred to as the decay length and is determined by geometry. For a 2D container of width W,

$$s = s_{2D} = \frac{W}{2K\mu_w}.$$

(1.10)

A quasi 2D granular column is a container with a thickness just above the diameter of the particles so that particles only form a single layer inside the container. For a quasi 2D container with thickness t and width W,

$$s = s_{q2D} = \frac{Wt}{2W + 2t}\frac{1}{K\mu_w}.$$

(1.11)

For a 3D column of radius R,

$$s = s_{3D} = \frac{R}{2K\mu_w}.$$

(1.12)

This behavior of a granular column is obviously different from that of a column filled with liquid in which pressure increases linearly as we go down the column. To test Janssen's prediction, the vertical stress at the bottom of a granular column has been widely documented for both 2D and 3D cases; see e.g. Vanel and Clément (1999), Qadir et al. (2010), Bratberg et al. (2005), Liu et al. (2009), Bertho et al. (2003), Wen et al. (2015), Chand et al. (2014) and Ovarlez et al. (2003) in experiments and Vanel et al. (2000), Ovarlez and Clément (2005) and Zhao et al. (2018) in simulations. To satisfy the second assumption of the Janssen's theory, i.e., to make the particles at the side walls fully mobilized, a common practice is to use a column with a moving wall (Ovarlez et al., 2003; Vanel and Clément, 1999). Vanel and Clément (1999) used movable bottom walls, whereas Ovarlez et al. (2003) translated the side walls vertically. The movable wall is slowly translated to mobilize the particles in contact with the side walls and then the packing is allowed to relax. Vanel and Clément (1999) proposed a two-parameter fit to reconcile their experimental observations of pressure at the bottom of a granular column with Janssen's theory. They observed a hydrostatic-like region up until a certain fill-height of the granular column, followed by a region at larger fill-height that obeys Janssen model. They suggested that the hydrostatic-like region can be thought of as a hydrostatic slice at the bottom of the container. Their two-parameter fit has been widely accepted in the granular community.

A common explanation for the saturation of vertical stress at the bottom of a granular column at large fill-heights is that the walls of the column bear some of the load of the granular pile with the help of wall-friction. Hence, filling the container with more particles just increases the load on existing, mutually-compressed particles. These

mutually-compressed particles make a chain and transfer this load to the side walls with the help of wall-friction. These chains are referred to as force chains and a set of interconnected chains is referred to as force network (Majmudar and Behringer, 2005; Vanel et al., 2000). Adding more grains in the column helps in creating new force networks which transfer the load to the side walls, while the load at the bottom of the container remains unaffected. Janssen's pressure at the bottom of the container has been studied in moving walls system as well. Bertho et al. (2003) measured Janssen's pressure on the bottom wall in a system in which the side walls were moved at different velocities while the base remained fixed. This was achieved by using a tube of slightly bigger diameter than the base as the side wall. They concluded that Janssen's prediction is valid for a large range of velocities. It is widely known (Hilton and Cleary, 2011; Janda et al., 2012; Shah et al., 2017; Tighe and Sperl, 2007) that the efflux of granular matter from a silo or a container occurs at a fixed speed, irrespective of fill height. This phenomenon has also been related to Janssen's observation of pressure saturation (Jaeger and Nagel, 1992; Jaeger et al., 1996). However, it has been proven now that constant efflux from a granular container is not related to Janssen's pressure as, unlike Janssen's pressure the efflux rate does not depend on the width of the container (Andreotti et al., 2013; Mankoc et al., 2007).

Despite a large number of studies on measuring pressure at the bottom of a granular pile, there is still not a clear understanding of local stress variation inside the granular column, especially for a 2D granular column. Landry et al. (2004) and Zhao et al. (2018) investigated the stress variation inside a cylindrical column to test the Janssen model using numerical simulations. Landry et al. (2004) used pouring and sedimentation techniques for creating the granular columns in their study. In the pouring technique, a fixed number of grains are poured from a fixed height above the granular column at fixed time intervals until the total number of grains in the column is equal to the desired value. In the sedimentation technique, all the grains are first placed inside the granular column with zero initial velocity to occupy the whole space of the container, and then they are allowed to settle under gravity. Both these techniques are discussed in detail in Chapter 5. Zhao et al. (2018) did not mention the protocol they used for creating the granular column. Both Landry et al. (2004) and Zhao et al. (2018) found the two-parameter form of Vanel and Clément (1999) to be a better fit than Janssen's form for their numerical data. Landry et al. (2003) measured the stress variation inside a 2D granular column created by the pouring method and found the results to be closer to the Vanel and Clément (1999) form. It is also not known if Landry et al. (2003, 2004) and Zhao et al. (2018) mobilized the particles in contact with the side walls by moving

bottom or side wall before measuring the vertical component of stress. As per the private conversation with Steve Plimpton [one of the authors of Landry et al. (2003, 2004)], the stress shown in their article was total or global stress of the granular column and not the local stress. This brings us back to our initial point of the unavailability of thorough studies on local stress variation inside a 2D granular column. One of the main reasons for the lack of such studies is the fact that it is difficult to measure local stress inside a granular column experimentally.

Therefore, it is still not clear how the local stress varies with the vertical or horizontal coordinate in the bulk of the column and how it depends on the method by which the column is being created. The series of assumptions used by Janssen has not been fully tested for different methods by which a granular column can be created. This will be addressed in Chapter 5 of this thesis. With the help of numerical simulations, I will discuss how the stress profile in the bulk of a 2D granular column depends on the fill-height of the column and how it can vary depending on the protocol used to create the granular column.

1.4 Immersed packing

The packing arrangements of multi-particle systems can be completely different inside a fluid and can depend on many parameters [like buoyancy forces and Stokes number St, if the packing is created by sedimenting particles in a fluid (Farrell et al., 2010; Onoda and Liniger, 1990)]. This makes it interesting and important to understand how such packings come about and if it can be exploited to understand the jamming transition (O'Hern et al., 2002).

In two dimensional systems, the highest packing arrangement is obtained by hexagonal crystalline packing where the volume fraction is around $\phi_{hex} = 0.907$. A disordered or amorphous packing has a much smaller volume fraction. Random close packing (RCP) is referred to as the largest packing fraction achievable without deliberately introducing crystalline structures. In the literature, RCP limit has been discussed as a jamming transition point considering the disordered structure to be glassy or liquid-like and the crystalline structure to be solid (O'Hern et al., 2002). Random loose packing (RLP) refers to the lowest packing fraction achievable in a disordered stable structure. RCP and RLP limits are typically quoted for three dimensional systems to be 0.64 and 0.55, respectively (Bernal and Mason, 1960; Berryman, 1983; Farrell et al., 2010; Onoda and Liniger, 1990; Scott and Kilgour, 1969). However, it has been seen that RLP is a friction dependent number and that there is no fixed limit (Dong et al., 2006; Farrell et al., 2010;

Jerkins et al., 2008; O'Hern et al., 2002; Scott and Kilgour, 1969; Zhang et al., 2001). Chaudhuri et al. (2010) established that there is no tight limit on RCP for frictionless spheres in 3D systems.

In one of the first studies of loose packings, Onoda and Liniger (1990) developed a value of RLP to be 0.555 ± 0.005 in the limit of zero gravitational force by sedimenting glass spheres in a fluid of similar density. Though a question arises about the strength of such packings and if more fragile packings can be created in such conditions when the load on each particle is negligible. Farrell et al. (2010) studied the loose packing of frictional spheres in a fluid and found that there exists a critical Stokes number at which the loose packing limit is attained. They concluded that the limit is determined by the friction of the particles and that this limit can be attained by going to slow deposition.

The existence of disordered packing in a 2D system is a subject of debate as monodisperse 2D packings easily crystallize. Therefore bidisperse spheres are used in the granular community to study 2D systems. The RCP for a pile of monodisperse discs in a 2D system is found to be near 0.82 (Berryman, 1983; Visscher and Bolsterli, 1972). Bidisperse frictionless spheres in the 2D system seem to have a larger packing fraction of 0.84 (O'Hern et al., 2002). Loose packing in the 2D system has been scarcely studied and its existence is under debate. An attempt to develop an experimental protocol to create disordered packings of frictional, mono-disperse spheres in the 2D systems will form the final chapter of this thesis.

1.5 Overview of work and findings

In the next chapter of this thesis, I will show that a sphere falling under gravity makes direct mechanical contact with the bottom plate during the bounce, in contrast to expectations based on elastohydrodynamic theory. An electrical set-up was used where a conducting sphere was dropped from a given height on a conducting plate and a voltage was applied between them. When the sphere makes or breaks electrical contact with the plate, the circuit closes or opens. We observed that there is a critical Stokes number for collision below which the sphere does not bounce and the first electrical contact persists for all time. For larger values of St, the sphere makes metallic contact for a finite time δT_c. It then breaks the contact and is in the fluid for a flight time T_F, before settling into permanent electrical contact. It was observed that all contacts were purely resistive, and the duration and other properties were found to be independent of the applied voltage. The experiments not only resolve the question of the contact but also provide information on the nature of the contact and the dissipation during such contacts.

In an attempt to understand this difference between our experimental observations and lubrication theory (and elastohydrodynamic lubrication theory), we develop a new method to calculate the hydrodynamic force on a falling sphere in Chapter 3 of this thesis. We analytically go beyond lubrication theory by including unsteady terms and inertial terms, which were neglected in lubrication theory. We develop a boundary layer equation to describe the flow and solved it by a novel method. This allows us to obtain the radial velocity profile below the sphere which is then used to solve for the pressure and the sphere's acceleration. By defining an appropriate non-orthogonal coordinate system, we are able to solve the dynamics as a succession of parametric ordinary differential equations. At the end of the chapter, we also argue that even a non-deformable sphere with an atomic-scale roughness should be expected to make contact with the plate just using the lubrication approximation.

In the fourth chapter of this thesis, we experimentally observe the dynamics of the sphere just before and after the contact and quantify the deviation from lubrication theory which results in the final contact. We use our electrical set-up to trigger a high-speed camera and use conventional image analysis to track the sphere at high resolution, with the help of a bellow and a macro lens. The dynamics observed up to a few micrometers above the bottom plate showed systematic deviation at small heights from lubrication theory. We find that the actual approach velocity is slightly greater than predicted by lubrication theory at these heights. Rebound and second impact dynamics are found to be similar to the first impact dynamics.

In a separate study of frictional multi-particle systems, we show numerically how a granular column can be different from both hydrostatic columns and the standard Janssen model in Chapter 5 of this thesis. This is achieved by observing the stress variation in the bulk of a 2D static granular column filled with monodisperse spheres. We perform LAMMPS-based molecular dynamics simulations, (https://lammps.sandia.gov/) Plimpton (1995) to construct granular columns in four different ways, as discussed in the chapter. We study how the stresses in the bulk vary in a 2D monodisperse system with these protocols. The different protocols give different vertical stress profiles and forces on the walls. We also find that the static friction on the wall can be far from the Coulomb yield limit and depends on the construction protocol.

In the last chapter, we present an experimental procedure to create disordered packings of frictional mono-disperse spheres in 2D systems. Our goal is to use the principles learned in Chapters 2-4 to deposit particles at St below a critical value, so that every new particle incident on a packing transfers almost no momentum to the particles beneath. In the protocol developed, the container is kept at an inclination angle θ and spheres are

allowed to roll downhill within a viscous fluid to create disordered packings. Packing has been observed at four different inclination angles and the packing density was found to decrease with the reduction of this angle.

Chapter 2

Is there a contact in normal collision?

The work in this chapter was done in collaboration with Dr. G Rajalakshmi. This chapter's content has been published in Physical Review Fluids (Birwa et al., 2018) and the chapter follows that article closely.

2.1   Introduction

Wet collisions, collisions of two solids bodies in a viscous medium, have been a subject of studies for years now. One of the celebrated triumphs of fluid mechanics is Reynolds (1886) explanation of how a sheared viscous fluid generates sufficient pressure to separate the moving rotors in a journal bearing. And yet, a spoon clangs against the side of a cup as we stir a fluid. In Chapter 1, we have discussed the history of this problem.

In this chapter, we consider the simple situation of a sphere falling towards a plane in a viscous fluid. Balls rebound when bounced on the floor. However, if the air is replaced by a highly viscous fluid a ball can settle without bouncing depending on the Stokes number of the ball. We ask whether solid-on-solid contact occurs during bouncing collisions, and more generally whether solid dissipation plays a role in determining the transition from bouncing to settling. Whether contact occurs during rebound is still not established. It is difficult with video techniques to resolve contact dynamics spatially or temporally. In our experiments, we directly address the existence and influence of solid-on-solid contact using an electrical set-up to investigate kinematics very close to the moment of impact.

2.2   Experimental set-up

(a)

(b)
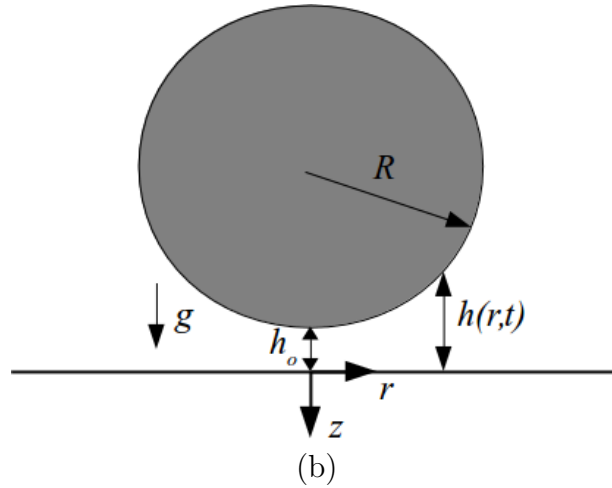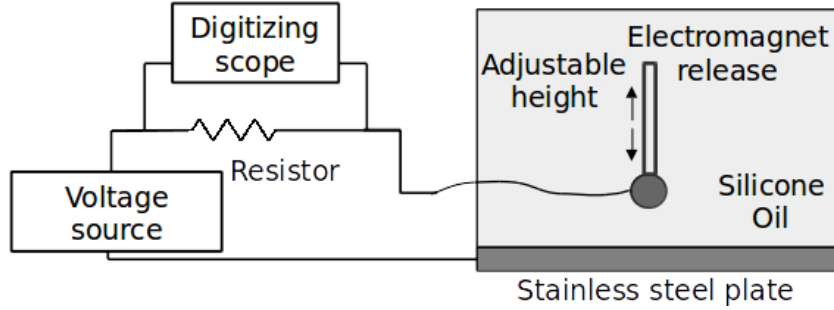
Fig. 2.1 (a) Schematic diagram of the experimental set-up. The voltage is measured across a resistor (R_s) of 220 kΩ. (b) A sphere approaching a plane, where r, z are the radial and vertical directions, $D = 2R$ is the diameter of the sphere, g is the acceleration due to gravity, and $h(r, t)$ is the time-dependent distance between sphere and the bottom wall.

We dropped stainless steel spheres on a stainless steel plate of 10 cm x 10 cm cross-section and 1 cm thickness through silicone oil of dynamic viscosity $\mu = 0.336 \pm 0.020$ Pa-s, and density $\rho_f = 970$ kg/m^3. As shown in Figure 2.1 (a), a voltage was applied between the plate and the sphere. When the sphere makes or breaks electrical contact with the plate, the circuit closes or opens, King et al. (2011). The current through the resistor was sampled by a digital oscilloscope (Tektronics DPO 4054B) at a rate of 1 to 5 MHz. Both direct current (DC) and alternating current (AC) voltage sources were used in the experiments.

An electromagnet mounted on a micrometer translation stage released spheres from different initial heights, allowing us to vary the incoming velocity and the Stokes number. The release heights ranged from 1 mm to 70 mm and were determined to an accuracy of 20 μm, corresponding to a maximum error of 2% at the lowest height. In each case, the nominal St was determined from the velocity v_c computed at the height of the plate's surface in the absence of the plate (see equation 1.5). For this, we solved the equation of motion of the ball under gravity, buoyancy and viscous drag (Figure 2.1 (b) using an empirical formula from Flagan and Seinfeld (1988) applicable to our experimental range of Reynolds number,

$$\rho_s V \ddot{h}_o = (\rho_s - \rho_f) V g - 3\pi\mu D \dot{h}_o (1 + 0.15 Re_{in}^{0.687}), \qquad (2.1)$$

where $Re_{in} = \rho_f D \dot{h}_o / \mu$ is the instantaneous Reynolds number of the sphere defined by using the instantaneous velocity and diameter of the sphere. Take note that Re_{in} is changing with time. V is the volume of the sphere and $h_o = h(r = 0, t)$ is the gap between the sphere and the plate. The dot on h_o represent total derivative in time. The resulting Stokes numbers (St) ranged from 5 to 28 with a maximum error of 6.5% at the largest St (including contributions from the temperature dependence of viscosity and precision of release height). Corresponding Reynolds number Re, defined by using v_c, varied from 5.7 to 32.

2.3   Roughness

We used two types of spheres. One was as-purchased stainless steel ball bearings with density $\rho_s = 7630$ kg/m^3 in two diameters, $D = 16$ mm and 12 mm. The second type of sphere, $D = 15.4$ mm, was produced by etching the 16 mm balls with HNO$_3$ in a 1:3 aqueous solution for 10 minutes. We measured surface topography with a diamond-tip Dektak contact profilometer and extracted position-dependent roughness from the difference ξ between the measured height, and the best-fit spherical profile. The as-purchased spheres had smooth patches with low rms roughness around ~ 0.025 μm interspersed with widely separated pits (of typical height $1 - 2$ μm) and mounds (of typical height 0.25 μm), with lateral size ~ 10 μm. These numbers varied slightly between individual spheres. The etched spheres had larger, but more uniform roughness with an rms value ~ 0.4 μm but several larger peaks of the order of $1-2$ μm. The typical lateral scale of the roughness is ~ 100 μm (see Table 2.1) and a probability density distribution of roughness for all the three spheres is shown in Figure 2.2.
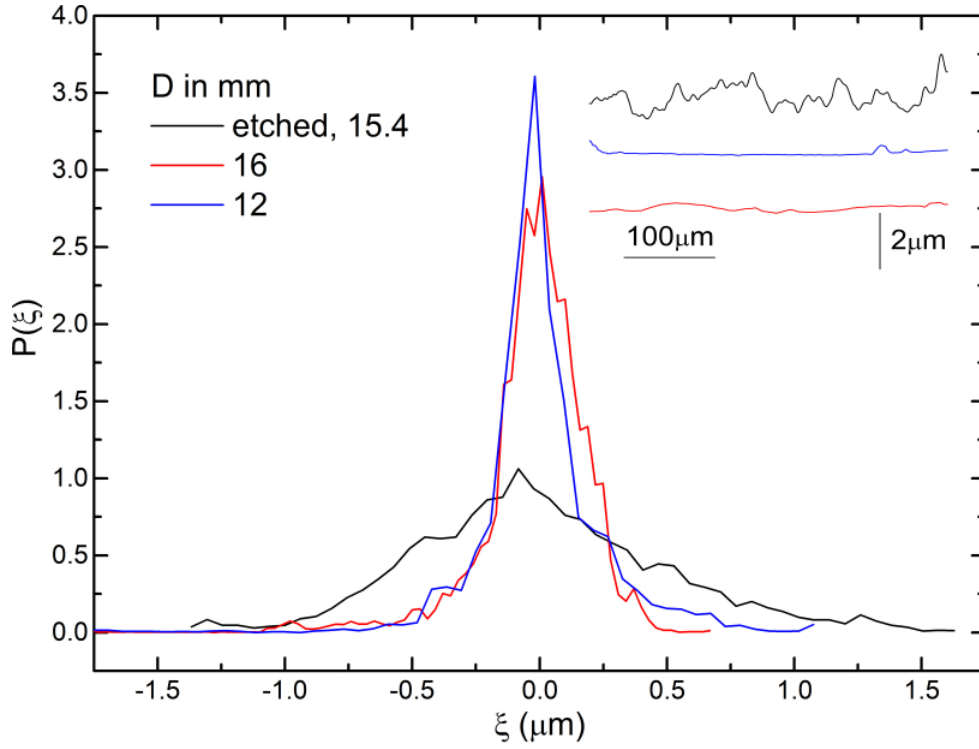
Fig. 2.2 Probability density $P(\xi)$ of the roughness of spheres as measured with a contact profilometer. To obtain the roughness ξ, the path traced by profilometer as a function of distance has been subtracted from the gross curvature of the sphere. The inset shows typical profiles $\xi(s)$ of roughness as a function of the position s along the surface, for all the three spheres used.

Table 2.1 Roughness values

D =	12 mm	16 mm	15.4 mm
RMS (μm)	0.25	0.22	0.5
Max positive deviation (μm)	1.1	0.68	1.66
Max negative deviation (μm)	-1.78	-1.77	-1.4

The profilometer has a lateral resolution of 0.5 μm and a vertical range of 65.5 μm. The vertical resolution of the profilometer is $\approx$ 1 nm. The profilometer tip travels along a path of length $\sim$ 0.4 mm along the surface of the sphere. We fit a circle with radius value the same as the radius of the sphere to the height along the path traced by the profilometer. This yields the global radius of curvature along this path as shown in Figure 2.3. The deviations from this fit give the local roughness, ξ of the topography of the surfaces. Note that the profile shown in Figure 2.3 is an example of a particularly

rough region of the etched sphere. The unetched spheres are much smoother. In more typical line profiles, much fewer asperities would be found. As can be seen from the statistics of ξ given in Table 1, the etched 15.4 mm sphere's surface was found to be most rough; as discussed in above paragraph. It is also the least heterogeneous, with relatively uniform roughness across the surface.
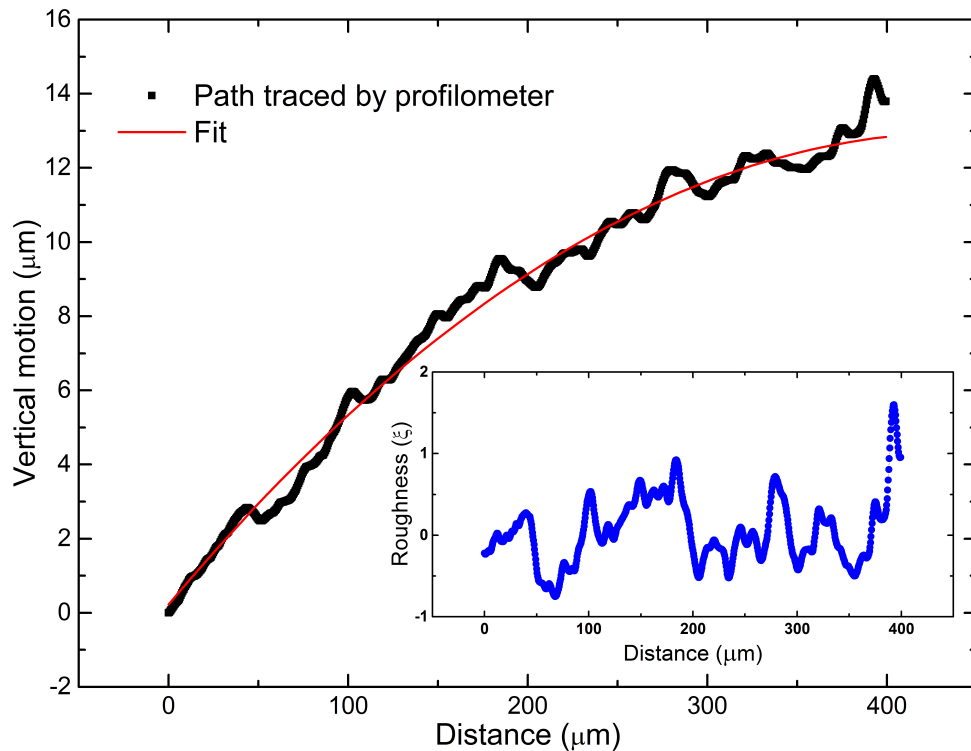
Fig. 2.3 A fit for the 15.4 mm etched sphere on the path traced by the profilometer as a function of position along a line on the sphere's surface is shown in red. The fit gives us the global curvature of the path and the local roughness of the sphere is obtained by subtracting the surface profile from this fit. The roughness (ξ) is shown in blue in the inset.

The plate roughness was measured using optical profilometry. The rms roughness of the plate was found to be around 0.29 μm and the average of the maxima of the peak to valley height from 12 random samples of the plate was observed to be 3.2 μm. In Chapter 1, we talked about Donahue et al. (2010) suggestion that in a two-sphere or a sphere-wall collision, the rebound will occur when the separation between the sphere and the plate decreases to any of the three length scales: 1.) Elastohydrodynamic length scale, 2.) Glass-transition length scale, or 3.) Roughness length scale. In Figure 2.4, we show the comparison between all the three length scales for 16 mm sphere and for the range of St we are studying. Glass transition length scale is determined by using 0.55

GPa as glass-transition pressure (Donahue et al., 2010). For both elastohydrodynamic length scale and glass transition length scale, v_c is used as the velocity (see Chapter 1). Elastohydrodynamic length scale measurement requires the value of the initial relative velocity and v_c is a good assumption. However, for measuring glass transition length scale, we need the impact velocity and v_c will be an overestimate. We will learn in Chapter 3 that this overestimate will be bigger for lower St and v_c will be close to the impact velocity at larger St. We note that the maximum combined roughness of the plate and the sphere is $\sim 1.6 + 0.68 \mu$m. However, it can be seen from Figure 2.2 that a vast majority of the roughness of the spheres is below this number and is much smaller for unetched balls. We assume a similar distribution of roughness on the plate. Thus given that the contact between a sphere and a plate initiated by a point contact, in a vast majority of the trials we expect contact at a distance smaller than the maximum combined roughness. Hence we have chosen rms roughness of the sphere as the length scale for roughness. Even if we add the rms roughness of the plate to this value, we find that the roughness length scale is below the other length scales, particularly at large St.
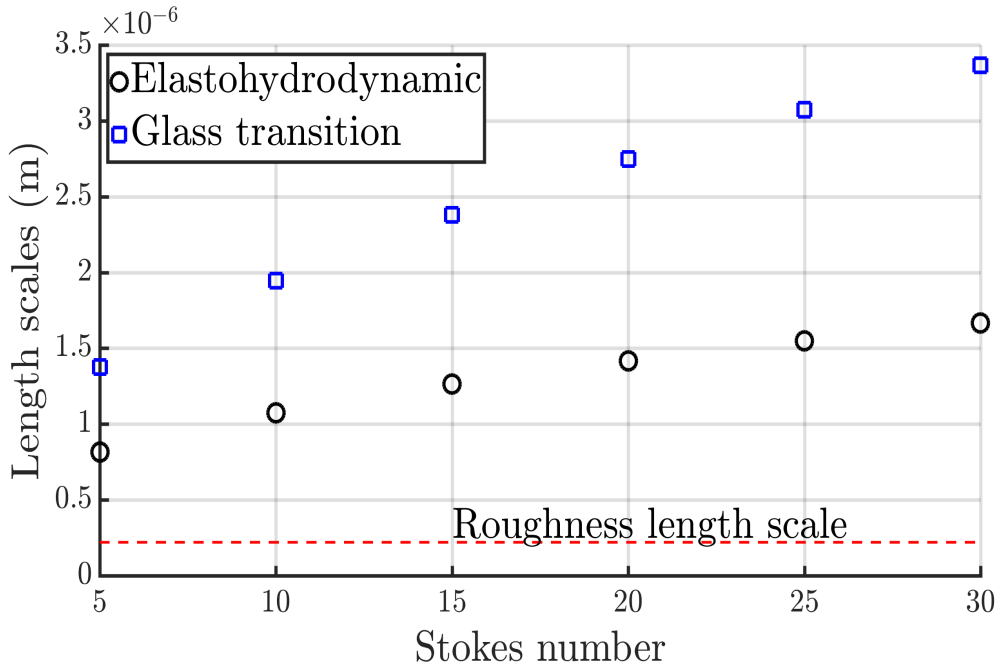
Fig. 2.4 Comparison between elastohydrodynamic, glass-transition, and roughness length scale. The roughness length scale is chosen as 0.22 μm, the rms roughness value for 16 mm sphere, and glass transition length scale is determined by using 0.55 GPa as glass-transition pressure (Donahue et al., 2010). For calculating the elastohydrodynamic length scale, Poisson ratio of 0.3 and Young's modulus of 210 GPa is chosen.

As per Figure 2.4, both elastohydrodynamic and glass-transition length scales are above rms roughness value for 16 mm sphere and, therefore, we should not encounter solid-on-solid contact and the sphere should rebound without making contact. However, our experiments contradict the theory and we do see contact before a rebound.

2.4 Contact observed
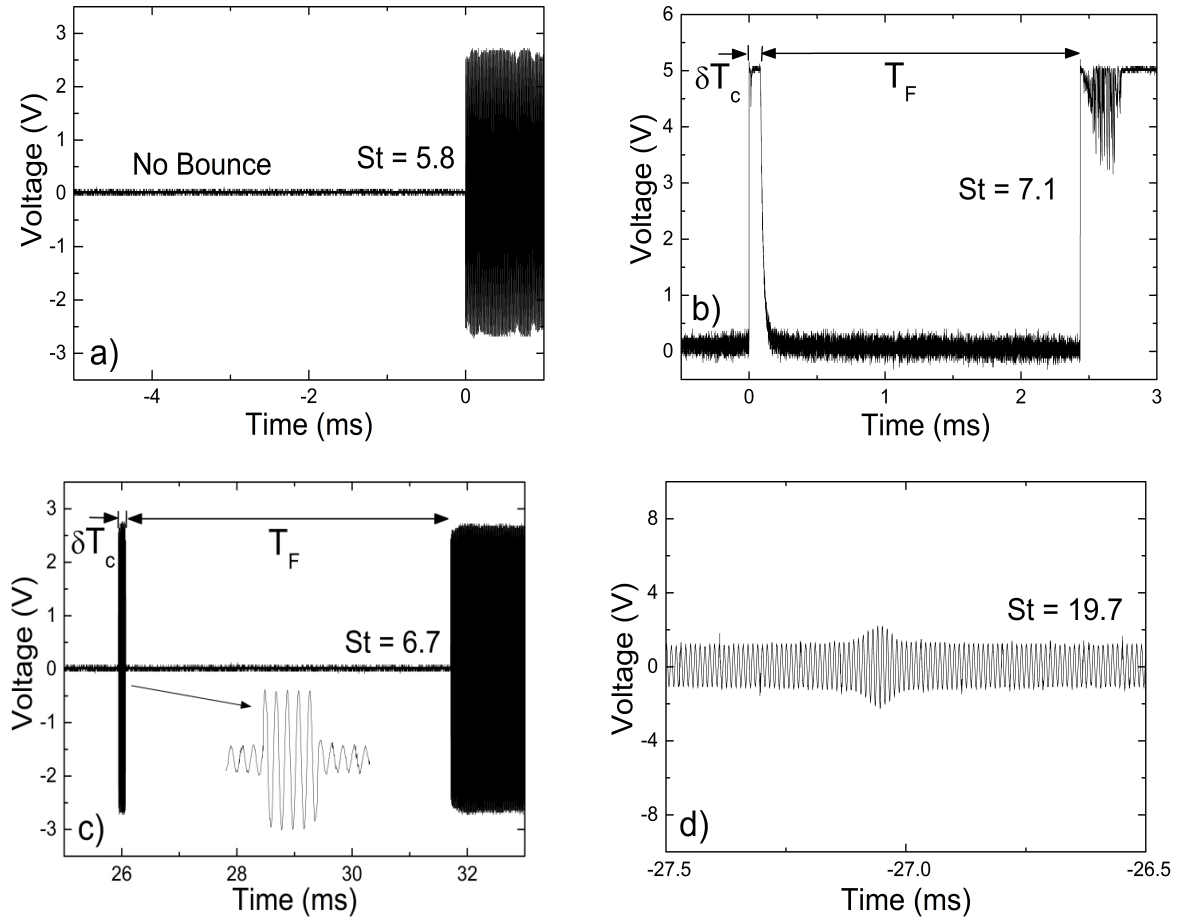
Fig. 2.5 Voltage versus time graphs for increasing St with AC and DC voltages. (a) At $St = 5.8$ with an AC applied voltage, no bounce occurs, but electrical contact is made in a finite time. This is the generic behavior for $St < St_c$. (b) At $St = 7.1$ and (c) at $St = 6.7$ with DC and AC voltages, respectively, we see a collision, and then a period of no contact, followed by permanent contact. The contact has much lower resistance than the series resistance i.e. $R_c \ll R_s$. This is the generic behavior for $St > St_c$. For $St > St_c$, we also see the case shown in (d) where there is a high resistance contact (R_c is of the same order as R_s) (see next section 2.5 : Effect of electrical forces).

In Figure 2.5 we show examples of the collision obtained by applying both AC [Figure 2.5 (a), 2.5 (c), and 2.5(d)] and DC voltages (Figure 2.5 (b) between plate and sphere. At very low Stokes number [panel (a), $St = 5.8$], we observe no bounces. The first electrical contact persists for all time. At larger values of St, as shown in Figure 2.5 (b) and 2.5 (c), the ball makes metallic contact for a finite time, δT_c. It then breaks contact and is in the fluid for a flight time T_F before settling into permanent electrical contact. There is a clear separation of scale between the contact time, δT_c (tens of μ-sec) and the flight time, T_F (tens of milli-sec). Contact can sometimes be noisy (as seen at late times in Figure 2.5 (b), presumably due to rolling or rocking of the sphere. Such differential motions have been studied for a sphere in a rotating cylinder by Ashmore et al. (2005) and Yang et al. (2006). Finally, we see instances, as shown in Figure 2.5 (d), where the contact resistance (R_c) between the ball and the plate is comparable to the external series resistance (R_s).

To test if electrical forces play a role in contact mechanics, we compared our results with high-frequency AC (100 to 500 kHz) to results with a DC voltage and made measurements as a function of the amplitude of the applied voltage. We chose silicone oil as the working fluid due to its high dielectric breakdown voltage (> 40 MV/m). There appears to be no systematic effect of the amplitude or frequency of the AC voltage or the choice of AC or DC voltage on the occurrence of contact, the duration of contact and on the intervals between bounces at a given St (see next section 2.5 : Effect of electrical forces). We thus conclude that our results are not due to dielectric breakdown. All observed contacts are resistive, that is, with no phase shift between the applied and measured voltages. However, we do point out that the relative frequency of low versus high-resistance contacts can be affected by many factors such as the impurity content of the oil, aging of the surface electrical properties, and the topography of the sphere following repeated collisions. To achieve consistent results, we report data taken under a set of fixed conditions.

The major qualitative result in Figure 2.5 is that the ball makes direct mechanical contact with the plate during the bounce, in contrast to expectations based on the elastohydrodynamic theory by Davis et al. (1986). Next, we explore the nature of that contact.

We define contact fraction, ϕ, as the fraction of experiments at a particular Stokes number in which the sphere made a low resistance contact with the plate's surface during the bounce, i.e., collisions as shown in Figure 2.5 (b) and 2.5 (c). The value of ϕ rises sharply from zero above a critical Stokes number St_c, which is the same for all three types of spheres we used. Thus solid-on-solid contact occurs even just above the threshold of bouncing. The value of $St_c \approx 6.2 \pm 0.5$ that marks the transition to
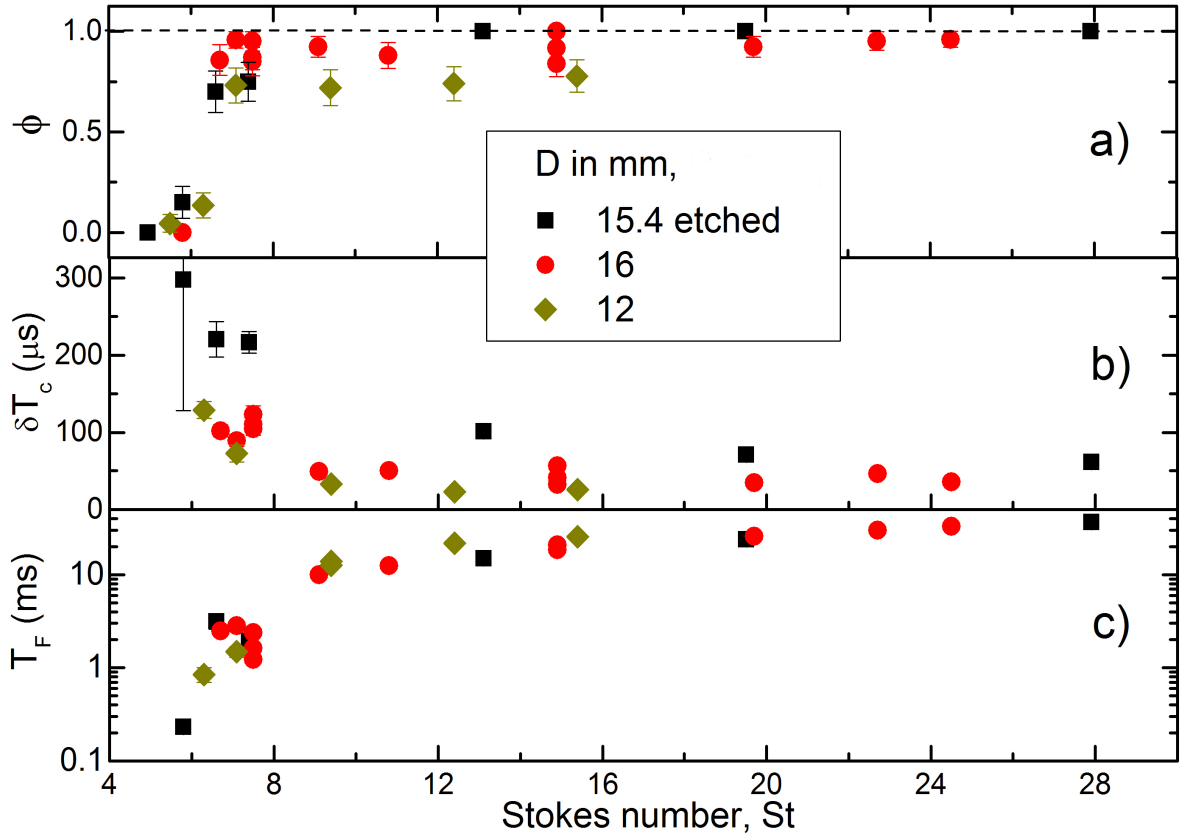
Fig. 2.6 Contact fraction (ϕ), contact time (δT_c), and flight time (T_F) vs Stokes number for the 15.4 mm etched ball, 16 mm and 12 mm unetched balls. Here we report data only for low resistance contacts ($R_c \ll R_s$) as in Figure 3b and 3c, however, the trends are unaffected if we include more resistive contacts (see next section 2.5 : Effect of electrical forces) as in Figure 2.5. Error bars are the standard deviation of measurements in panel (a) and standard error of measurements in panel (b) and (c) taken at fixed St. Wherever the error bars are not visible, errors are smaller than symbol size.

bouncing with mechanical contact is close to the bouncing transition observed in previous experiments by Gondret et al. (1999, 2002) and Joseph et al. (2001). We refer to ϕ as the contact fraction, even though it is actually a lower bound on the contact fraction, in that high resistance events are not included. Including high resistance events, as shown in Figure 2.9 does not change any qualitative trends (see the next section 2.5 : Effect of electrical forces).

In Figure 2.6 (b) we show data for the duration of contact, δT_c. The contact time δT_c decreases as the Stokes number is increased above St_c. The relatively small change of δT_c is consistent with calculations for a Hertzian, elastic impact which predict a very weak dependence of contact time on velocity, $\delta T_c \propto (U R_{eff})^{-1/5}$, where R_{eff} is the effective

radius at the point of contact (Landau and Lifshitz, 1986). For perfectly smooth spheres, $R_{eff} = R$, whereas R_{eff} will be smaller when a bump on the sphere is presented to the plane. Contact times for the etched spheres are slightly longer than those for the unetched spheres (which have very similar contact times for both sizes of the sphere). Roughness at the point of contact, rather than the sphere radius, possibly sets the relevant curvature at impact and influences the contact time (see appendix A: Hertzian calculation). In Figure 2.6 (c) we show the duration between the bounce and the next collision, which we refer to as the flight time T_F. This is a measure of the kinetic energy with which the ball rebounds from the plate. As expected, this is an increasing function of $(St - St_c)$. Furthermore, there is little or no variation with the type of sphere used, as opposed to the data for δT_c. This implies that the details of the solid contact may not affect the total dissipation, as elaborated below.
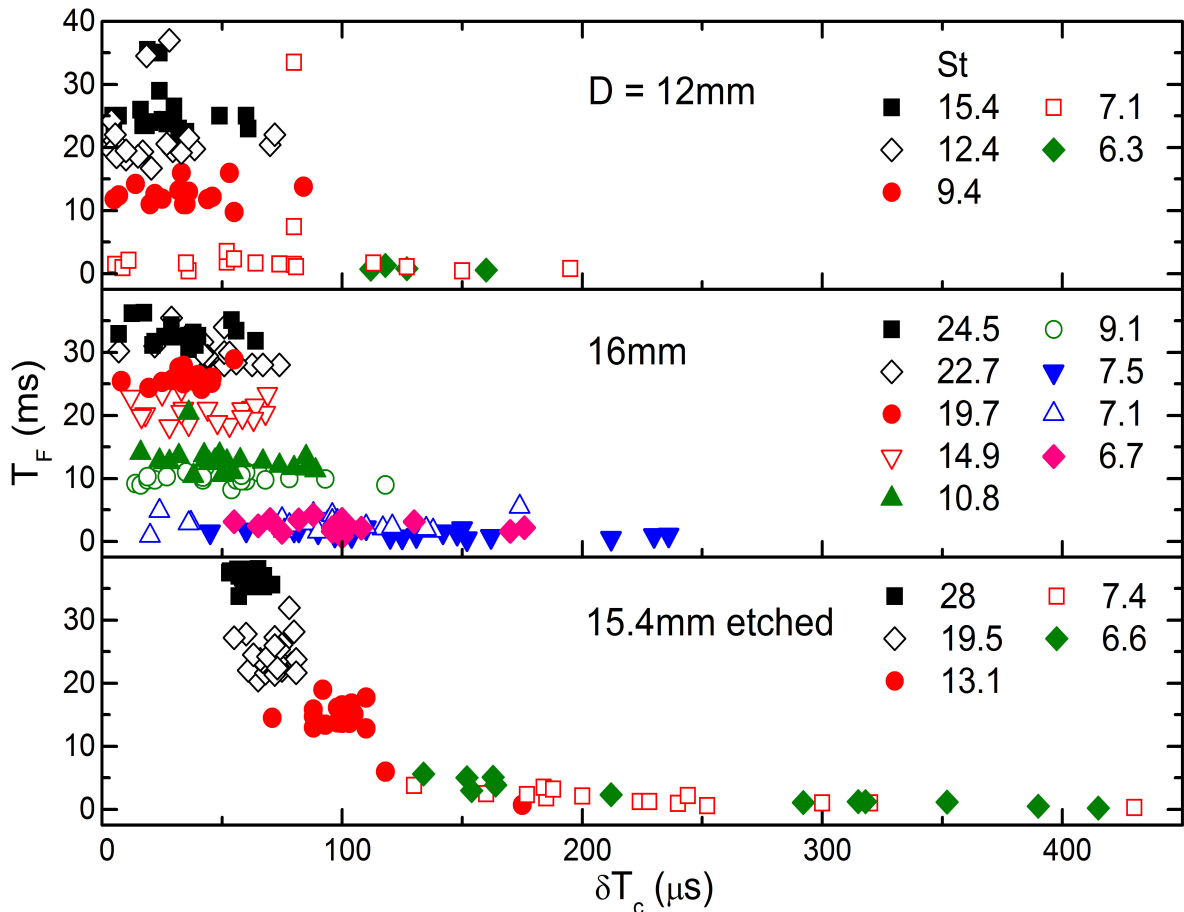
Fig. 2.7 Flight time vs contact time for $D = 16$ mm un-etched, 12 mm and 15.4 mm etched balls. Notice the increase in the scatter at lower St.

Thus far, we have discussed mean values of the contact duration and flight times, averaged over experimental trials at fixed St. However, the distribution of δT_c and T_F reveals the source of dissipation. In Figure 2.7 we plot T_F versus δT_c for St varying from just above St_c to about $St = 28$. In most cases, we find a broad distribution of contact times varying by up to an order of magnitude, at a fixed value of St. Presumably this reflects the variation in the local topography of the sphere. Remember that 16 mm and 12 mm spheres have inhomogeneous roughness whereas the etched sphere of 15.4 mm has homogeneous roughness and, therefore, shows much less scatter in contact times. We, however, find much smaller variability in the flight time, particularly at larger St for all the three spheres. Thus the total dissipation in the sphere-wall encounter, as reflected by the flight time, is not strongly affected by the duration of solid-on-solid contact. This indicates that despite solid contact, the bulk of kinetic energy is lost to fluid dissipation.

At large Stokes numbers, a different trend sets in, most clearly observed in the etched spheres: the contact time T_c becomes narrowly distributed. We suggest that at large impact speeds, the effective radius of the Hertzian contact increases, and averages over the roughness of the etched sphere (see appendix A: Hertzian calculation). Thus collisions at different locations become similar in their contact mechanics and no longer depend on local roughness. We anticipate another regime at even higher St where the dissipation becomes solid-dominated (as in a ball bouncing in the air), but we do not observe that regime. At the largest St, we observe plastic deformation in the form of pitting at the point of impact (more details are in appendix A: Hertzian calculation).

Direct solid contact is likely to be a general feature, even close to the threshold of bouncing. In this regime, the dissipation remains dominated by fluid mechanics, while the duration of the contact is largely controlled by surface and bulk properties of the solids. Even though solid dissipation does not play a prominent role, the presence of solid-to-solid contact is of great significance in contexts such as wear, charge transfer, or chemical reactivity of solids in suspension.

We do not observe a case where no contact was made by the sphere with the bottom wall in a finite time. Even at the smallest Stokes number we studied ($St = 5$), the contacts with the bottom wall were made which persist throughout the time. However, it is difficult to speculate what will happen at very low Stokes number ($St < 1$) and if we will see contact in a finite time or not.

2.5 Effect of electrical forces

In order to verify that electrical forces do not play any role in the mechanics of contact, we compared our results for a fixed Stokes number St at different AC voltages and frequency. We did not find any systematic dependence on the duration of contact or flight time with applied voltage or frequency. Results obtained with DC measurements were found to be similar to AC measurements.
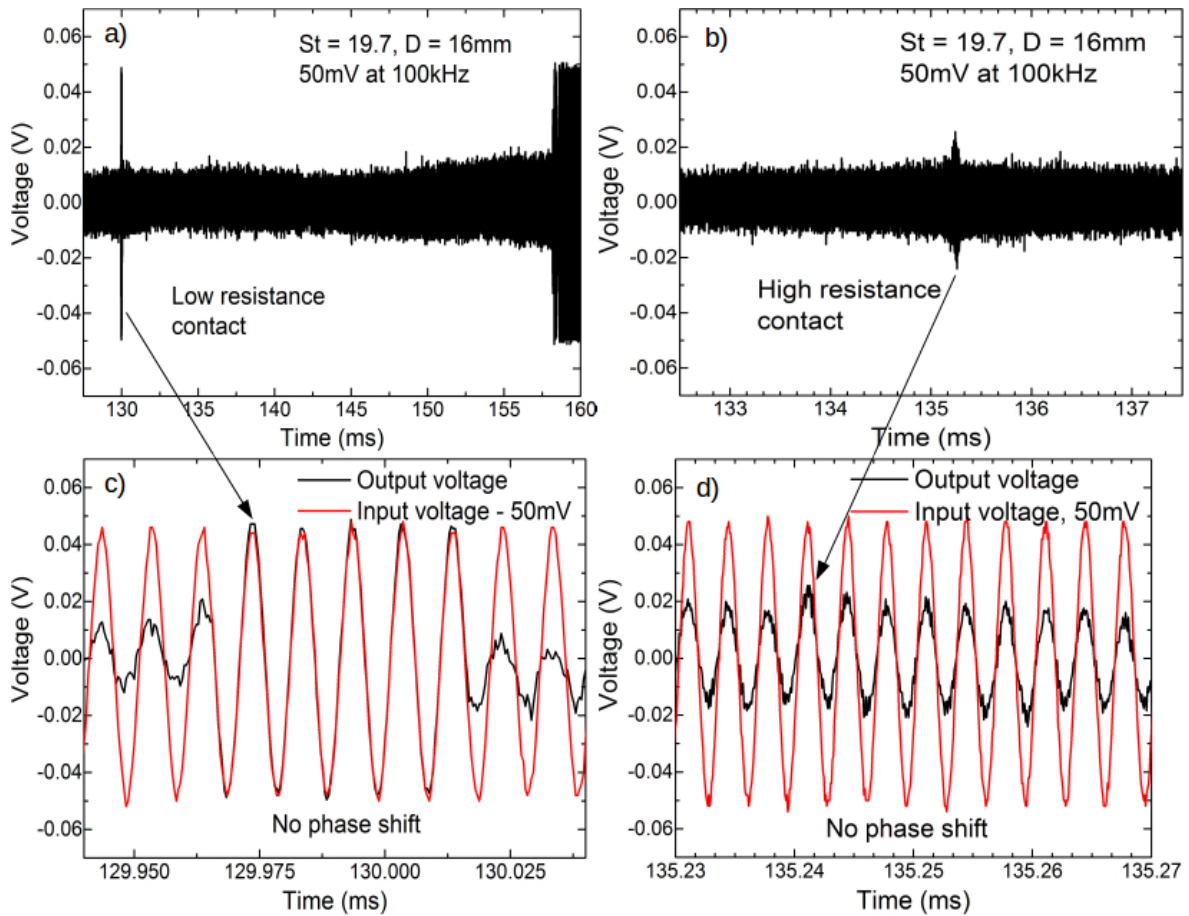
Fig. 2.8 (a) Low-resistance contact and (b) high-resistance contact at 50 mV, 100 kHz and $St = 19.7$. Panel (c) and (d) are the zoomed-in version of contacts shown in panel (a) and (b). The voltage shown in black is measured by a digital oscilloscope across a 220 kΩ resistor. In panel (a) and (c), the output voltage is equal to the source voltage (shown in red) of 50 mV suggesting that there is no voltage drop across the contact and the contact has very low resistance. However, in panel (b) and (d), the output voltage is lower than the source voltage suggesting that some contacts obtained during the experiments have high resistance. Notice the zero phase shift in both cases.

We used the same circuit as discussed before, Figure 2.1 (a). The output voltage was measured across a 220 kΩ resistor, R_s. This meant that if the contact resistance, R_c, is very low all the voltage drop would occur across R_s. This indeed was observed in a majority of the experiments. An example has been shown in Figure 2.8 (a) and a zoomed-in version of this contact is visible in Figure 2.8 (c). The output voltage (shown in black) is equal to the applied voltage of 50 mV (shown in red) suggesting that no voltage drop occurs across the contact. Such contacts will be called "low resistance contacts". In the rest of the experiments, we observed a significant voltage drop occurring across the contact. Hence, the voltage measured across the oscilloscope is less than the applied voltage as is visible in Figure 2.8 (b) and 2.8 (d). This suggests that R_c is of the same order as R_s in these cases. Such contacts were termed as "high resistance contacts". The measurements shown in Figure 2.8 were taken at $St = 19.7$, 100 kHz for 16 mm sphere. Contacts were found to be purely resistive as can be seen from the fact that there is zero phase difference between the applied voltage and output voltage across R_s in Figure 2.8, panels (c) and (d).

In Figure 2.9, we have made measurements as a function of the amplitude of the applied AC voltage for the same Stokes number as above ($St = 19.7$) and $D = 16$ mm. The applied AC voltage was varied from 50 mV to 10 V. The fraction of low resistance contact ($R_c << R_s$) was found to be lower than unity, implying that high resistance contact occurs in some of the trials. When high resistance contacts are also included, the contact percentage becomes one and does not vary with applied voltage. We point out that the fraction of high resistance contacts is variable and can be affected by many factors such as the impurity content of the oil, aging of the surface electrical properties and topography of the sphere following repeated collisions.

As is evident from Figure 2.9, no systematic dependence of contact time [panel (b)] and flight time [panel (c)] on electrical voltage was observed. This suggests that electrical forces do not play a role in the dynamics of the collision. In particular, there is no observed change in the nature of the electrical signal, arguing that dielectric breakdown of silicone oil does not occur during the collision process. The literature value of the breakdown voltage is high but finite (> 40 MV/m), so perhaps breakdown is avoided due to the very short time-scales of interaction. We thus infer that the values of contact time, flight time and contact fraction reported in this article are independent of the voltage applied.
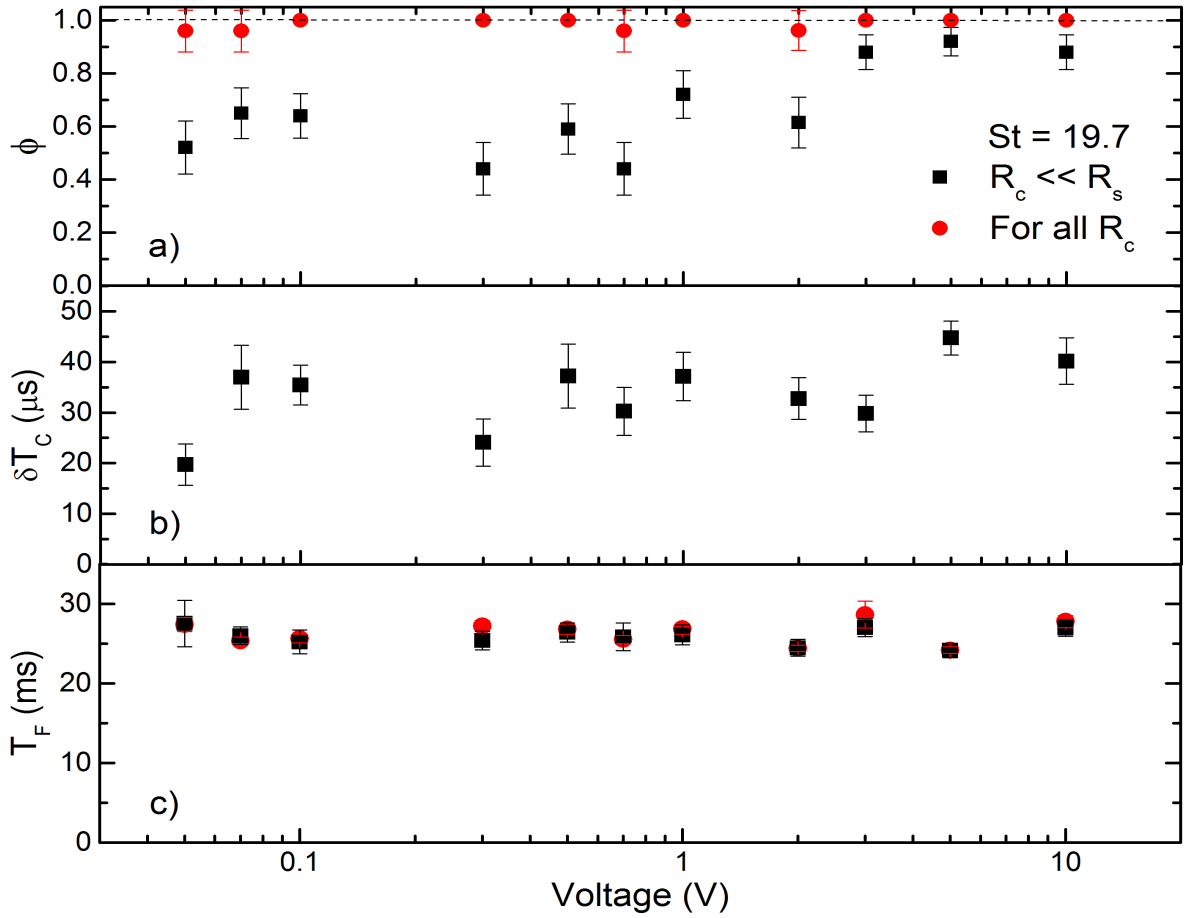
Fig. 2.9 There appears to be no systematic effect of the electrical voltage on the duration of contact [panel (b)] or on the intervals between bounces [panel (c)]. This experiment was carried out at 300 kHz, $St = 19.7$. The total measured contact fraction [panel (a)] remains close to one. The fraction of low resistance contacts (black squares) is lower. Error bars are the standard deviation of measurements in panel (a) and standard error of measurements in panel (b) and (c) taken at fixed Stokes numbers. Wherever the error bars are not visible, errors are smaller than symbol size.
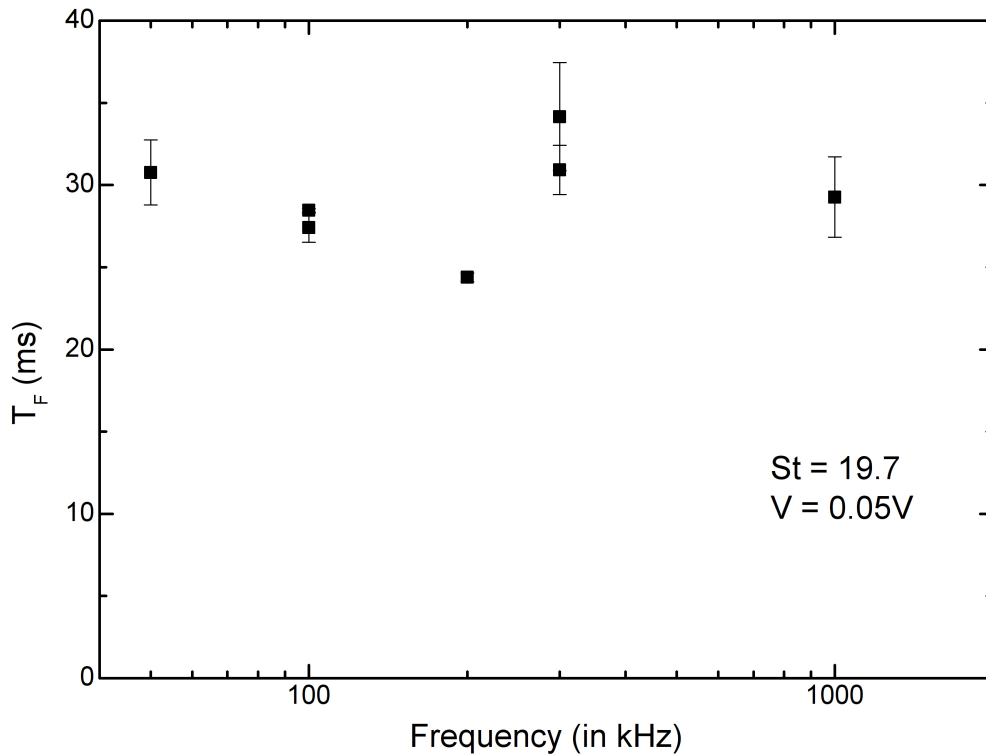
Fig. 2.10 Variation in flight time with frequency. No systematic trend was observed and contact fraction was found to be equal to one for all values of frequencies.

The dependence on frequency (50 to 1000 kHz) of the applied voltage was also studied and is shown in Figure 2.10. No systematic trend in the duration of contact, flight time and contact fraction were observed. Figure 2.10 shows that there is no significant change in flight time with frequency. As mentioned before, the contact fraction, when both low resistance contacts and high resistance contacts are included, was found to be close to one for all values of applied frequencies at $St > St_c$.

While the data make a clear case for solid-on-solid contact in all the spheres used, the $St-$dependence of the details of the bounce appears to be influenced by the surface quality of the sphere. This leads one to question whether our conclusions are valid for spheres that are even smoother than the ball bearings employed here. The next chapter is illuminating in this regard.

Chapter 3

Going beyond lubrication theory

To understand the contradiction between our electrical measurements from the last chapter and lubrication theory, we revisit lubrication theory with a goal of releasing some of the assumptions it is based upon. Equation 1.3 in the first chapter predicts that a falling sphere will approach the bottom wall infinitely slowly. While the decelerating force diverges as $h_o \to 0$ [recall that $h_o = h(r = 0, t)$ as shown in Figure 3.1], the velocity in the numerator also decreases, and the ratio of $\dot{h}_o/h_o$ produces this result.
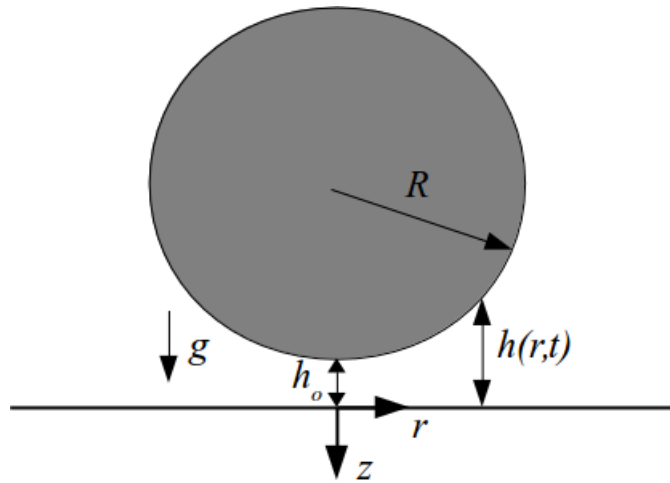
Fig. 3.1 A sphere approaching a plane, where r and z are the radial and vertical directions, respectively, $D = 2R$ is the diameter of the sphere, g is the acceleration due to gravity, and $h(r, t)$ is the time-dependent distance between the sphere and the bottom wall.

In the lubrication approximation, both the surfaces approaching each other are considered to be flat and streamwise derivatives are neglected as discussed in Chapter 1. Under this approximation, one obtains similarity profile in velocity, i.e., the radial velocity always has the same parabolic form at all radii. In our analysis in this chapter, we account

exactly for the shape of the object. We define a new non-orthogonal coordinate system (η, ζ) in which the variation in shape (h) of the sphere with the radial coordinate is considered. Besides this, explicit first-order streamwise derivatives are also considered. In other words, we make a boundary layer approximation and also allow for weak departures from the similarity of the velocity profile. Using this, we obtain a single parametric differential equation which provides the velocity profiles at different radii at a given time. The advantage of this new non-orthogonal coordinate system is that we are able to solve our final equation as a succession of parametric ordinary differential equations. The radial velocity profiles are then used to solve for the pressure and the sphere's acceleration.

3.1   Falling sphere

We start by adopting the cylindrical coordinate system as shown in Figure 3.1 and using the streamfunction-vorticity formulation. The axisymmetric continuity equation in this coordinate system is:

$$\frac{1}{r}(ru)_r + v_z = 0, \tag{3.1}$$

where u and v are the velocities in the radial r (parallel to the wall) and z (normal to the wall) directions, respectively and subscripts denote derivatives with respect to that coordinate. Using the continuity equation, we can define the streamfunction, ψ, by

$$2\pi r u = \psi_z; \qquad 2\pi r v = -\psi_r. \tag{3.2}$$

Now writing the axisymmetric Navier-Stokes equation for the r and z components (assuming that there is no flow in the azimuthal direction and the flow is axisymmetric),

$$\rho_f\Big(u_t + uu_r + vu_z\Big) = -p_r + \mu\Big(u_{rr} + \frac{u_r}{r} - \frac{u}{r^2} + u_{zz}\Big); \tag{3.3}$$

$$\rho_f\Big(v_t + uv_r + vv_z\Big) = -p_z + \mu\Big(v_{rr} + \frac{v_r}{r} + v_{zz} - \rho_f g\Big), \tag{3.4}$$

where t denotes time.

To eliminate pressure from the above equations, we take the derivative of equation 3.3 with respect to z and equation 3.4 with respect to r and take their difference, which yields:

$$\rho_f\Big[\big(u_z - v_r\big)_t + u\big(u_z - v_r\big)_r + v\big(u_z - v_r\big)_z + u_r\big(u_z - v_r\big) + v_z\big(u_z - v_r\big)\Big]$$
$$= \mu\Big[\big(u_z - v_r\big)_{rr} + \frac{1}{r}\big(u_z - v_r\big)_r + \big(u_z - v_r\big)_{zz} - \frac{1}{r^2}\big(u_z - v_r\big)\Big]. \tag{3.5}$$

Using the definition of vorticity ω,

$$\omega = u_z - v_r, \tag{3.6}$$

in equation 3.5, we get,

$$\rho_f\Big(\omega_t + u\omega_r + v\omega_z + \omega\big(u_r + v_z\big)\Big) = \mu\Big(\omega_{rr} + \frac{1}{r}\omega_r - \frac{\omega}{r^2} + \omega_{zz}\Big). \tag{3.7}$$

Now, using the definition of streamfunction in this equation, we finally obtain

$$\rho_f\left(r\frac{\partial \omega_d}{\partial t_d} + \frac{1}{2\pi}\frac{\partial \psi_d}{\partial z}\frac{\partial \omega_d}{\partial r} - \frac{1}{2\pi}\frac{\partial \psi_d}{\partial r}\frac{\partial \omega_d}{\partial z} - \frac{1}{2\pi}\frac{\omega_d}{r}\frac{\partial \psi_d}{\partial z}\right) = \mu r\left(\frac{\partial^2 \omega_d}{\partial r^2} + \frac{1}{r}\frac{\partial \omega_d}{\partial r} - \frac{\omega_d}{r^2} + \frac{\partial^2 \omega_d}{\partial z^2}\right), \tag{3.8}$$

where the subscript d has been included just to show that all the variables are dimensional in the equation. Derivatives have been mentioned explicitly, rather than by subscript. As the sphere approaches the bottom wall, the fluid gets squeezed out. The flow rate $Q(r,t)$ across the gap at some radius r is given by

$$Q(r,t) = 2\pi r \int_0^{h(r,t)} u(r,t)dz = 2\pi U(r,t)rh(r,t), \tag{3.9}$$

where $U(r,t)$ is the vertically averaged velocity at any r and t and where $h(r,t)$ is the distance between the sphere and the bottom wall at some radius. By geometry, this is given by

$$h(r,t) = h_o + R - \sqrt{R^2 - r^2}. \tag{3.10}$$

Note that at $r = 0, h(r,t) = h_o(t)$.

We now define a suitable non-orthogonal coordinate system:

$$\eta \simeq \frac{z}{h(r,t)}; \quad d\zeta \simeq \frac{dr}{h(r,t)}; \quad t \simeq t_d\frac{v_c}{R}. \tag{3.11}$$

Note the non-standard way of defining the streamwise coordinate. This simplifies our final equation and allows us to eliminate higher-order terms in a consistent manner. Here v_c would have been the velocity of the sphere at $h_o = 0$ had there been no bottom wall, and is obtained by solving the equation of motion of the sphere under gravity, buoyancy and viscous drag using an empirical formula given in Chapter 2 equation 2.1. This coordinate system accounts for the curvature of the sphere, unlike the lubrication approximation where h is considered independent of r. In this new coordinate system,

the vertical coordinate η varies from 0 at the bottom wall to 1 at the sphere's surface, at all r.

We non-dimensionalise ψ and ω using the following transformations:

$$\psi = \frac{\psi_d}{Q}; \quad \omega = \omega_d \frac{h}{U} = \frac{\omega_d}{f}. \tag{3.12}$$

Global continuity is imposed by prescribing that ψ varies from 0 at $\eta = 0$ to 1 at $\eta = 1$. Using global continuity, the flow rate can be written in terms of the fluid displaced by the sphere as it approaches the wall:

$$Q(r,t) = -2\pi R(h(r,t) - h_o)\dot{h_o}, \tag{3.13}$$

where the dot represents the derivative in time t.

Using this new coordinate system and non-dimensionalization, we find a solution in the region where $h_o \ll r \ll R$. and hence our solution will not be valid for $r \sim O(h_o)$ or smaller, and when $r \sim R$. Since we are interested in the dynamics of the sphere when it is very close to the plate (h_o is very small), the region $r \leq O(h_o)$ constitutes an extremely small fraction of the spherical area over which pressure acts. The force contributions from this region can be neglected consequently, and also because the pressure maximum happens not to lie within this region. Even when $r \sim R$, the pressure contribution is very small because of the large gap size. Thus, the region where $h_o \ll r \ll R$, gives most of the contribution to the pressure force and is important to study.

Using equation 3.11, we can write the radial derivative as:

$$\frac{\partial}{\partial r} = -\frac{\eta h_r}{h}\frac{\partial}{\partial \eta} + \frac{1}{h}\frac{\partial}{\partial \zeta}. \tag{3.14}$$

Now, we make the assumption that $h_o/R \ll 1$, and denote it by δ. This is a fair assumption when the sphere is close to the bottom wall. From equation 3.10 and in the region where $r \ll R$, one can see that h/R is of the same order as r^2/R^2 as δ is very small. In the region $h_o \ll r \ll R$, the equations below elucidate the scaling.

$$h = h_o + \frac{r^2}{2R} - \frac{1}{8}\frac{r^4}{R^3} + ...; \tag{3.15}$$

$$\frac{h}{R} = \frac{h_o}{R} + \frac{r^2}{2R^2} - \frac{1}{8}\frac{r^4}{R^4} + ...; \tag{3.16}$$

$$\frac{h}{R} = \delta + \frac{r^2}{2R^2} - ... \qquad . \tag{3.17}$$

Taking r^2/R^2 to be of $O(\epsilon)$, where $\epsilon \ll 1$ but for $\delta \ll \epsilon$, we can determine that h/r is of $O(\sqrt{\epsilon})$.

$$\frac{h}{r} = \frac{h}{R}\frac{R}{r} = O(\sqrt{\epsilon}). \tag{3.18}$$

This gives,

$$h_r(r,t) = \frac{r}{\sqrt{R^2 - r^2}} \sim \frac{r}{R} \sim \sqrt{\epsilon} + \text{higher order}. \tag{3.19}$$

This makes all the terms of equation 3.14 $\sim \frac{1}{h}(\sqrt{\epsilon}$ order) as $\partial/\partial\zeta$ is $\sim O(h/r)$ which is $\sim O(\sqrt{\epsilon})$. The second derivative of $h(r,t)$ with respect to r is:

$$h_{rr}(r,t) = \frac{r^2}{(R^2 - r^2)^{3/2}}. \tag{3.20}$$

Using equation 3.20 and approximations as mentioned above, one can obtain that all the terms of $\partial/\partial r^2$ are of order $\frac{1}{h^2}\epsilon$:

$$\frac{\partial^2}{\partial r^2} = \frac{1}{h^2}(\text{all } \epsilon \text{ order terms}). \tag{3.21}$$

In addition, we also have:

$$\frac{\partial}{\partial z} = \frac{1}{h}\frac{\partial}{\partial\eta}; \tag{3.22}$$

and

$$\frac{\partial}{\partial t_d} = \dot{\zeta}\frac{\partial}{\partial\zeta} - \frac{\eta\dot{h}_o}{h}\frac{\partial}{\partial\eta} + \frac{v_c}{R}\frac{\partial}{\partial t}. \tag{3.23}$$

where subscript d denotes that time is dimensional and the dot on ζ and h_o represent partial derivative and total derivatives in time respectively. Having discussed the scaling for $h_o/R \ll 1$, we now go back to equation 3.8. Let us substitute the expressions for ψ_d and ω_d from equation 3.12 into equation 3.8. We get:

$$\rho_f\left(rf\frac{\partial\omega}{\partial t_d} + r\omega\frac{\partial f}{\partial t_d} + \frac{Q}{2\pi}\frac{\partial\psi}{\partial z}\left(f\frac{\partial\omega}{\partial r} + \omega\frac{\partial f}{\partial r}\right) - \left(Q\frac{\partial\psi}{\partial r} + \psi\frac{\partial Q}{\partial r}\right)\frac{f}{2\pi}\frac{\partial\omega}{\partial z} - \frac{fQ\omega}{2\pi r}\frac{\partial\psi}{\partial z}\right)$$
$$= \mu r\left(f\frac{\partial^2\omega}{\partial r^2} + 2\frac{\partial\omega}{\partial r}\frac{\partial f}{\partial r} + \omega\frac{\partial^2 f}{\partial r^2} + \frac{f}{r}\frac{\partial\omega}{\partial r} + \frac{\omega}{r}\frac{\partial f}{\partial r} - \frac{f\omega}{r^2} + f\frac{\partial^2\omega}{\partial z^2}\right). \tag{3.24}$$

Now, using equations 3.14, 3.22 and 3.23, we get

$$
\rho_f\left[rf\left(\dot{\zeta}\omega_\zeta - \frac{\eta\dot{h_o}}{h}\omega_\eta + \frac{v_c}{R}\omega_t\right) + r\omega\dot{f} + \frac{Qf}{2\pi h^2}\psi_\eta\omega_\zeta + \frac{Q\omega}{2\pi h}f_r\psi_\eta - \frac{Qf}{2\pi h^2}\psi_\zeta\omega_\eta - \frac{\psi f}{2\pi h}Q_r\omega_\eta - \right.
$$
$$
\left. \frac{fQ\omega}{2\pi rh}\psi_\eta\right] = \mu r\left[f\omega_{rr} + 2f_r\omega_r + \omega f_{rr} + \frac{f}{r}\left(-\frac{\eta h_r}{h}\omega_\eta + \frac{1}{h}\omega_\zeta\right) + \frac{\omega}{r}f_r - \frac{f\omega}{r^2} + \frac{f}{h^2}\omega_{\eta\eta}\right].
$$
$$(3.25)$$

From the definition of vorticity, we have

$$
\omega_d = \frac{1}{r}\frac{\partial^2\psi_d}{\partial z^2} + \frac{1}{r}\frac{\partial^2\psi_d}{\partial r^2} - \frac{1}{r^2}\frac{\partial\psi_d}{\partial r}.
$$
$$(3.26)$$

Using equations 3.11 and 3.12, and shifting to non-dimensional coordinates, we get:

$$
\omega f = \frac{Q}{rh^2}\psi_{\eta\eta} + \frac{Q}{r}\psi_{rr} + \frac{2}{r}Q_r\psi_r + \frac{\psi}{r}Q_{rr} - \frac{\psi}{r^2}Q_r - \frac{Q}{r^2}\psi_r;
$$
$$(3.27)$$

From the scaling of $h/R \sim O(\epsilon)$ and $h/r \sim r/R \sim O(\sqrt{\epsilon})$, we get:

$$
\omega = 2\pi\frac{\partial^2\psi}{\partial\eta^2} + (\text{all } \epsilon \text{ order terms}).
$$
$$(3.28)$$

To simplify the equation 3.25, we non-dimensionalize all lengths (h_o and h) by R, velocities ($\dot{h_o}$) by v_c, and acceleration ($\ddot{h_o}$) by v_c^2/R. We now evaluate each term separately by using $h/R \sim O(\epsilon)$, $r^2/R^2 \sim O(\sqrt{\epsilon})$ and $\partial/\partial\zeta \sim O(h/r) \sim O(\sqrt{\epsilon})$ and find that all the terms, except for the last term, on the right-hand side of the equation 3.25 are small and thus can be neglected. Retaining all the terms on the left-hand side and using equation 3.28, we get:

$$
\frac{\rho_f rf\dot{h_o}}{h}\left[\frac{h\dot{\zeta}}{\dot{h_o}}\psi_{\eta\eta\zeta} - \eta\psi_{\eta\eta\eta} + \frac{h}{\dot{h_o}}\psi_{t\eta\eta} + \left(\frac{\ddot{h_o}h}{\dot{h_o}^2} - 2\right)\psi_{\eta\eta} - \frac{(h-h_o)}{rh}(\psi_\eta\psi_{\eta\eta\zeta} - \psi_\zeta\psi_{\eta\eta\eta})\right.
$$
$$
\left. -\left(\frac{h_r}{r}\frac{2h_o-h}{h} - \frac{2(h-h_o)}{r^2}\right)\psi_{\eta\eta}\psi_\eta + \frac{h_r}{r}\psi\psi_{\eta\eta\eta}\right] = \mu r\left[\frac{f}{h^2}\psi_{\eta\eta\eta\eta} + \epsilon\right].
$$
$$(3.29)$$

After rearranging the terms, we get:

$$
\begin{aligned}
\Bigg[\frac{h\dot\zeta}{\dot h_o} \psi_{\eta\eta\zeta} - \eta\psi_{\eta\eta\eta} + \frac{h}{\dot h_o}\psi_{t\eta\eta} + \left(\frac{\ddot h_o h}{\dot h_o{}^2} - 2\right)\psi_{\eta\eta} - \frac{(h-h_o)}{rh}(\psi_\eta\psi_{\eta\eta\zeta} - \psi_\zeta\psi_{\eta\eta\eta}) \\
- \left(\frac{h_r}{r}\frac{2h_o - h}{h} - \frac{2(h-h_o)}{r^2}\right)\psi_{\eta\eta}\psi_\eta + \frac{h_r}{r}\psi\psi_{\eta\eta\eta}\Bigg] = \frac{1}{Re}\left[\frac{1}{hh_o}\psi_{\eta\eta\eta\eta}\right],
\end{aligned} \qquad (3.30)
$$

where $Re = \rho_f v_c R/\mu$ is the Reynolds number of the sphere. The no-slip and no penetration boundary conditions for equation 3.30 are:

$$
\begin{aligned}
\psi(\eta = 0, \zeta, t) = 0; &\quad \psi(\eta = 1, \zeta, t) = 1; \\
\psi_\eta(\eta = 0, \zeta, t) = 0; &\quad \psi_\eta(\eta = 1, \zeta, t) = 0.
\end{aligned} \qquad (3.31)
$$

Thus, apart from allowing for the first-order variations in the streamwise direction, we explicitly include the effect of the acceleration of the body. Thus our formulation has several improvements over lubrication theory. If we set all the left-hand side terms to zero, we get $\psi_{\eta\eta\eta\eta} = 0$, i.e. the equation reduces to lubrication theory. The result is a parabolic radial velocity profile at all t and r. Therefore, the lubrication theory comes out to be a special case of the present formulation.

We use a double shooting method for numerically solving equation 3.30 in an approach similar to Govindarajan and Narasimha (1995). Our first guess is obtained by neglecting the streamwise (ζ) and time derivatives. This leaves a fourth-order ordinary differential in η with two boundary conditions at $\eta = 0$ and two boundary conditions at $\eta = 1$. This boundary value problem (BVP) can be solved by a shooting method which converts a BVP into a system of initial value problems. We start with two known boundary conditions at $\eta = 0$ ($\psi(\eta = 0, \zeta, t) = 0$ and $\psi_\eta(\eta = 0, \zeta, t) = 0$) and two guess conditions for $\psi_{\eta\eta}$ and $\psi_{\eta\eta\eta}$ at $\eta = 0$. We then use Mathematica which employs the Newton-Raphson method to update guess conditions until we get desired boundary conditions on the boundary at $\eta = 1$.

We obtain such solutions at a given time, at two closely spaced streamwise locations of ζ and $\zeta + \Delta\zeta$, and at two close time instants of t and $t + \Delta t$. The differences in the two solutions, when appropriately scaled, give us an estimate of the necessary derivatives in ζ and t. This estimate is fed into the next iteration, and the process is repeated until we obtain a converged solution of ψ as a function of η for a given ζ and t. The complete solution over all radial locations and time may be obtained by sweeping the $\zeta - t$ space in this manner.
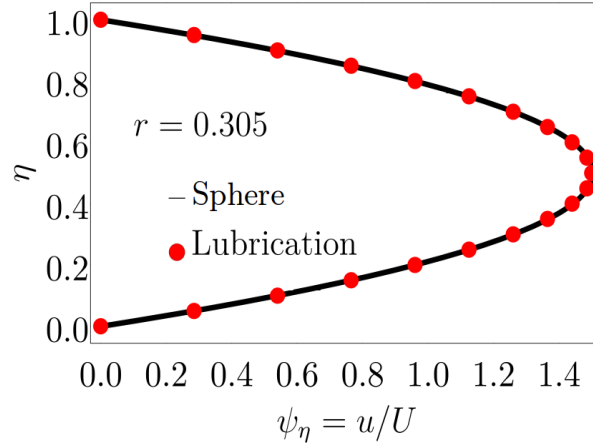
Fig. 3.2 Normalized radial velocity profile at $r = 0.305R$ for $St = 11$ at $h_o = 0.0007R$. The instantaneous velocity $\dot{h}_o$ at this time instant is $0.6v_c$ and the non-dimensional acceleration is $77v^2/R$. The lubrication theory is used to obtain these values of h_o, $\dot{h}_o$ and $\ddot{h}_o$. These values correspond to Stokes number $St = 2\rho_s v_c R/9\mu = 11$, Reynolds number $Re = \rho_f v_c R/\mu$, Froude number $Fr = v_c^2/Rg = 1$ and density ratio $d_r = \rho_f/\rho_s = 0.127$. For example, if a sphere is dropped from $0.59R$ height with zero initial velocity, it will reach v_c velocity when the sphere reaches $h_o = 0$, if there was no bottom wall. For a given R, ρ_f, ρ_s and μ, the initial height of drop decides v_c and therefore the St, Re, and Fr. If a bottom wall was present, using lubrication theory it will reach $h_o = 0.0007R$ with $\dot{h}_o = 0.6v_c$ and $\ddot{h}_o = 77v^2/R$. The black curve is obtained by our new formulation for a falling sphere and the red curve represents the parabolic profile used in the lubrication theory for the same case. Even at a relatively large radius of 0.305, our approach shows that a parabolic velocity profile is supported under the sphere. This validates the lubrication approximation for this case.

Our method provides a novel way to obtain the radial velocity profile (as shown by the black curve in Figure 3.2) and hydrodynamic force on the sphere without neglecting unsteady and inertial terms. Only the highest contributing viscous term of equation 3.25 has been retained. The pressure in the gap and the hydrodynamic force on the sphere is obtained in a manner similar to that in the lubrication approximation and is given by:

$$p_r = -\frac{2}{Re}\frac{(h - h_o)\dot{h}_o}{rh^3}\psi_{\eta\eta\eta}, \tag{3.32}$$

$$F_p = \int 2\pi r p_r dr. \tag{3.33}$$

Here, pressure and the hydrodynamic force F_p have been non-dimensionalized by $\rho_f v_c^2/2$ and $\rho_f v_c^2 R^2/2$ respectively. This hydrodynamic force will then be used in a vertical-force
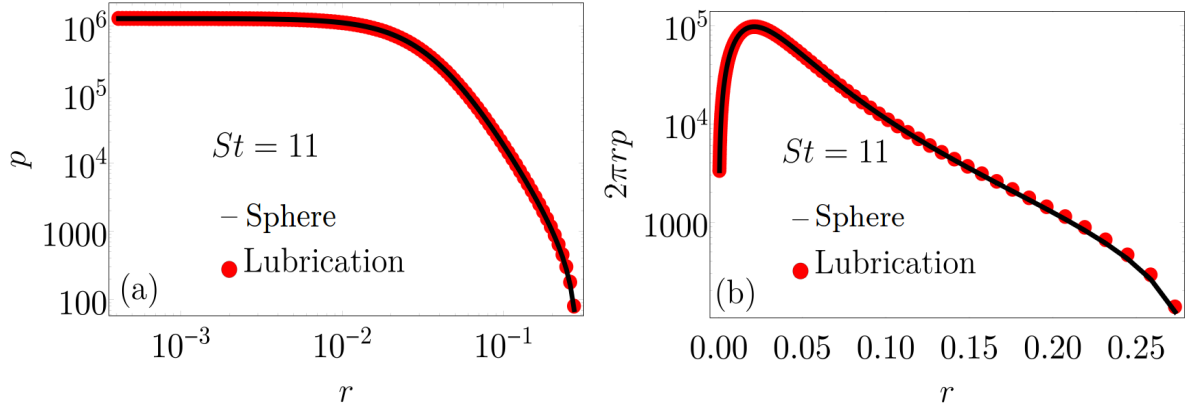
Fig. 3.3 (a) Pressure p and (b) $2\pi r p$ as functions of the radial coordinate for $St = 11$ at $h_o = 0.0007R$. Here r has been normalized by the radius of the sphere. The instantaneous velocity $\dot{h}_o$ at this time is $0.6v_c$ and the non-dimensional acceleration used in equation 3.30 is 77. These values correspond to $St = 11$, $Re = 6$, $Fr = 1$ and density ratio $d_r = 0.127$ (see Figure 3.2). The black curve is obtained by our new formulation for a falling sphere and the red is predicted by the lubrication theory. The pressure profiles and the force obtained by our formulation (black curves) are very close to those obtained under the lubrication approximation (red curve). As is visible in (b), the maximum of $2\pi r p$ lies in our region of study ($h_o \ll r \ll R$).

balance equation of motion containing gravity, buoyancy, viscous drag (Flagan and Seinfeld, 1988) and pressure force to get acceleration. In dimensional form this equation is similar to equation 2.1 in Chapter 2:

$$\rho_s V \ddot{h}_o = (\rho_s - \rho_f) V g - 3\pi\mu D \dot{h}_o (1 + 0.15 Re_{in}^{0.687}) - F_{p_d}, \tag{3.34}$$

where Re_{in} is defined by the dimensional instantaneous velocity of the sphere $\dot{h}_o v_c$, $Re = \rho_f \dot{h}_o D/\mu$. $F_{p_d} = F_p \rho_f v_c^2/2$ denotes the dimensional upward pressure force exerted by the fluid layer. As in equation 2.1, we use an empirical formula for the viscous drag in the absence of a bottom plate. In non-dimensional form, this equation is:

$$\ddot{h}_o = -\frac{1 - d_r}{Fr^2} - \frac{\dot{h}_o}{St}(1 + 0.15 Re_{in}^{0.687}) + \frac{3}{8\pi} d_r F_p, \tag{3.35}$$

where $d_r = \rho_f/\rho_s$ is the density ratio. $St = 2\rho_s v_c R/9\mu$ and $Fr = v_c^2/Rg$ are the Stokes number and Froude number of the particle respectively.

The pressure profiles and force obtained are very close to those obtained under the lubrication approximation as shown in Figure 3.3. This is because we find that the deviations from a parabolic velocity profile are significant only at large r, where the

contribution to upward pressure force is minimal. What is then causing the difference between theory and experiment? There are many other effects like those of higher-order streamwise derivatives, surface roughness and deformation which could be contributing.

3.2   Falling cone
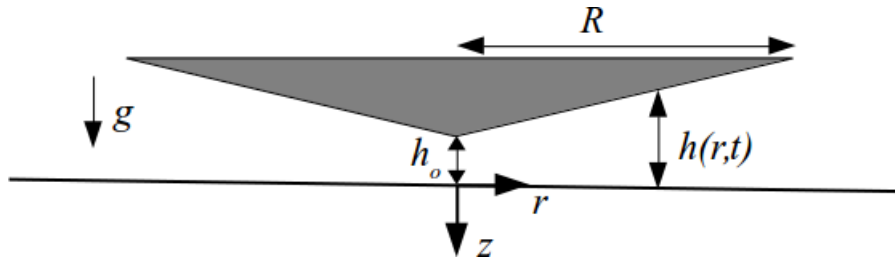
Fig. 3.4 A cone approaching a plane, where r and z are the radial and vertical coordinates respectively. R is the radius of the cone, g is the acceleration due to gravity, and $h(r,t)$ is the time-dependent distance between the cone and the bottom wall.

We can use the same methodology for a cone of radius R falling towards a bottom wall with the apex of the cone facing downwards as shown in Figure 3.4 and obtain a similarity solution. The geometry enables us to set all streamwise (ζ) derivatives to zero and thus the radial velocity supports a similarity profile. No scaling argument is necessary for this derivation.

The distance between the bottom wall and the surface of the cone $h(r,t)$ is given by

$$h(r,t) = h_o + cr, \tag{3.36}$$

where c is a constant defining the angle made by the cone walls with the horizontal axis and $h_o = h(r = 0, t)$ is the smallest distance between the cone and the bottom wall. Three different values of c are used in this analysis as shown in Figure 3.5(a) and (b). The global continuity equation gives us the flow rate $Q(r,t)$ by using identical arguments as employed to derive equations 3.9 and 3.13:

$$Q(r,t) = 2\pi U(r,t)rh(r,t) = -\pi rl\dot{h}_o, \tag{3.37}$$

where $l = r\sqrt{1 + c^2}$ is slant height of the cone and $U(r,t)$ is now the vertically averaged velocity for the cone at any r and t. Reverting to the non-orthogonal coordinate system employed earlier (equation 3.11), after non-dimensionalisation (see equation 3.12), we
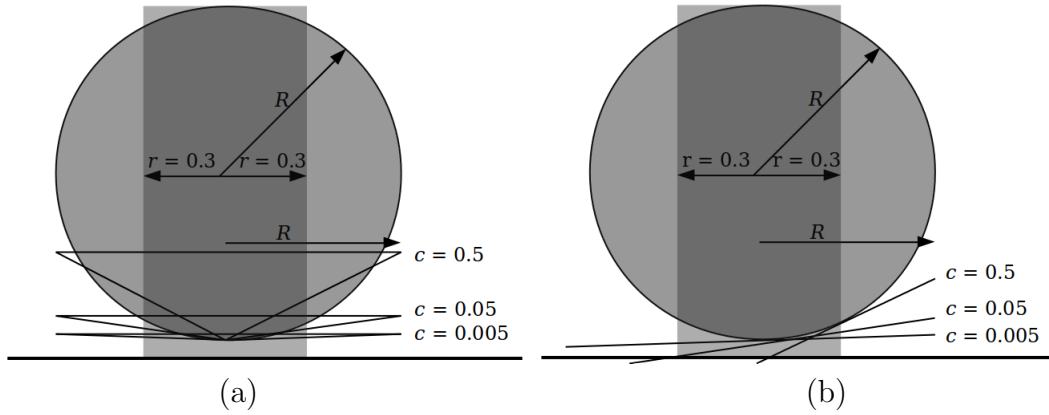
Fig. 3.5 (a) Comparison between a sphere and cones of different slopes ($c = 0.5$, 0.05 and 0.005) and same radius R. The rectangular shadowed region in middle represents the region ($h_o \ll r \ll R$) for which computation is performed. Notice that the cone with $c = 0.005$ is much flatter than the sphere. That is, on average the $c = 0.005$ cone has much smaller variation in height with r compared to the sphere. Cone with $c = 0.05$ has same order of magnitude variation in height with r compared to the sphere and $c = 0.5$ cone has much larger variation. (b) In a sphere, c is a function of r. Slopes $c = 0.5$, 0.05 and 0.005 are shown as tangents to the circle at different r. These tangent lines again help to understand the difference between different slope cones. Note that the cones drawn in (a) and tangent lines drawn in (b) are only for representation and are not to the actual scale.

can write the derivatives of cylindrical coordinates in terms of η and t after neglecting all the derivatives in ζ as:

$$\frac{\partial}{\partial r} = -\frac{\eta c}{h} \frac{\partial}{\partial \eta}, \tag{3.38}$$

$$\frac{\partial^2}{\partial r^2} = \frac{\eta^2 c^2}{h^2} \frac{\partial^2}{\partial \eta^2} + \frac{2\eta c^2}{h^2} \frac{\partial}{\partial \eta}, \tag{3.39}$$

$$\frac{\partial}{\partial t_d} = -\frac{\eta \dot{h}_o}{h} \frac{\partial}{\partial \eta} + \frac{v_c}{R} \frac{\partial}{\partial t}. \tag{3.40}$$

Here again, the subscript d is used for dimensional time. Note that v_c is the velocity of a sphere of radius R at $h_o = 0$, if there was no bottom wall. We continue to use v_c for non-dimensionalizing the velocity to compare the dynamics of a falling cone with that of a falling sphere. The derivative of z remains unchanged from the case of the falling sphere and is given by equation 3.22. Using this information and equation 3.24, we get the final equation for the cone after non-dimensionalizing all lengths (h_o and h) by R,
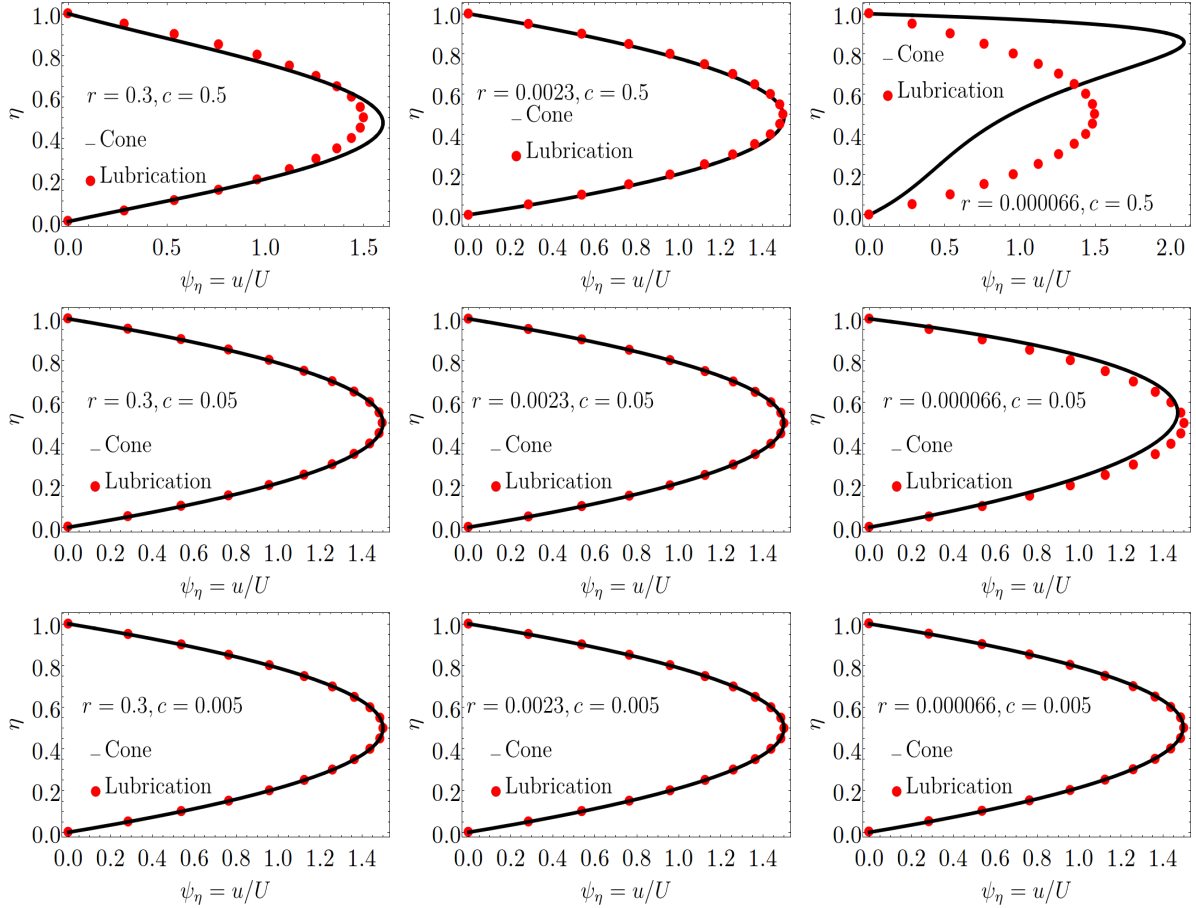
Fig. 3.6 Normalized radial velocity profile for $St = 11$ at $h_o = 0.0007R$. The instantaneous velocity $\dot{h}_o$ at this time is $0.6v_c$ and the non-dimensional acceleration used is 77. Here v_c is the velocity of a sphere of radius R at $h_o = 0$, if there was no bottom wall. We are still using v_c and the same values of h_o, $\dot{h}_o$ and $\ddot{h}_o$ as in Figure 3.2 to compare the results for a cone with the results for a falling sphere. These values correspond to $St = 11$, $Re = 6$, $Fr = 1$, and density ratio $d_r = 0.127$. The black curve is obtained by our new formulation for the cone and the red curve (parabolic velocity profiles) is from lubrication theory. The top panel shows the velocity profile for $c = 0.5$, the middle panel for $c = 0.05$, and the bottom panel for $c = 0.005$. Here r has been normalized by the radius of the cone. The normalized radius r at which the velocity profiles are observed decreases from left to right. The radius in all the left panels, middle panels, and the right panels is $r = 0.3$, 0.0022, and 0.000066 respectively.
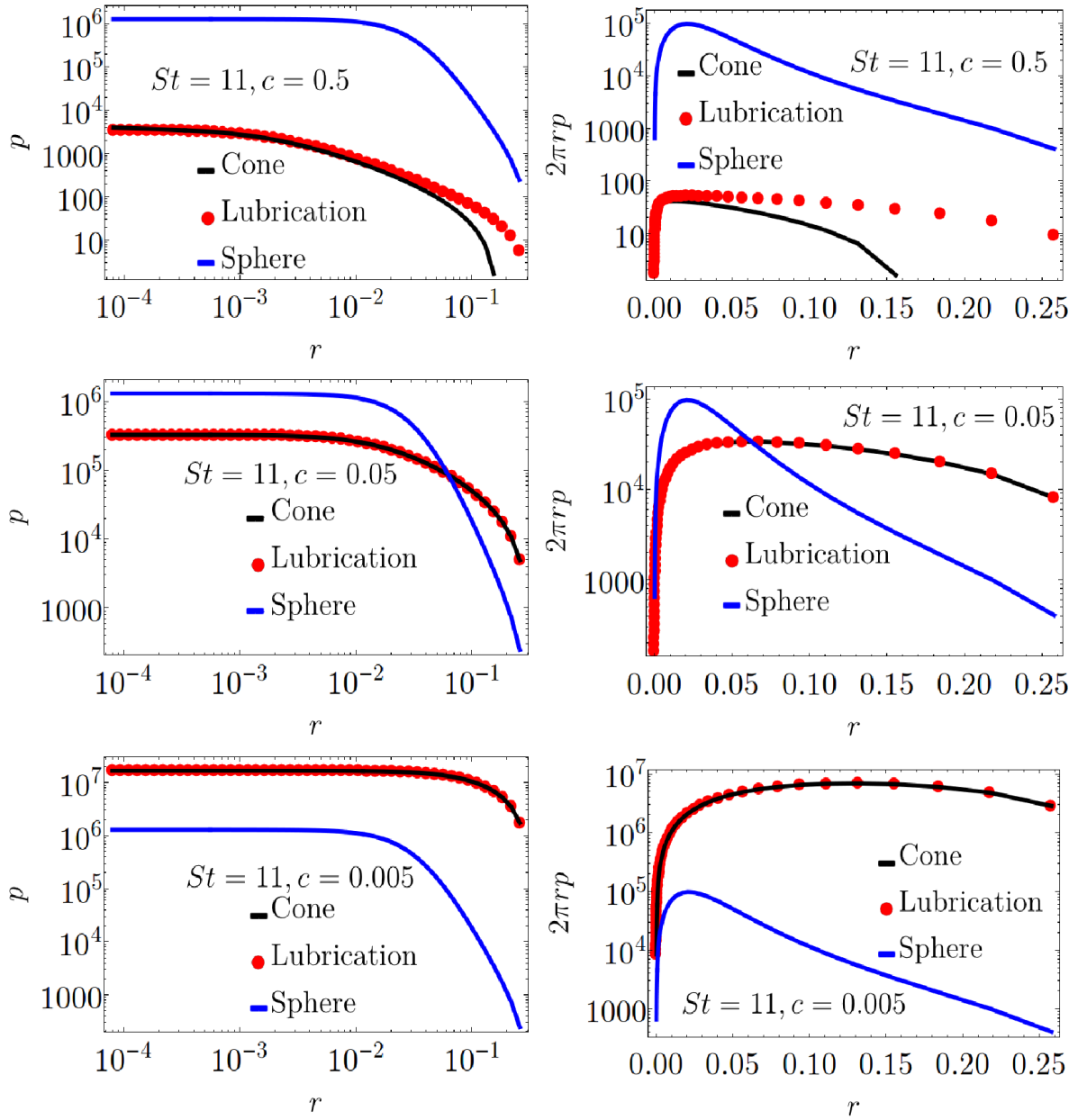
Fig. 3.7 Pressure p and $2\pi rp$ profiles for $St = 11$ at $h_o = 0.0007R$ as a function of the non-dimensional radial coordinate. The instantaneous velocity $\dot{h}_o$ at this time is $0.6v_c$ and the non-dimensional acceleration used in equation 3.41 is 77. We are still using the same values of h_o, $\dot{h}_o$ and $\ddot{h}_o$ as in the sphere case to compare the results for a cone with the results for a falling sphere. These values correspond to $St = 11$, $Re = 6$, $Fr = 1$, and density ratio $d_r = 0.127$. The black curve is obtained by our new formulation for a falling cone and the red dots are obtained by the lubrication theory for a falling cone. The blue curve is obtained by using lubrication theory for a falling sphere as shown in Figure 3.3. The top panel shows the profiles for $c = 0.5$, the middle panel for $c = 0.05$, and the bottom panel for $c = 0.005$.

velocities ($\dot{h}_o$) by v_c, and acceleration ($\ddot{h}_o$) by v_c^2/R:

$$-\eta\omega_\eta + \frac{h}{\dot{h}_o}\omega_t + \left(\frac{\ddot{h}_o h}{\dot{h}_o^2} - 2\right)\omega + l\left(\frac{c}{h} - \frac{1}{r}\right)\omega\psi_\eta + \frac{l}{r}\psi\omega_\eta = \frac{1}{\text{Re}}\frac{1}{h\dot{h}_o}\left[(1 + \eta^2 c^2)\omega_{\eta\eta}\right.$$
$$\left. + \left(4\eta c^2 - \frac{3h\eta c}{r}\right)\omega_\eta - \left(\frac{6hc}{r} - 6c^2\right)\omega\right], \qquad (3.41)$$

where $Re = \rho_f v_c R/\mu$ is the Reynolds number of the cone and the vorticity ω is obtained from equation 3.27 as:

$$\omega = 2\pi\left[(1 + \eta^2 c^2)\psi_{\eta\eta} + \left(2\eta c^2 - \eta c\frac{h}{r}\right)\psi_\eta\right] \qquad (3.42)$$

The boundary conditions given in equation 3.31 is applicable here as well. Equation 3.41 is solved to get the radial velocity profiles at different r and is shown in Figure 3.6. The top panel shows the normalized radial velocity for $c = 0.5$, the middle panel for $c = 0.05$ and the bottom panel for $c = 0.0005$. The radius is decreasing from left to right. Lubrication theory predicts parabolic radial velocity profile for both the sphere and the cone. The deviations from the parabolic profile are larger for the bigger values of c. At $c = 0.5$ and $r = 0.000066 < h_o$, we see larger deviations from the parabolic profile. At smaller values of c, the radial velocity profile is closer to a parabola. We use this radial velocity profiles in equation 3.3 to get the pressure between the cone and the bottom wall. Equation 3.3 gives us p_r in terms of ψ.

$$p_r = \frac{l}{h}\left(\ddot{h}_o - \frac{\dot{h}_o^2}{h}\right)\psi_\eta - \frac{l\dot{h}_o^2}{h^2}(\eta - 1)\psi_{\eta\eta} + \frac{l\dot{h}_o}{h}\psi_{\eta t} + \frac{l^2\dot{h}_o^2\eta c}{2h^3}\psi_{\eta\eta}\psi_\eta - \frac{l^2\dot{h}_o^2}{2h^2}\left(\frac{1}{r} - \right.$$
$$\left. \frac{c}{h}\right)\psi_\eta^2 + \frac{2}{\text{Re}}\left[\frac{-l\dot{h}_o}{2h^3}(1 + \eta^2 c^2)\psi_{\eta\eta\eta} + \frac{\eta l c\dot{h}_o}{h^2}\left(\frac{3}{2r} - \frac{2c}{h}\right)\psi_{\eta\eta} + \frac{lc\dot{h}_o}{h^2}\left(\frac{3}{2r} - \frac{c}{h}\right)\right] \qquad (3.43)$$

Note how the whole Navier-Stokes equation in the radial direction is used to get p_r, unlike in the case of the sphere in equation 3.38 where after using lubrication approximation $\psi_{\eta\eta\eta}$ proves to be bigger than all the other terms. Equation 3.33 gives us the final drag force on the cone, which is used in non-dimensional vertical force balance to get acceleration at each time-step:

$$\ddot{h}_o = -\frac{1 - d_r}{Fr^2} + \frac{3}{2\pi c}d_r F_p. \qquad (3.44)$$

The pressure profiles, and therefore the force obtained, depend strongly on the value of c as shown in Figure 3.7. The curves in the red represent the results obtained by the

lubrication theory for a cone falling towards a bottom wall whereas the curve in the blue shows the results for a falling sphere obtained by lubrication theory (see Figure 3.3). For $c = 0.5$, shown in the top panel of Figure 3.7, we see the pressure and $2\pi r p$ obtained for cone by our new formulation to be $O(10^3)$ smaller than the plots obtained by the lubrication theory for a falling sphere (shown in blue). At $c = 0.05$ (middle panel), the values of pressure for a falling cone are not that different from the values for a falling sphere and therefore the final forces are quite close to each other. At an even smaller value of $c = 0.005$ (bottom panel), the pressure obtained between the cone and the bottom wall proves to be much larger than that in the case of the sphere. This is true because a sphere at small r behaves like a disc as it has a very small slope h_r. But at larger r, the slope of the sphere increases and crosses $c = 0.005$, thus allowing the fluid between the sphere and the bottom wall to get squeezed out more easily. And hence at very small c, the force obtained for the falling sphere is smaller compared to that of the cone.

The results obtained by lubrication theory for a falling cone (shown in red in Figure 3.7) matches well with the results obtained by our formulation at lower values of c. At $c = 0.5$, lubrication theory over predicts the drag force on the cone. Hence, our new formulation shows that at a larger slope, the lubrication theory is not completely correct. Such larger slopes come at very large radial coordinates in the sphere. But for cone and similar geometries, our method provides a novel way to calculate the drag force on the object.

From Figure 3.7, we understand that the fluid is squeezed out more easily in a sphere than in a disc (or a cone with a very small slope) and even more easily in a cone with a large c than in a sphere. Therefore, one would expect that a cone approaching a bottom wall would be able to come in contact with the wall in finite time depending on the slope of the cone. But we already know from our experiments (Chapter 2) that even a sphere comes in contact with the bottom wall in a finite time before rebounding. In experiments, the process of squeezing out the fluid can be assisted by the surface roughness, which can be considered as conical objects on the surface of the sphere. The previous section 3.1 showed us that the dynamics of a smooth sphere falling towards a bottom wall is very close to that predicted by the lubrication theory for a falling sphere. Hence, the question arises whether we can observe contact just using the lubrication theory. The following section attempts to answer this.

3.3 Lubrication theory

We now return to the sphere. To compare the dynamics of the sphere with experimental observations, we again work in dimensional cylindrical coordinates (see Figure 3.1) and use the equation of motion for a smooth, rigid sphere approaching a plane under the lubrication approximation (Davis et al., 1986; Leal, 2007). The minimum vertical distance between ball and plate, $h_o = h(r = 0, t)$, can be determined from equation 3.45. The horizontal force balance between pressure gradient and viscous forces, as per lubrication approximation, is given by:

$$\frac{\partial p}{\partial r} + \mu \frac{\partial^2 u}{\partial z^2} = 0, \tag{3.45}$$

where $p(r, t)$ is the pressure. The radial velocity of the fluid u, squeezing out between the plate and the sphere is assumed to have a parabolic profile (Leal, 2007). To obtain the net pressure force F_p, we solve equation 3.45 using the relation given in equation 3.10 for the surface profile of a sphere.

Equation 3.34 is numerically solved to obtain $\dot{h}_o$ as a function of h_o and is shown by solid curves in Figure 3.8. In the calculation, we follow previous work by Davis et al. (1986), except that they had made the further assumption that the region near $r = 0$ may be modeled as a paraboloid rather than a sphere. The approximation of a paraboloid allows for analytic solutions, as shown by the dashed curves in Figure 3.8, that are quantitatively close to our numerical solutions for a sphere.

The asymptote, the portion for $St = 5.4$ and 6.95 that appears as a straight line in this figure, has a slope of -1. This may be referred to as the "lubrication phase" of the dynamics, where $\dot{h}_o$ decreases at the same rate as the increase in $1/h_o$ and consequently the hydrodynamic force remains constant. All the plots at different St approach this line just before contact, at lower h_o for larger St. Even within these approximate treatments, where p diverges as h_o in the limit $r \to 0$, the velocity of approach is significant at a roughness cut-off scale as small as 1 nm, for sufficiently large St. Thus the calculation indicates that contact occurs even when the spheres are atomically smooth. However, one needs to test these trajectories with experiments and try to observe how the difference of solid-on-solid contact comes into existence. The next chapter will attempt to answer this.
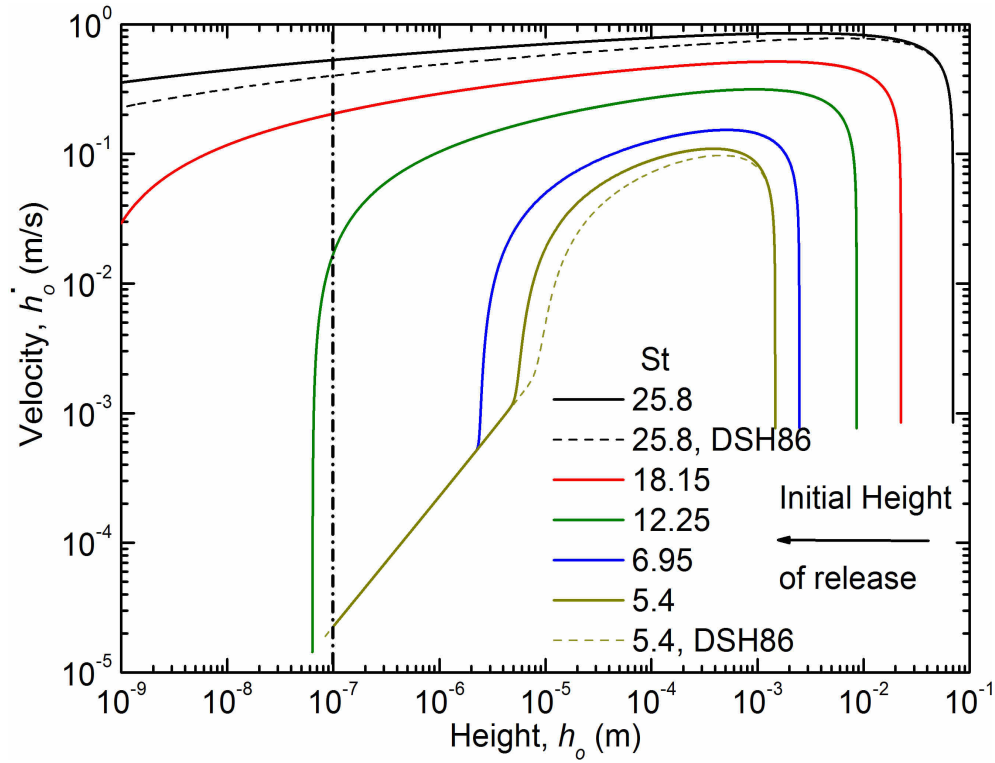
Fig. 3.8 Velocity ($\dot{h}_o$) versus height (h_o) of a rigid smooth sphere approaching a rigid plane calculated from the equation of motion 3.34. The results shown are for a steel sphere of diameter 15.4 mm (etched sphere dimension used in Chapter 2), dropped from different heights yielding the labeled nominal values of St. The solid curves are obtained by using equation 3.45 and equation 3.10 to get the net pressure force, and then numerically solving equation 3.34. The curves for various Stokes numbers cross a given height with different velocities; a typical example is shown by the vertical dash-dot line at $h_o = 100$ nm. At this height, the velocity for the curve labeled $St = 12.25$ is three orders of magnitude higher than those for the curves shown for lower St. This implies that even for extremely smooth surfaces, physical contact will occur prior to bouncing for a high enough Stokes number. The dashed curves at $St = 25.8$ and $St = 5.4$ are obtained by approximating the sphere as a paraboloid near $r = 0$, to compare with the previous calculations in DSH86: Davis et al. (1986) that use this approximation.

Chapter 4

High-speed imaging of dynamics

Our electrical experiments have shown that a sphere falling under gravity in a viscous medium will make physical contact with the bottom wall before bouncing, in contradiction to the predictions of lubrication theory and elastohydrodynamic theory, as discussed in Chapter 2 and Birwa et al. (2018). To understand this discrepancy, in this chapter, I describe studies in which we observe near-collision dynamics of the sphere, before and after the contact with the bottom plate, and observe the deviations from lubrication theory. It is difficult to track the sphere up to a few micrometers by using normal video techniques as the pixel resolution required for being able to observe the dynamics at these length scales is quite high. Also, since the velocity of the sphere is quite large at higher Stokes number (e.g. approximately 0.3 m/s at 10 μm for $St = 18.15$ as seen in Figure 3.8 of Chapter 3), one needs high frames per second to resolve such fast dynamics. Another important point in being able to track the collision dynamics is to have a good estimate of "zero" height. This height is defined as the height at which the contact is initiated and the gap between the undeformed sphere and the bottom plate is zero.

Earlier experiments done by Barnocky and Davis (1988), Gondret et al. (1999, 2002), and Joseph et al. (2001) used a high-speed camera to image the trajectory of the sphere before and after the collision but failed to resolve the contact dynamics. They had limited spatial and temporal resolution in determining when the contact was initiated, and therefore, do not have a good estimate of the "zero" height. Experiments by Lecoq et al. (1993) and Mongruel et al. (2010) tried to resolve the dynamics just before the collision for a settling sphere using interferometric techniques. They reported an error of around 112 nm in contact position and therefore, have a good estimate of "zero" height. However, their work only focused on the dynamics of a settling sphere. Hence, there still remains a need to understand the dynamics of a sphere, before and after the collision, in the bouncing regime.

Trigger Camera via Oscilloscope
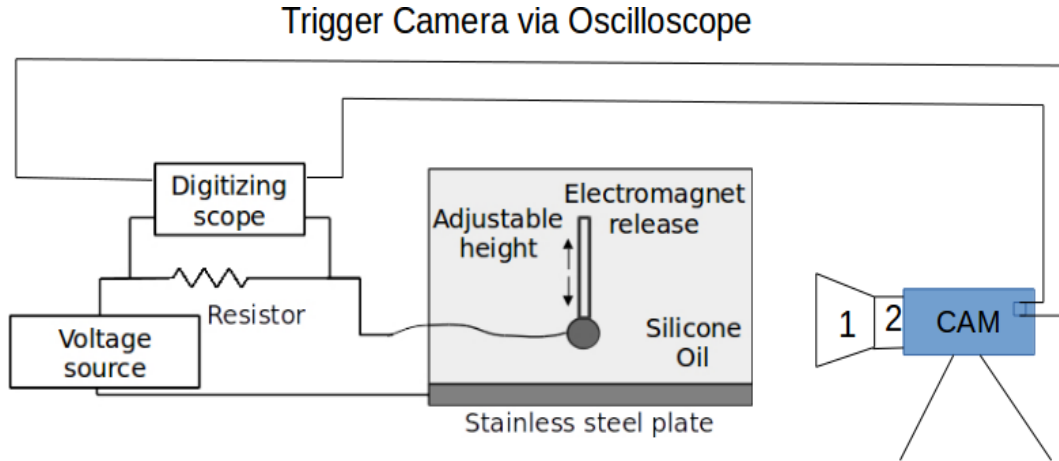
Fig. 4.1 Schematic diagram of the experimental set-up. A high-speed camera is triggered via an oscilloscope which detects a voltage change as soon as the sphere touches the bottom plate and the circuit gets completed. 1 is a macro lens and 2 is a bellow, both of which help us in zooming in on a 1 mm dot on $D = 16$ mm sphere.

4.1   Experimental set-up

To overcome the difficulties discussed above, we use our electrical set-up from Chapter 2 to trigger a high-speed camera. The electrical set-up allows us to resolve the contact point and we use a combination of a bellow and a macro lens to increase the spatial resolution. We drop stainless steel spheres of diameter $D = 16$ mm on a stainless steel plate of 10 cm x 10 cm cross-section and 1 cm thickness through silicone oil of dynamic viscosity $\mu = 0.335 \pm 0.02$ Pa-s, and density $\rho_f = 970$ kg/m³. As shown in Figure 4.1, a DC voltage is applied between the plate and the sphere. When the sphere makes electrical contact with the plate, the circuit is completed and the current is sampled by a digital oscilloscope (Tektronics DPO 4054B) across a $220k\Omega$ resistor at a rate of 5 MHz. As soon as the contact begins, a pulse is sent to the high-speed camera (Photron FASTCAM Mini AX 200 type 200K-M-32GB) from the oscilloscope which triggers the camera. The camera is already in an endless record mode at 50000 frames per second with a resolution of 384 x 256 pixels² and saves a fixed number of frames before and after the trigger event. This technique allows us to resolve contact within half a frame time, 10 μs, and gives a good estimate of "zero" height. The estimate of "zero" height in our experiment varies from 0.3 μm at the smallest Stokes number ($St = 6.5$) to less than 5 μm at the largest Stokes number ($St = 25$). The number of frames saved varies with St.

The roughness of the 16 mm sphere and the release mechanism of the sphere have previously been discussed in Chapter 2. To track the motions of the sphere, we stick a small piece of white paper, with a black dot of diameter $d = 1$ mm printed on it, on the sphere using scotch tape. The tape protects the paper and the dot on it from the oil. We track this dot, as the sphere approaches the bottom wall under gravity. To improve the magnification, we use a bellow between the high-speed camera and a macro-lens (Tamron SP AF 90 mm F/2.8). The bellow is a long tube, which helps in increasing the distance between the macro-lens and the camera sensor. The result is a magnification that makes each pixel equal to 6 μm. Thus, based on the resolution, our field of view is $2.29d$ x $3.05d$. We observe the sphere in reflection-mode lighting using a Philips LED flood-light (BVP 122 LED 110), which has an array of 64 LEDs working together to give 11000 lumens at 110 W.
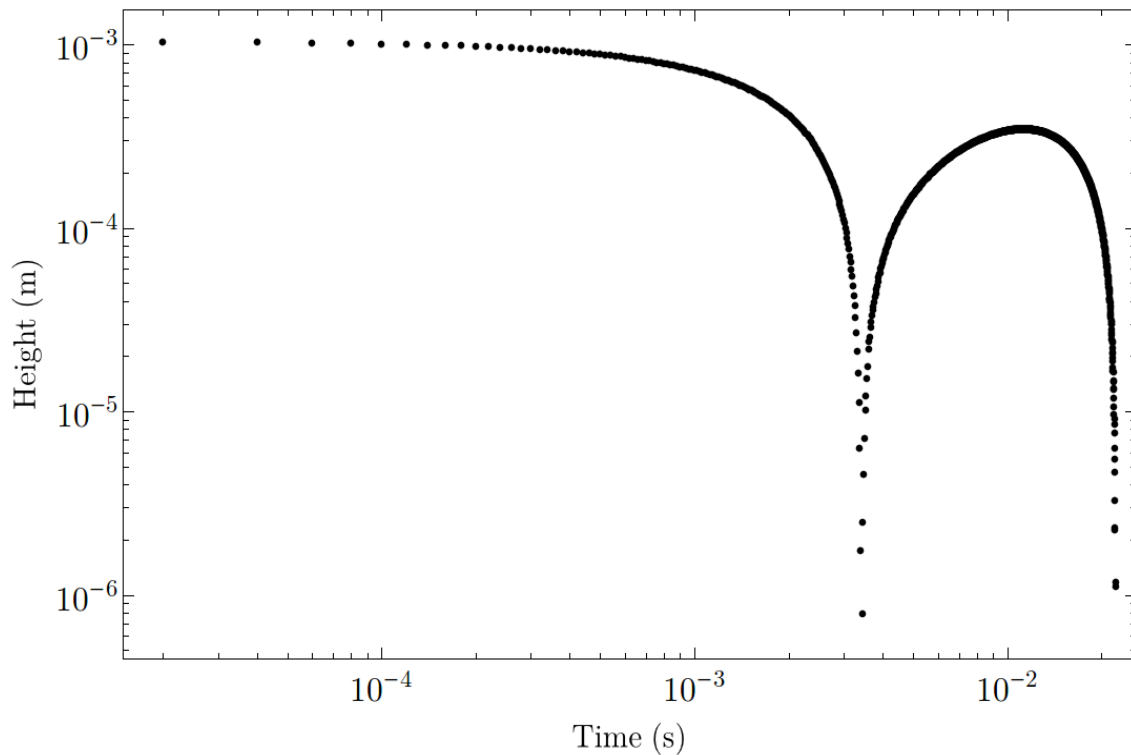
Fig. 4.2 A sample trajectory is shown as a log-log plot (height versus time) obtained for the Stokes number $St = 15$ by observing a dot of diameter 1 mm on the sphere at 50000 frames/sec. St is still defined using v_c as the velocity scale as discussed in previous chapters.

Different Stokes numbers are achieved by releasing the sphere from different heights using an electromagnet. We focus on the near-collision dynamics and therefore, our field of view lies very close to the bottom wall. Hence, we only use data from the time frame that marks the complete entry of the dot on the sphere into the field of view of the camera, regardless of the dropping height of the sphere.
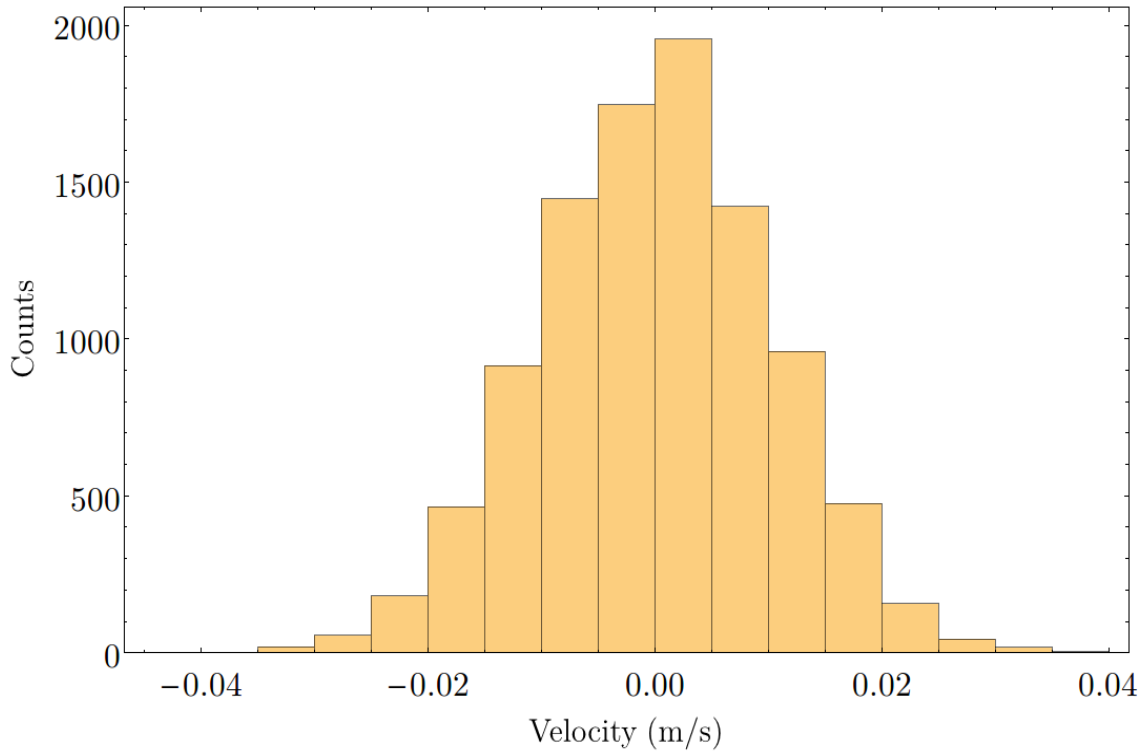
Fig. 4.3 Histogram of velocity when the sphere is at rest. The velocity when the sphere is at rest is obviously supposed to be zero but due to pixel noise, we observe a standard deviation of 0.01 m/s with zero mean velocity.

4.2   Image analysis

The resultant 8-bit frames are analyzed and the center of the 1 mm black dot on the white piece of paper stuck to the sphere is found out by using ImageJ software. This is done by converting the image into a binary scale by setting a cut-off threshold on the intensity. If a pixel intensity is larger than the cut-off value then the pixel is considered to be bright, otherwise dark. This method separates out the black dot clearly. After this, the "Analyze particle" feature of ImageJ software is used to find the center of the

dot. The dynamics of this center with time is studied to obtain the trajectory of the sphere. A sample trajectory is shown in Figure 4.2. As can be seen in the log-log plot, we are able to resolve up to a few micrometers above the bottom wall with the help of our arrangement consisting of a macro lens and bellow.

To obtain the velocity, we first convolve the height data with a Gaussian kernel by using "Gaussian filter" feature in Mathematica software. Then we use the quadratic interpolation with spline method in Mathematica to smoothen out the height data and convert it into a function. The advantage of the spline method is that it allows for the evaluation of continuous first-order derivatives. Finally, we obtain the velocity of the sphere by differentiating this function with respect to time. The velocity when the sphere is at rest should be zero and its distribution should ideally be a delta function. But due to the pixel noise, we get a velocity distribution which has a standard deviation of 0.01 m/s with zero mean velocity as shown in Figure 4.3. The error in the velocity measurement is considered to be equal to the standard deviation of this distribution. This sets a lower bar on the error (0.01 m/s) in velocity. The error in height due to pixel noise, measured by calculating the standard deviation of the sphere while it is resting on the plate's surface, is less than 0.06 pixels. This small error in the height and the velocity is the consequence of detecting the center of a 168 pixels (1 mm) diameter dot on the sphere. More the number of pixels in the dot, smaller is the error in the center detection.

A similar exercise was repeated by dropping the sphere from a large height ($St = 25$). In the beginning, the drag force is zero and hence the sphere's velocity increases rapidly. After some time when drag force comes into action, the sphere's acceleration decreases and finally it starts to decelerate because of the lubrication forces. In the vicinity of the maximum velocity, the sphere can be assumed to be moving with a constant velocity for a small time. We sample 50 frames in this constant velocity region and find that the standard deviation in the velocity is less than 0.01 m/s. We consider 0.01 m/s to be the final error in velocity measurement.

4.3   Trajectories and first-impact dynamics

Figure 4.4 shows the trajectory in a linear scale for $St = 15$. Figure 4.4 (a) and (b) show the height versus time and velocity versus time plots respectively (during the approach, the impact, and rebound stages of the dynamics). One can see the sphere decelerating before it comes in contact with the bottom wall. Figure 4.4 (c) and (d) are obtained by zooming into (a) and (b) panels at the point of contact. The blue vertical lines show the start and the end of the contact. The start of the contact is the point at which the
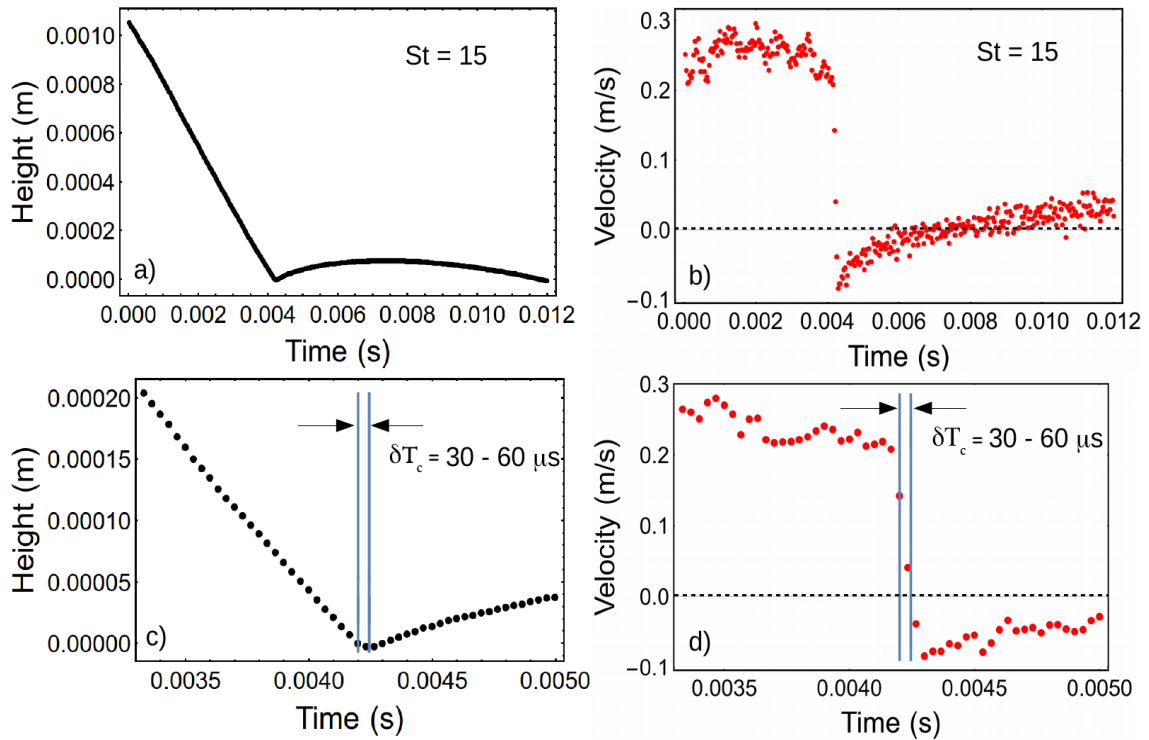
Fig. 4.4 A sample trajectory plot for $St = 15$. (a) and (b) shows the variation of height and velocity of the sphere with time, while it approaches the bottom wall, makes contact and then rebounds. (c) and (d) panels are obtained by zooming in close to the point of contact. The vertical blue lines, obtained by the data from the oscilloscope, show the start and end of the contact. Note that we get the contact duration and flight time from our electrical set-up.

oscilloscope triggers the camera and the duration of the contact is known by observing the data recorded by the oscilloscope as discussed in Chapter 2 (Figure 2.4). As shown in Figure 4.4 (d), it is clear that contact happens with a finite velocity, in contradiction to lubrication theory and elastohydrodynamic lubrication theory. During the contact, the sphere deforms and comes to rest before starting to bounce back. The precision in time here is approximately 10 μs (half a frame time) and this error in time does not change the velocity of impact considerably.

Using these trajectories, we obtain the variation of the vertical velocity with height for different Stokes number as shown in Figure 4.5 and Figure 4.6 (a) and (b). Figure 4.5 shows the results of five distinct runs taken at $St = 6.5$ and 20, to illustrate the level of reproducibility of the experimental trials. Different colors represent different trials at a fixed St.
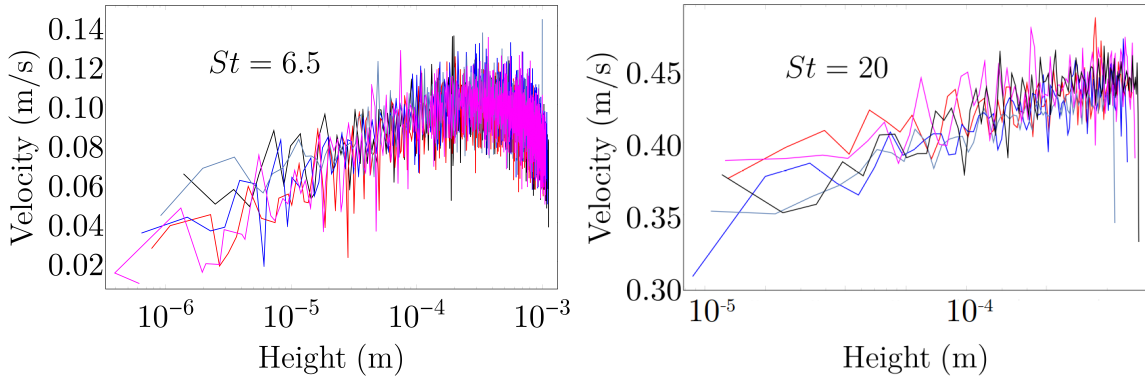
Fig. 4.5 Velocity versus height curves for experiments at $St = 6.5$ and 20. Different colors represent different experimental trials at the same Stokes number and show the reproducibility in the data. Using these curves, an average velocity versus height curve is obtained as shown in Figure 4.6.

We also observe a small amount of horizontal drift and rotation of the sphere and found that it was difficult to completely remove these unwanted features. The horizontal drift and rotation arise because of the asymmetry by which sphere leaves the electromagnet. To measure this drift and rotation we use three non-collinear dots on the sphere rather than one. We stick a small piece of white paper on the sphere with three black dots of 1 mm each on it using the scotch tape. The centers of the three dots make an isosceles triangle with the equal sides of length $\sqrt{2}$ mm and the unequal side being 2 mm in dimension. By observing the motion of these three dots while the sphere is falling, we were able to estimate the horizontal drift and the rotation of the sphere. It was difficult to measure the exact values of this drift and rotation and to separate out one from another due to the limitations in the spatial resolution. For instance, rotation of the dots around the vertical axis of the sphere was difficult to differentiate from the horizontal drift of the sphere. The maximum horizontal drift and angular velocity observed were less than 0.009 m/s and 0.0015 radians/s respectively at $St = 13$, while the maximum vertical velocity is around 0.25 m/s. The maximum horizontal drift and rotational velocity are approximately two orders of magnitude less than the maximum vertical velocity of the sphere. The drift and rotation remain variable in direction and magnitude from one trial to another. Based on the reproducibility of our data, we speculate that the horizontal and rotational movement of the sphere does not have any major effect in the estimation of the sphere dynamics.

As the reproducibility is good, we can obtain the average velocity as a function of height using data from different trials for each St as shown in Figure 4.6 (a) and (b).
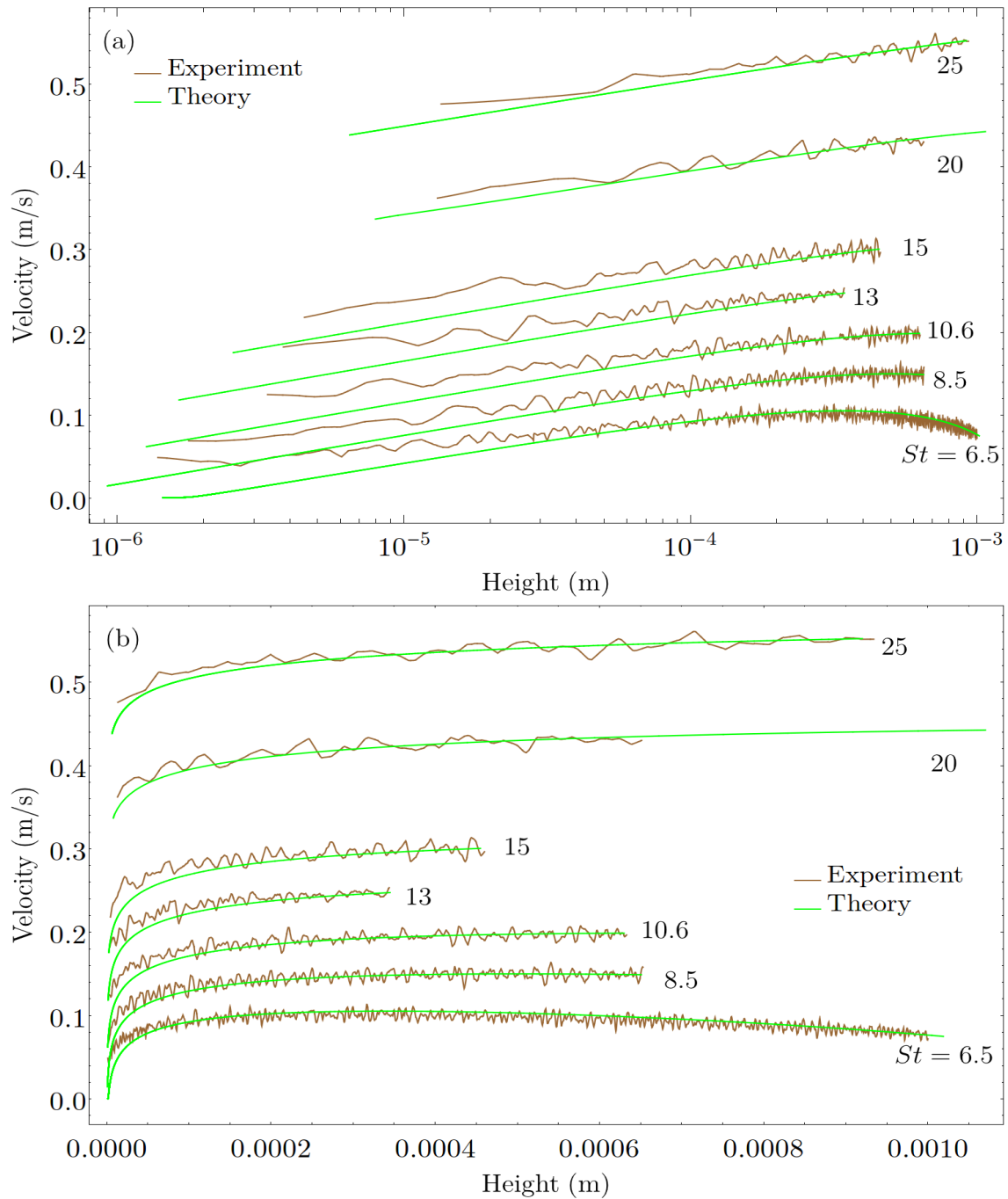
Fig. 4.6 Velocity vs height curves for experiments and theory at different St. Theoretical curves (shown in green) are obtained by using the first values of height and velocity captured by the camera as the initial condition. Experimental curves (shown in brown) are obtained by taking an average of five trial curves at each St. (a) Log-linear plots allow us to see the deviations in experiments from theory at small heights. (b) This difference is less evident in the linear-linear plot which shows a good match with the theory for most of the trajectory.

Note that the curves only start at around 1 mm height, which is because of the small field of view limited by the resolution of the camera at 50000 fps, as discussed earlier. To compare the experimental dynamics with lubrication theory, we obtain theoretical results by using the experimental data when the dot on the sphere first enters the field of view as the initial condition in equation 3.34, and calculate the pressure force by lubrication theory.

We see in Figure 4.6 (a) that the lubrication theory correctly describes the experimental curves for a sphere approaching a plate up to $\sim 50 - 100$ μm above the bottom wall. At smaller heights, we see a systematic deviation between the experimental curves and the theoretical results. The curves obtained from the lubrication theory lie below the experimental data at smaller heights and the gap between the curves increases as the sphere moves closer to the bottom wall. Hence, the sphere has a larger downward velocity at a given height compared to what is predicted by the theory. In the linear plot in Figure 4.6 (b), it is difficult to see these deviations as they are only prominent at smaller heights. Note that we are only comparing our results with the lubrication theory and not with the elastohydrodynamic theory. We expect elastohydrodynamic effects to produce a smaller velocity at a given height as the theory predicts that the bottom surface of the sphere will become flatter due to pressure build-up. The flattened surface will lead to greater dissipation. One can also note that as per elastohydrodynamic theory the sphere is supposed to reach zero velocity above the bottom surface, so the deceleration will be faster in elastohydrodynamic theory compared to lubrication theory. So by showing that our experiments observe larger downward velocity at a given height than predicted by lubrication theory, we are automatically ahead of elastohydrodynamic theory.

To quantify these differences between dynamics observed by experiments from that predicted by theory, we measured the relative deviations of experimental velocity V_{exp} with respect to the theoretically estimated velocity V_{th} by lubrication theory, $(V_{exp} - V_{th})/V_{th}$, and plotted it against the height as shown in Figure 4.7. We find that the deviations increase rapidly as the sphere approaches the bottom wall. This rapid increase in the relative deviations is expected to result in a contact in a finite amount of time with a finite velocity.

We track the sphere till one frame before the zeroth frame, the frame at which the contact is initiated and the sphere reaches the "zero" height. If the Stokes number is low, then the velocity of the sphere will be less at this "-1" frame compared to the corresponding velocity for larger St. Hence, we are able to track the sphere to much smaller heights at lower St. As discussed above, the deviations from lubrication theory become larger as the sphere reaches closer to the bottom plate. Consequently, we are able
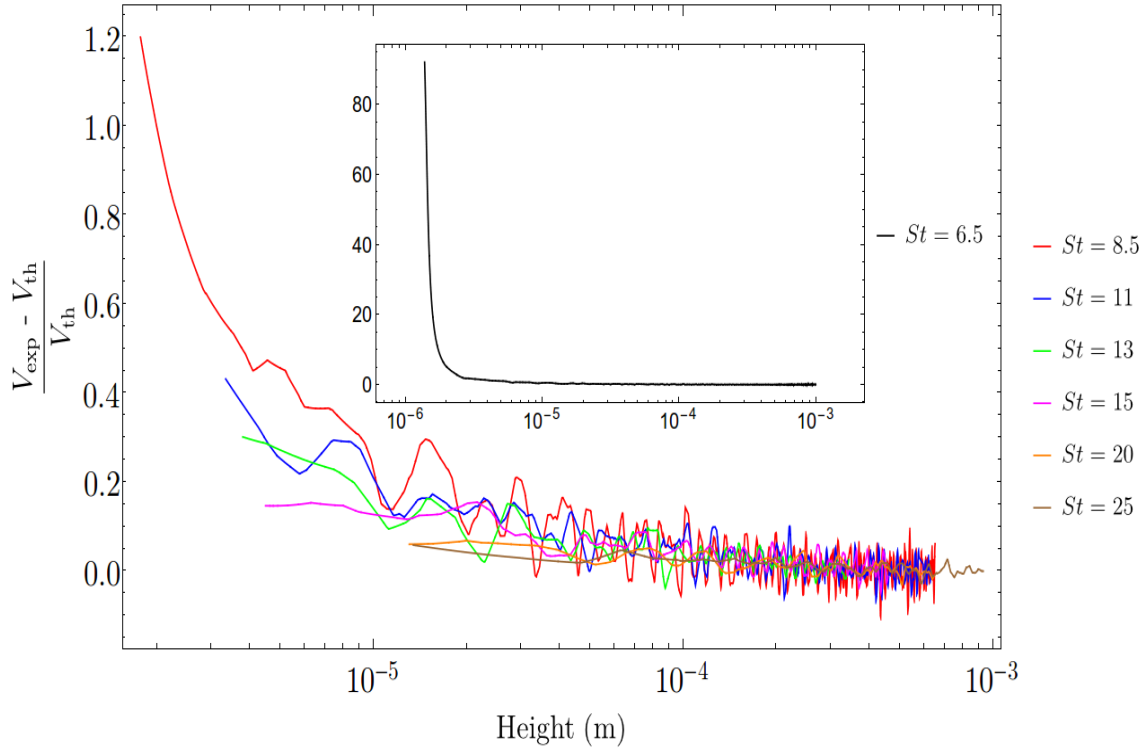
Fig. 4.7 Relative deviations of experimental velocity from that obtained by lubrication theory $(V_{exp} - V_{th})/V_{th}$ vs height. The deviations increase as height decreases. Different colors are for different St. In the inset, the deviations are shown for $St = 6.5$. The inset has the same units as the main figure.

to observe larger deviations for lower St as we can observe the sphere at smaller heights and also the theoretical velocity at these small heights are less for lower St. This becomes more comprehensible by looking at the inset of Figure 4.7. The inset corresponds to $St = 6.5$ and has the same x-axis and y-axis as the main figure. The deviation shoots up as the lubrication curve start approaching zero velocity (V_{th}) at small heights as can be seen in Figure 4.6 (a).

4.4 Rebound and second-impact dynamics

We also track the sphere during the rebound phase after the first impact as shown in Figure 4.8. It is comparatively easy to observe the rebound dynamics at larger St, as the bounce is more prominent in such cases. Negative velocity in the figure represents the upward motion of the sphere. For obtaining the rebound curves from lubrication theory we first measure the smallest rebound height from the experiment. Now, we feed
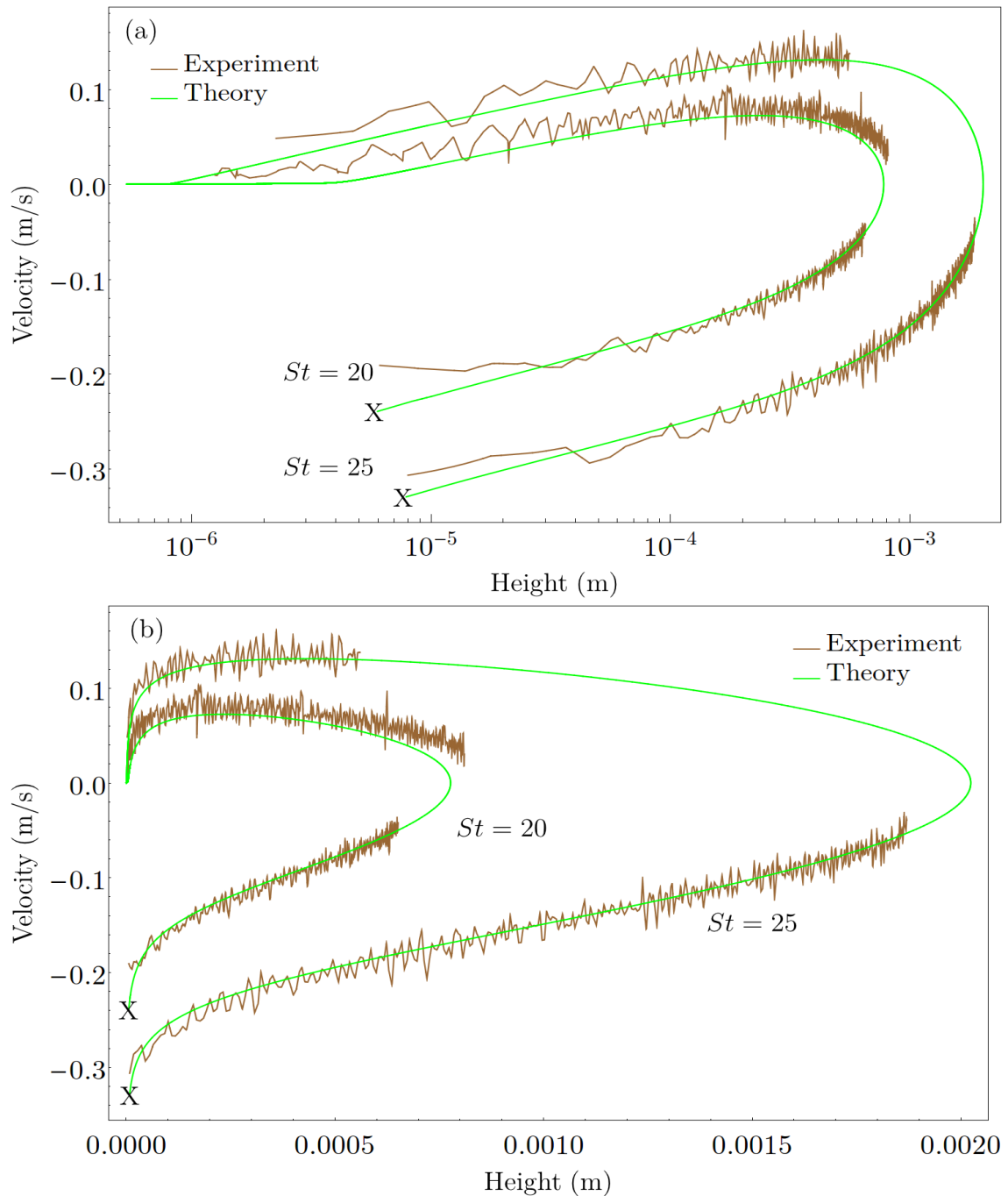
Fig. 4.8 Rebound curves for $St = 20$ and 25 plotted in (a) Log-linear scale and (b) linear-linear scale. The curves start from the fourth quadrant once the sphere loses the contact and starts to rebound. Negative velocity indicates upward motion of the sphere. Corresponding lubrication curves are plotted for both the Stokes number. Lubrication curves are obtained by using "X" as the initial condition in equation 3.34. A small region near the maximum height during the rebound is missing due to the sphere briefly leaving the field of view.

trial velocities in equation 3.34 and choose the one based on the condition that at large heights the lubrication curves matches well with the experimental data, similar to the first impact curves. We use this as the initial condition "X" as shown in Figure 4.8. Due to this choice of the initial condition, the theoretical rebound curves also show deviations at small heights similar to the first impact curves.
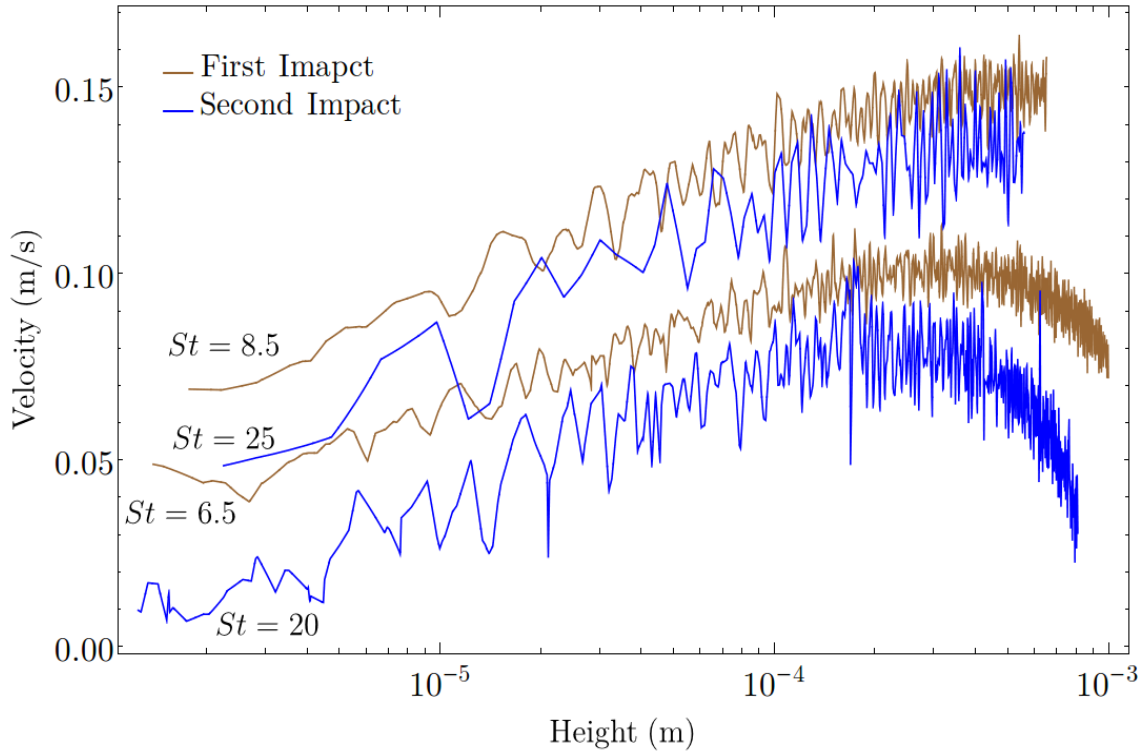
Fig. 4.9 Comparison of the second impact of $St = 20$ and 25 (calculated based on the first impact) with the first impacts of $St = 6.5$ and 8.5. After rebounding, sphere corresponding to $St = 20$ and 25 bounce to a height similar to the height from which the sphere is dropped to achieve lower Stokes number. The St during the second impact of $St = 20$ is less than 6.5 and $St = 25$ is between 6.5 and 8.5.

The sphere bounces up to reach the maximum height where its velocity becomes zero and then starts to fall towards the bottom wall for another impact. We refer to this next impact as the "second impact". As the sphere reaches the maximum height above the bottom wall during rebound, it leaves our camera's field of view. Therefore, there is some data missing near that region in Figure 4.8 (a) and (b). The second impact dynamics for these values of St (20 and 25) are similar to the dynamics of the first impact for smaller St as shown in Figure 4.9.

The second impact dynamics of a sphere whose first impact was at $St = 20$, corresponds to a Stokes number less than $St = 6.5$. Therefore, it is appropriate to compare this second impact dynamics to the first impact dynamics of a sphere corresponding to $St = 6.5$. Similarly, the second impact of $St = 25$ corresponds to the dynamics of a case where St (based on the first impact) lies between 6.5 and 8.5. These observations that rebound after the first impact and second impact dynamics have the same qualitative behavior as the first impact dynamics (and lubrication theory) of a suitably lower Stokes number suggest that the disturbances created due to first impact (or rebound after the first impact) might not be important in such systems and die quite rapidly.

This can also be proven by directly comparing the disturbance time scale, the time taken for the disturbances to die, with the rebound time scale at $St = 20$ and $St = 25$. The rebound time scale is taken as half of the flight time. As discussed in Chapter 2, the flight time is the time duration between the two contacts. We find that the rebound time scale is approximately 0.015 s and 0.024 s for $St = 20$ and $St = 25$ respectively. The disturbance time scale is estimated by using L^2/ν, where L is the rebound height — the maximum height to which the sphere jumps after rebounding and ν is the kinematic viscosity of the silicone oil. From this, we obtain the disturbance time scale of ~ 0.0019 s and 0.012 s for $St = 20$ and $St = 25$ respectively. Comparing the two time scales, we find that the disturbance time scale is smaller compared to the rebound time scale. However, this difference seems to be decreasing with the decrease in St and we expect the disturbances to play a significant role in the small rebounds of lower St like $St = 16$ and $St = 13$.

4.5   Coefficient of restitution

We are able to measure the approach and rebound velocity at heights closer to the bottom wall than earlier studies by Barnocky and Davis (1988), Gondret et al. (1999, 2002), and Joseph et al. (2001). Therefore, we get a better estimate of the coefficient of restitution η (the ratio of rebound velocity to the approach velocity) as shown in Figure 4.10. We measure the approach velocity and the rebound velocity at three different heights ($h_o = 13.5$, 20, and 30 μm) and for four different St. We find that the coefficient of restitution η at any St increases with decrease in the height h_o at which it is measured. This is more evident at lower St.

The coefficient of restitution is used as a measure of dissipation and inelasticity in dry collisions. Reducing the height reduces the contribution from fluid dissipation and η reaches closer to the dry coefficient of restitution limit. Therefore, it makes sense that
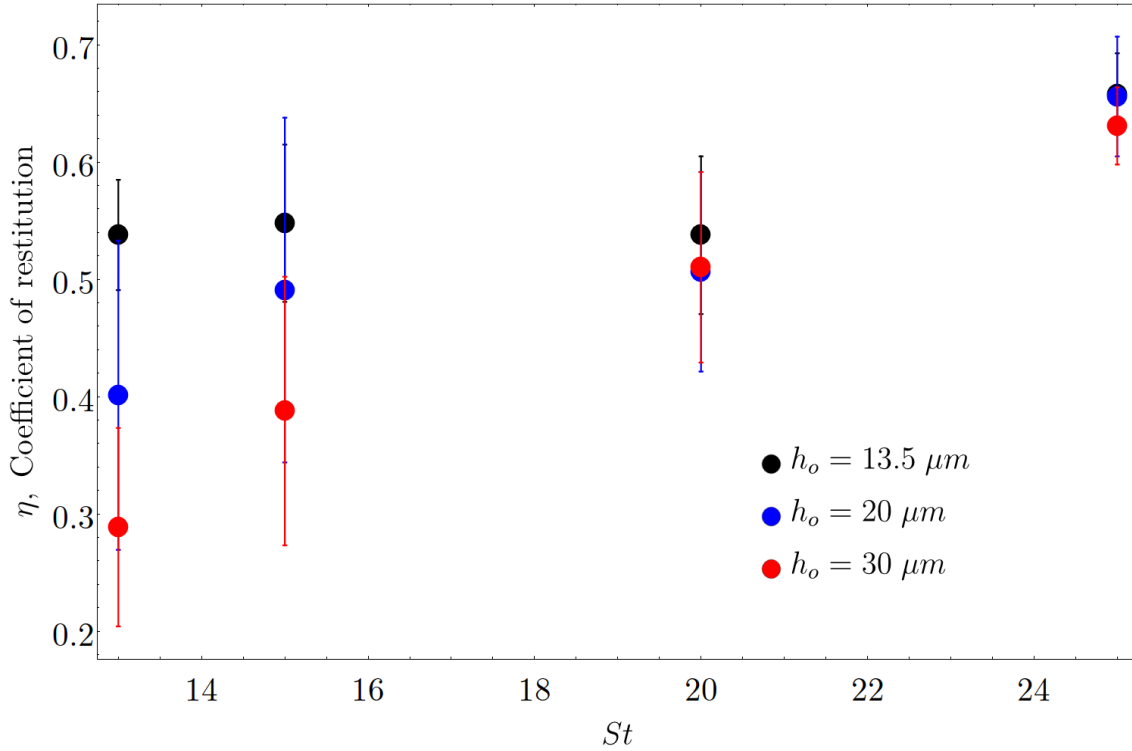
Fig. 4.10 Coefficient of restitution η vs St measured at three different heights h_o, above the bottom wall. η increases with St as observed in earlier studies by Barnocky and Davis (1988), Gondret et al. (1999, 2002) and Joseph et al. (2001). Also at small St, η increases with the decrease in height at which it is measured.

η increases with a decrease in the height at which it is measured. The difference in coefficient of restitution at different heights becomes less pronounced for larger St as the incoming and outgoing velocity remains almost the same at all the three heights.

From Figure 4.10, we can also see that the coefficient of restitution increases with St. This result is similar to earlier studies by Barnocky and Davis (1988), Gondret et al. (1999, 2002), and Joseph et al. (2001), who found that beyond St_c, coefficient of restitution increases with increasing the Stokes number. We expect a non-monotonic behavior of η as the St decreases (or the velocity of impact decreases) as observed by King et al. (2011), which can be the reason for St_c to be around 6 to 7 as reported in Chapter 2. So, direct extrapolation of η versus St plot is not advisable as it might give an erroneous value of St_c.

4.6   Summary and conclusion

This chapter brings us to the end of the study of normal collisions in a viscous medium. To summarise the results from Chapter 1-4, we found that there is indeed a critical Stokes number (around 7), marking the transition from the settling regime to the bouncing regime in immersed collisions. This is in agreement with previous observations and with elastohydrodynamic theory. In contradiction with lubrication theory, we observed direct mechanical contact for 10-100 microseconds before bouncing. The duration of this contact was found to be independent of the electrical parameters and weakly dependent on impact velocity, which is consistent with Hertzian elastic theory. We concluded that the total dissipation in the sphere-wall encounter is not strongly affected by the duration of solid-on-solid contact at large Stokes number. This indicated that despite solid contact, most of the loss of kinetic energy in this process is due to fluid dissipation.

We re-analysed the problem analytically by including unsteady terms and inertial terms, which were considered negligible in lubrication theory. We derived a boundary layer equation to describe the flow and solved it by a novel method. This allowed us to obtain the radial velocity profile below the sphere from which we can calculate the hydrodynamic drag on the sphere. We found that the actual approach velocity is slightly faster than predicted by lubrication theory at smaller heights by coupling a high speed-camera with our earlier electrical set-up. Rebound and second impact dynamics behavior were found to be similar to lubrication theory predictions.

4.7   Future work

There still remain a few unresolved issues in this work which needs to be addressed. As discussed in Chapter 3, even an atomically smooth sphere is expected to make contact with an equally smooth plate. Still, it will be intriguing to see if the duration of the contact changes for a very smooth sphere and plate. One can use Mica surfaces of few nanometer roughness (or less) for this purpose along with our electrical set-up.

The high-speed measurements in this chapter suggest that differences between the theory and the experiments grow as the sphere approaches the bottom plate (see Figure 4.7). These deviations can explain the contradiction from lubrication theory. It will be interesting to monitor these deviations at heights smaller than 1 μm and study the deviations for surfaces of different roughness. Optical techniques like Newton ring or evanescent-wave coupling along with a Borosilicate sphere can be used for this purpose. Evanescent-wave coupling experiment might also give some insights into the

time-evolution of the deformation of the sphere. Does the sphere always approximate a disk in the contact region as Hertzian theory predicts? Or is there a small dimple at the center of the contact region at the beginning of the contact? In addition, it would be interesting to study how this deformation changes with the elasticity of the material and how this changes the duration of contact.

The present study focuses only on normal collisions. Similar questions can be asked for an oblique collision. Our electrical set-up can be used again for that purpose with the bottom plate mounted at some finite angle with the horizontal and the variation of the contact duration with the inclination angle of the plate can be studied. Also, it will be interesting to study the change in dynamics if the sphere is rotating with large angular velocity and compare it with the results of this chapter and the lubrication theory for a rotating sphere.

It will be exciting to compare our results in this chapter with direct numerical simulations. For this purpose, we are currently collaborating with Laurent Lacaze of Institut de Mécanique des Fluides de Toulouse, France. He is studying the dynamics of the sphere using the Immersed Boundary Method. Preliminary results look promising and show a good match. A rather difficult but intriguing experiment will be to observe velocity profiles in the gap between the sphere and the plate. Particle Image Velocimetry (PIV) with nanoparticles can be used for this purpose. It will be interesting to see how closely the experimental radial velocity profile resembles a parabola as predicted by lubrication theory. One can expect the profile to change as the gap decreases owing to the roughness and the deformation of the surfaces.

Chapter 5

Stress in a granular column

This work is done in collaboration with Professor Bulbul Chakraborty from Brandeis University. In this chapter, we study the structures formed when many spheres are allowed to settle under gravity and come to rest. We shall see later in this chapter that heaving, namely, a collective bouncing back of particles after contact with the bed below them, can reorganize particles in surprising ways. The granular structures are governed by inter-particle frictional forces. This chapter focuses on understanding the stresses and packing inside such 2D monodisperse structures. The numerical methodology used in this study is discussed first and then the attention is shifted to different protocols used to prepare the granular columns. We show that preparing the 2D static granular column in different ways can generate completely different local stress profiles. Comparisons have been made with Janssen's model and other previous studies (Landry et al., 2004; Vanel and Clément, 1999). In the end, a model has been presented that attempts to explain the observed surprising behavior of vertical stress. The work discussed here is still in progress.

5.1 Numerical simulations

Molecular dynamics numerical simulations are carried out using the granular package of LAMMPS software (https://lammps.sandia.gov/) (Plimpton, 1995). The general idea of creating the computational domain and interaction potential is the same as in Merrigan et al. (2018). As we mentioned in the article, the computational domain is a quasi-2D rectangular box as shown in Figure 5.1 (a) filled with monodisperse particles. All lengths and masses are measured in units of the diameter d and mass M of the particle respectively. As a consequence, the diameter and mass of the particle are 1 and 1 respectively. Acceleration has been non-dimensionalized by the acceleration due to

gravity g and hence $g = 1$ in the simulation. We express all times in units of $T = \sqrt{d/g}$, which is the time taken for a grain to fall through a distance of one radius $0.5d$ under gravity, and each time step in the simulation is 0.0001 in these units. The velocities, forces, stresses and damping constants in the simulations have been non-dimensionalized by d/T, Mg, Mg/d^2, and $1/T\, d$ respectively. The simulation geometry is effectively two-dimensional since after each time step the force and velocity on each grain in the third dimension is set to zero. In line with standard usage, the simulations are termed as quasi-2D.
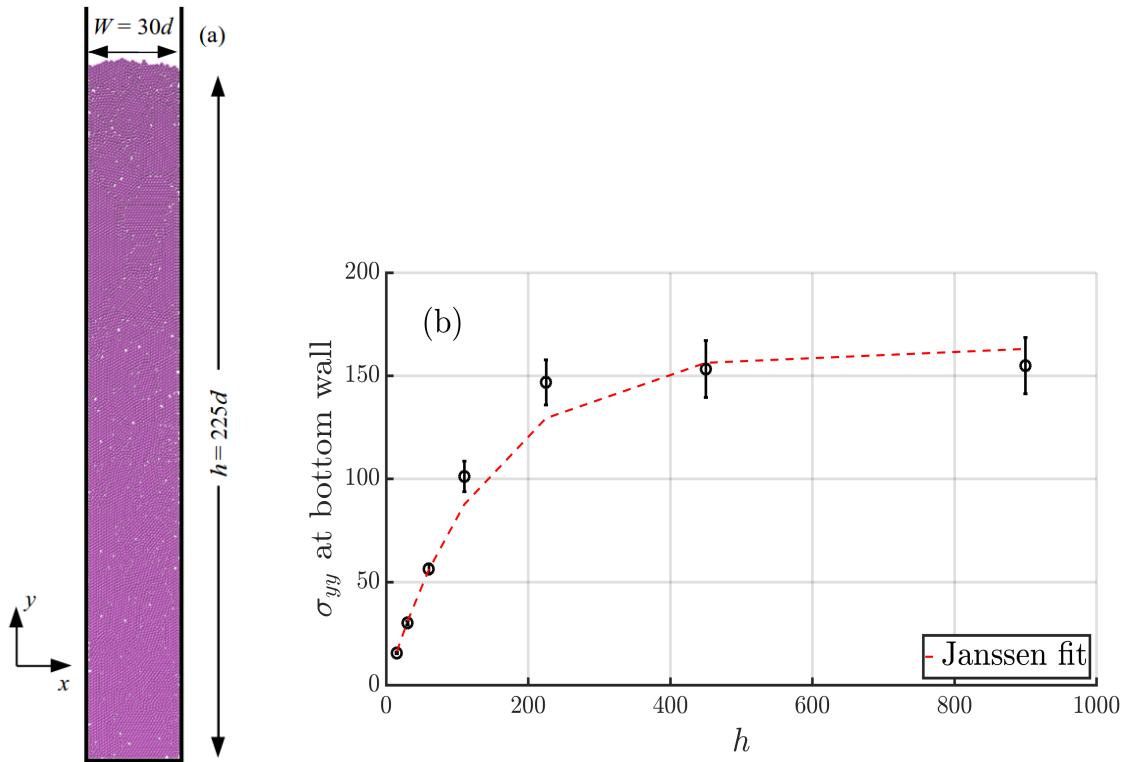
Fig. 5.1 (a) A sample geometry used in our quasi-2D computational study. The domain here has width $W = 30$, height $h = 225$, and is filled with ~ 7500 mono-disperse soft spherical grains. Gravity is pointing downwards. Our analysis in this chapter has primarily been done on widths $W = 30, 60$ and 90 and heights $h = 225, 450$ and 900. (b) Vertical stress, σ_{yy}, on the bottom wall, created by the S2 method, as a function of fill-heights for $W = 30$ and $\mu_w = 0.5$. Error bars are the standard deviation obtained by running 20 different ensembles at each height. The red dashed line is the best fit obtained by the Janssen's model which gives decay length $s = W/2\mu_w K = 148.1$. The Janssen form is taken from equation 5.11 and ϕ is chosen to be 0.87. This gives $K = 0.203$ and saturating value $4s\phi/\pi$ from equation 5.11 to be 164.

The side walls are created using the 'wall/gran' package in LAMMPS. The grain-grain and grain-wall forces are modeled by a Hertzian contact law coupled with a velocity-dependent damping term. Under this law, the force between two overlapping spheres of radii R_i and R_j and masses M_i and M_j is a function of their overlap $\delta = R_i + R_j - r$, with r being the center to center distance between the two adjacent grains. For the positive values of overlaps, the components of force are given by:

$$\mathbf{F_{n_{ij}}} = \sqrt{\delta}\sqrt{\frac{R_i R_j}{R_i + R_j}}[k_n \delta \mathbf{n_{ij}} - m_{\text{eff}}\gamma_n \mathbf{v_{n_{ij}}}]; \tag{5.1}$$

$$\mathbf{F_{t_{ij}}} = \sqrt{\delta}\sqrt{\frac{R_i R_j}{R_i + R_j}}[-k_t \mathbf{u_{ij}} - m_{\text{eff}}\gamma_t \mathbf{v_{t_{ij}}}], \tag{5.2}$$

where $\mathbf{F_{n_{ij}}}$ and $\mathbf{F_{t_{ij}}}$ are the normal and tangential force components respectively between the two grains with corresponding elastic constants set to be $k_n = 2 \times 10^5$ and $k_t = 2k_n/7$ (Silbert et al., 2001). The first term in the normal force is along $\mathbf{n_{ij}}$, the unit vector along the line connecting the centers of the contacting spheres. The tangential displacement vector is represented by $\mathbf{u_{ij}}$. The tangential force is truncated to satisfy the Coulomb yield criterion ($\mathbf{F_{t_{ij}}} \leq \mu_w \mathbf{F_{n_{ij}}}$), where μ_w is the static coefficient of friction and is chosen to be $\mu_w = 0.5$ for both grain-grain interactions and grain-wall interactions. The reduced mass is represented by $m_{\text{eff}} = (M_i M_j)/(M_i + M_j)$ and $\mathbf{v_{n_{ij}}}$ and $\mathbf{v_{t_{ij}}}$ are the normal and tangential components of the relative velocity between the two grains in contact. The viscoelastic damping constant for normal contacts in our study is fixed at $\gamma_n = 500$. However, we set $\gamma_t = 0$ for tangential contacts.

5.2 Methodology

The granular column is primarily prepared by three different protocols: S1 (Settling), S2 (Viscosity), and V1 (Vibration). S1: At the start of the simulation, N grains with zero initial velocity are placed randomly between the vertical coordinate 1 and initial maximum height H_{int} within the column, with all lengths in units of d. The number of grains N and H_{int} used for creating a granular column of fill-height $h = 225$ and width $W = 30$ are 60000 and 800 respectively. These parameters (N and H_{int}) change if a different-size granular column is being created. Once placed in the container, many grains are found to be overlapping with each other, i.e., their center to center distance is less than the diameter of each grain. The overlapping grains are removed and n grains remain in the container. These remaining, non-overlapping grains are then allowed to settle under gravity and the desired fill-height is obtained. The fill-height after settling

$n = 7400 - 7600$ particles is ~ 225. The grains are allowed to settle until the total kinetic energy of the system is less than 10^{-12}. This method of creating a granular column will be called the "Settling protocol" and hereafter is referred to as the S1 protocol.

In the S2 protocol, once all the overlaps have been eliminated during initialization, the grains are allowed to fall under gravity like in the S1 protocol. But in this case, after all the grains have fallen, a viscous damping force that is proportional to the velocity of the grains in the domain is introduced to drain the kinetic energy. This force can be thought of as a Stokes drag on spherical particle arising because of a viscous medium. This simple energy-minimization technique is commonly used to freeze the granular system (Landry et al., 2003, 2004). The drag force is removed after the total kinetic energy of the system is less than 10^{-12} and particles are allowed to relax normally for 100 units of time. This method of creating a granular column will be called the "Viscous protocol" and hereafter is referred to as the S2 protocol.

In the V1 protocol, this frozen S2 system is vibrated along x-axis [see Figure 5.1 (a)] for 100 units of time and then the final system is allowed to relax till the total kinetic energy is less than 10^{-12}. The vibration is sinusoidal with an amplitude of 0.1 with a period of 0.1 units of time. This method of obtaining the granular column will be called the "Vibration protocol" and hereafter is referred to as the V1 protocol.

Once we have obtained the final granular column, the stress tensor on the ith particle is calculated by summing over the contact stresses at all the contacts of this particle. Then, the granular column is divided into horizontal strips of size 15 x W, where W is the width of the granular column and 15 is the height of the strip. To obtain the stress $\sigma_{\alpha\beta}$ in volume V, which corresponds to a horizontal strip in the granular column, the stresses of all the particles are summed over, and expressed per unit volume as (Silbert et al., 2001):

$$\sigma_{\alpha\beta} = \frac{1}{V}\Sigma_i\left[\Sigma_{j\neq i}\frac{\mathbf{r_{ij}}^\alpha \mathbf{F_{ij}}^\beta}{2}\right], \tag{5.3}$$

where $\mathbf{F_{ij}}$ is the contact force between the ith and the jth particle. The stress tensors in the vertical strips of size 5 x h are obtained using the same method, where h is the fill-height of the column and 5 is the width of the vertical strip. This helps us to understand how the stress components are varying across the horizontal direction in the granular column.

The vertical variation of stress for different sizes of the granular column (widths = 30, 60, and 90 and fill-heights = 225, 450, and 900) and created by different protocols (S1, S2, and V1) are discussed in next section. Wall friction is always kept equal to inter-particle values.

5.3   Variation of vertical stress

In this section, we discuss the variation of the vertical stress in different protocols. We start by checking the stress at the bottom of the S2 protocol and comparing it with Janssen's model in section 5.3.1. Thereafter, we shift our attention to the variation of the vertical stress inside the column for different fill-heights and widths in the S2 protocol. Here, we encounter a peculiar looking stress profile, completely different from Janssen's prediction. This is the main result of this chapter. We also test for isotropy by observing the variation in horizontal stress. We did not start with the S1 protocol, as it is just a primitive version of the S2 protocol, and we observe in section 5.3.3 that the behavior of vertical stress in both the protocols are similar. The S2 protocol is primarily used as it is computationally least expensive to generate the packing and hence more data is available for it.

In section 5.3.2, we ask the question of what happens if we vibrate the granular column created by the S2 protocol? Can we change the vertical stress profile? If yes, is the new vertical stress profile closer to the Janssen's prediction? Then, in section 5.3.3, we compare all the protocols discussed till now including the S1 protocol and also introduce a new protocol called the Mobilize (M1) protocol. In this protocol, the particles in contact with the side walls are mobilized by the moving the bottom wall slowly downwards and then letting the packing relax. We observe that this protocol is closest to the Janssen form.

To compare our results with the earlier study of Landry et al. (2004), we introduce yet another protocol (Pouring protocol) in section 5.3.4. In this protocol, we pour the particles from a fixed height above the column and use the same parameter values as Landry et al. (2004). Finally, in section 5.3.5, we compare vertical stress profiles in monodisperse packings with bidisperse packing. Here, we attempt to understand if the peculiar behavior observed in the S2 protocol disappears for a bidisperse disordered packing. We mostly concentrate on the vertical stress profiles in different protocols in this section and revisit the topics like isotropy and wall friction in section 5.4. Note that the mention of any particular protocol refers to a numerical experiment where the column is formed using the concerned protocol.

5.3.1   The S2 protocol

Figure 5.1 (b) shows the comparison of the vertical stress at the bottom of the granular column with Janssen's model for different fill-heights. The comparison is done for a column of width $= 30$ and $\mu_w = 0.5$, obtained by the S2 protocol. To obtain the vertical

Fig. 5.2 (a) Vertical stress as a function of the vertical coordinate in a granular column for $W = 30$, $\mu_w = 0.5$, and three different fill-heights of the granular column, created by the S2 method. The vertical coordinate is measured from the bottom surface and therefore $h - y = 0$ represents the top of the granular column. There is a linear hydrostatic-like region near the free surface as observed by Landry et al. (2003, 2004) and Vanel and Clément (1999). Interestingly, we observe a sudden change in slope after this hydrostatic-like region and find a maximum which becomes sharper for higher fill-heights. (b) Vertical stress as a function of $h - y$ for $h = 225$, $\mu_w = 0.5$, and three different widths of the granular column, created by the S2 method, shows us that the maximum observed in (a) vanishes at larger widths of the column. Error bars are the standard deviation obtained by running 20 different ensembles at each height.

stress at the bottom wall, we determine the total force applied on the bottom wall by the particles which are in contact with it and then divide this force by the width of the container. This method is only used to determine the stresses on the walls. The stresses inside the container are obtained by using equation 5.3. As can be seen, the vertical stress at the bottom of the container is consistent with Janssen's prediction of stress saturation beyond a certain fill-height. The Janssen's model was discussed in Chapter 1 and will be also be revisited in section 5.4. The Janssen form of equation 5.11 is used for fitting by fixing $y = 0$ and choosing area-based packing fraction ϕ to be 0.87 in the equation. The fit gives a decay length $s = W/2\mu_w K$ of 148.1. This, in turn, gives $K = 0.203$ and the saturating value $4s\phi/\pi$ is found to be 164 from equation 5.11. K is the ratio between the horizontal normal stress to the vertical stress and is used as the fitting parameter. It is also referred to as Janssen's constant. To test if Janssen's model adequately describes local stress of the granular column, we obtain the variation of vertical stress with the vertical coordinate inside the S2 granular column of different fill-heights at $W = 30$.

This brings us to the most interesting result of this chapter. Figure 5.2 shows the variation in σ_{yy} with vertical coordinate in a column created by the S2 protocol. The different curves are for different fill-heights of the granular column and the zero on the x-axis represents the free surface of the packing. The trend depicted in Figure 5.2 (a) is quite peculiar. All three curves show an almost linear increase in vertical stress close to the free surface of the packing. This hydrostatic-like region near the free surface has been observed previously in simulations (Landry et al., 2004). While Janssen's model has been extensively tested by examining stress at the bottom of a column, we have not come across any earlier studies which asks whether this model is valid locally inside a 2D column, to the best of our knowledge. For example, Landry et al. (2004) only measured global vertical stress (total vertical stress) for different fill heights by raining particles from a fixed height above the granular column at a fixed rate.

After the linear increase, the slope of the vertical stress changes in Figure 5.2 (a) and a maximum in the vertical stress is observed. The figure does not show saturation as predicted by Janssen's model. Beyond the maximum, the stress decreases with height. In other words, the particles below bear less weight than those above. This decrease in pressure at greater depths is counter-intuitive and will be explained in more detail in section 5.4. The maxima in σ_{yy} for $h = 900, 450$, and 225 curves obtained by the S2 protocol are different and occur at different heights. Despite this, the final σ_{yy} at the bottom is remarkably the same, as can be seen by the dotted line in Figure 5.2 (a), and as discussed earlier [see Figure 5.1 (b)].
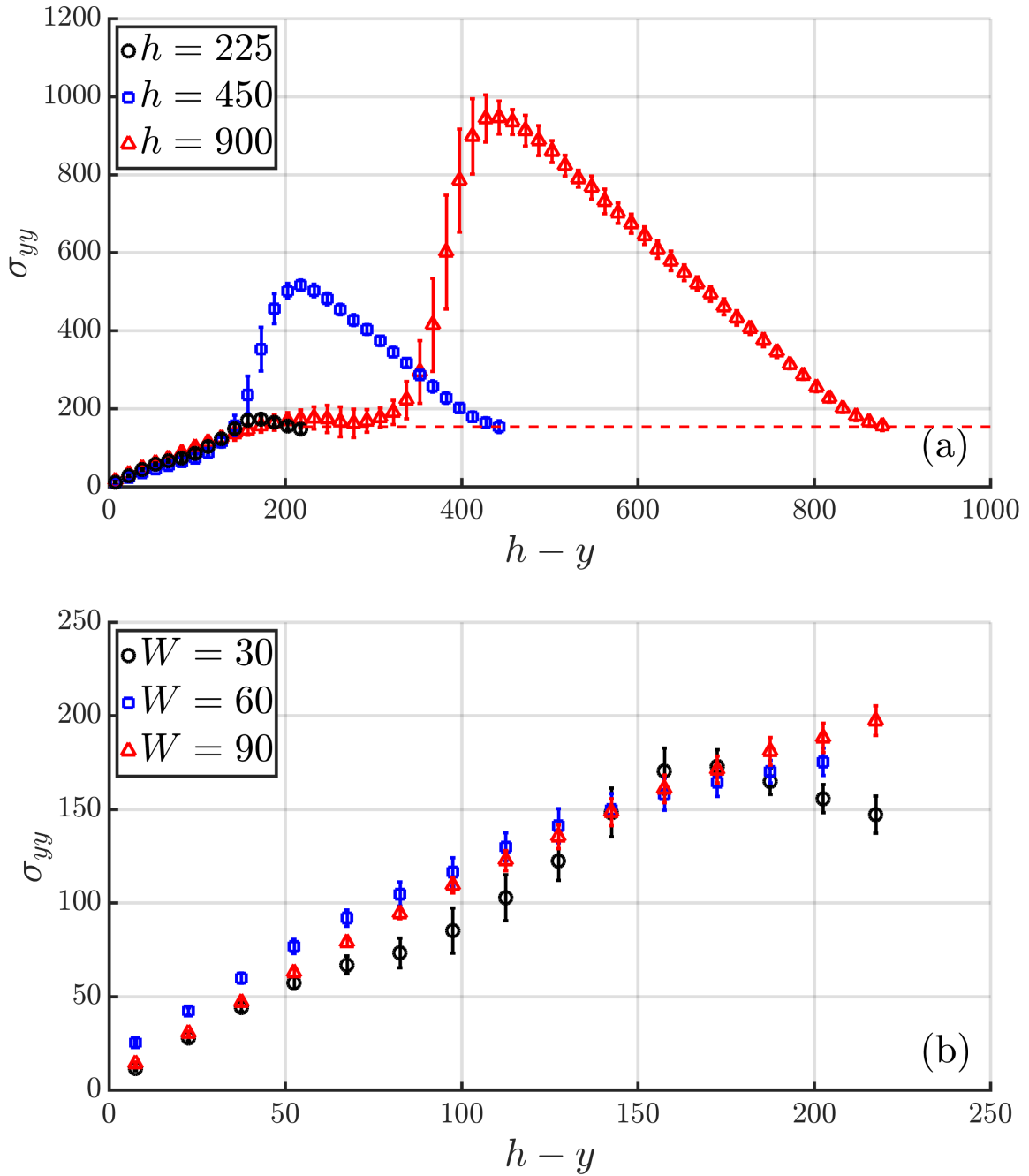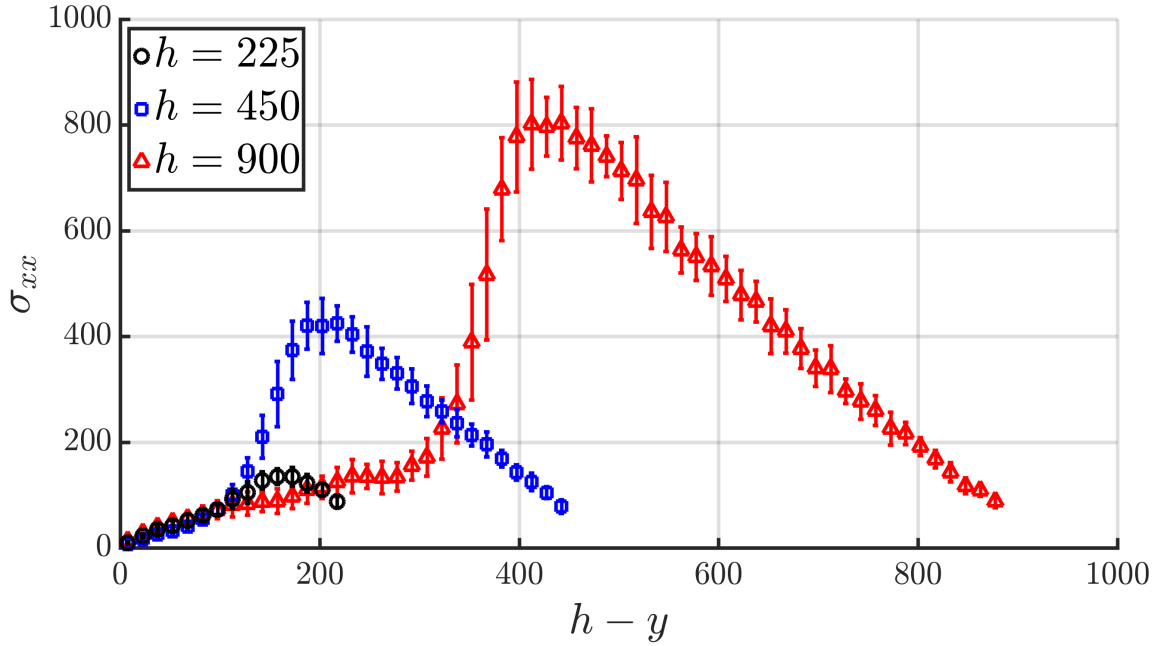
Fig. 5.3 Horizontal stress as a function of the vertical coordinate in a granular column for $W = 30$, $\mu_w = 0.5$, and three different fill-heights of the granular column, created by the S2 method. Error bars are the standard deviation obtained by running 20 different ensembles at each height.

The general understanding suggests that there are many force chains inside a granular column (Majmudar and Behringer, 2005). Increasing the width of the granular column should make it difficult for force chains to span the column width and thus transfer the load on to the side walls. So, it is expected that the maximum in σ_{yy} at larger fill-heights might start disappearing if the width of the column is increased. Figure 5.2 (b) shows the vertical variation of σ_{yy} in the column for different widths at fill-height $h = 225$. There is a maximum for width $W = 30$ case as already seen in Figure 5.2 (a). The maximum disappears once the width is increased to $W = 60$ and $W = 90$ and the vertical stress is maximum only at the bottom of the column.

A crucial assumption in Janssen's model is that the stress is isotropic inside the granular column. To test this, we plot the horizontal component of stress with the vertical coordinate for different fill-heights as shown in Figure 5.3. The behavior of σ_{xx} seems very much similar to the trend depicted by σ_{yy}. This shows us that even with such a peculiar behavior of vertical stress, horizontal stress is almost proportional to the vertical stress and $\sigma_{yy} \propto \sigma_{xx}$ is a good assumption to follow.
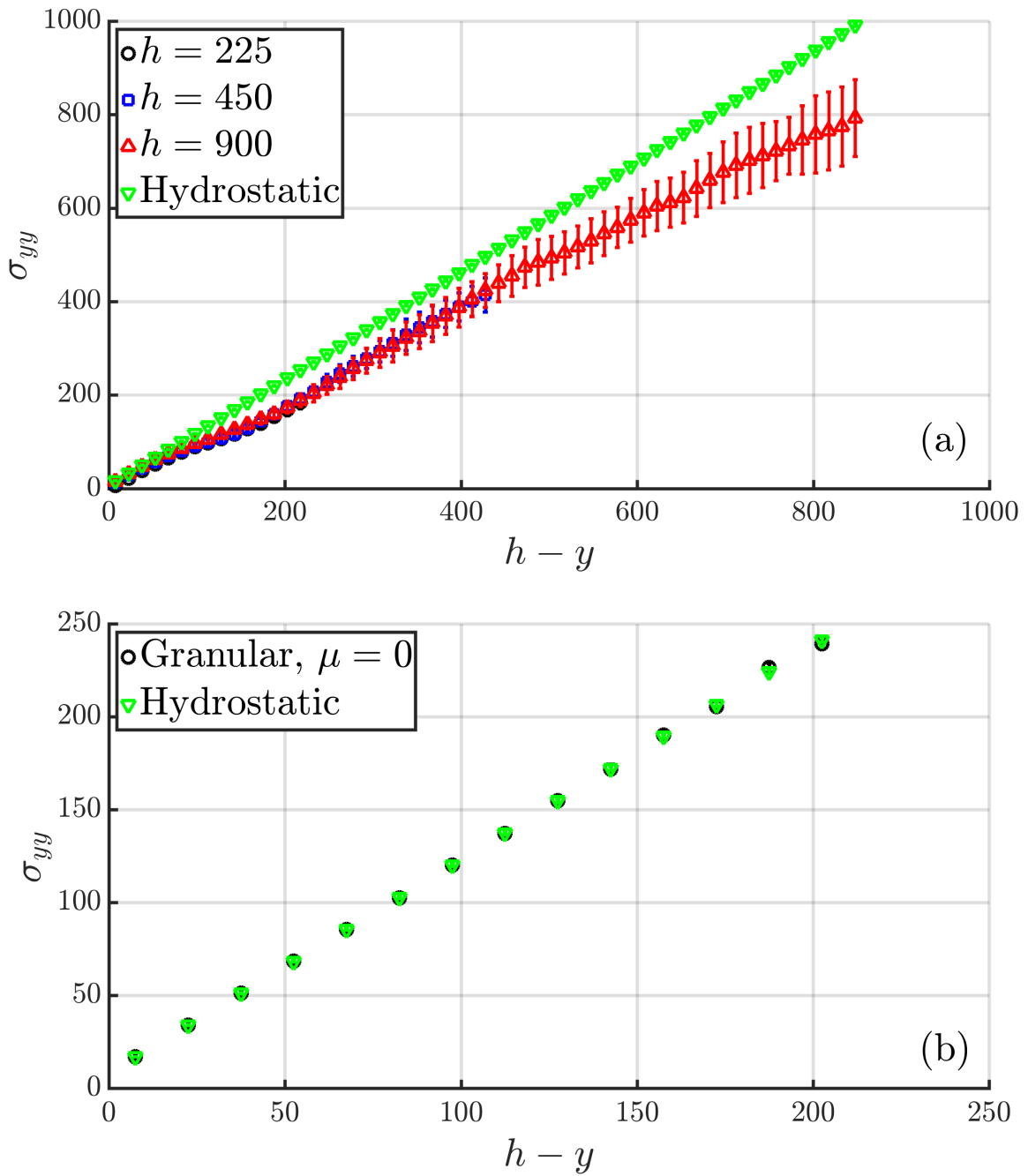
Fig. 5.4 Horizontal stress as a function of the vertical coordinate in a granular column for $W = 30$, $\mu_w = 0.5$, and three different fill-heights of the granular column, created by the S2 method. Horizontal stress behaves similarly to the vertical stress and agrees with the Janssen's assumption that stress inside a granular column is isotropic. Error bars are the standard deviation obtained by running 20 different ensembles at each height.

5.3.2   The V1 protocol

To understand the variation of σ_{yy} with vertical coordinate and the unexpected maximum observed in the S2 protocol, we decided to investigate the role of wall-forces and reconcile it with the common knowledge that wall-forces carry a significant part of the load in granular systems. For this, the variation of σ_{yy} with the vertical coordinate in the V1 protocol is examined. Our instinct was since all peculiar stress distributions must come due to inhomogeneous load borne by the walls, if we vibrate the column vigorously, we would break all arches transmitting stress to the walls, and this would make the maximum go away. After vibration, the fill-height decreases a little and the granular column becomes more compact. Here a question now arises — are the wall forces carrying much load in this newly rearranged column? Or are the particles just tightly squeezed? Figure 5.4 (a) shows the variation of σ_{yy} with $h - y$ for fill-heights $h = 225, 450$, and 900. For all the three fill-heights, the vertical component of stress increases almost linearly as we go down from the top of the column. There is a slight deviation from linearity for $h = 900$ as it reaches close to the bottom of the wall. The behavior of σ_{yy} is similar to what one observes in a compressible hydrostatic column. Hydrostatic stress gives the total stress that the grains would have applied if the load was not shared by frictional walls and is given by $\int \rho g dy$, where ρ is the mass density and is a function of the vertical coordinate.

So, we speculate that the walls in a granular column are not always carrying the load and particles in contact with the walls of the column are not always at the Coulomb friction limit, contrary to the assumption in the Janssen's model. This will be further discussed in section 5.4 and we will see that our speculation is correct by observing the wall forces at different protocols.

If we completely remove the friction from the system, a granular column will show hydrostatic behavior. In fact, the number density of particles is now practically a constant and so the stress is linear in the vertical coordinate. This is shown in Figure 5.4 (b). The granular column here is created by the S2 protocol for $W = 30$ and $h = 210$. This analysis tells us that the friction in the system is important, along with the protocol used to create the granular column as the V1 protocol almost completely attenuates the importance of friction in the system.

5.3.3   Protocol dependence

The particles in contact with the side walls are not always at the static friction limit. To get the particles closer to this limit a common practice is to use a column with a moving
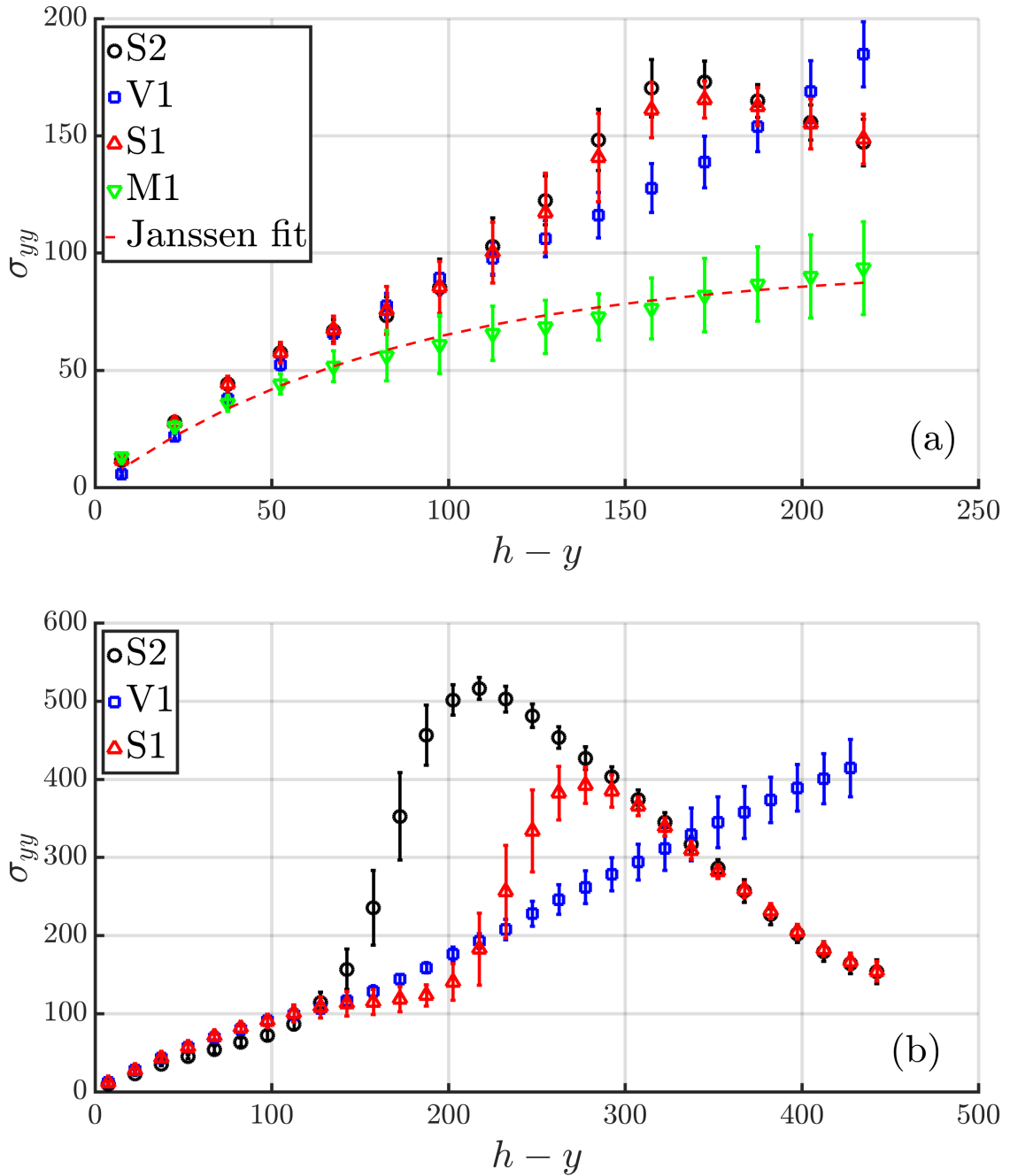
Fig. 5.5 (a) Comparison of vertical stress with the vertical coordinate for a granular column with $h = 225$, $W = 30$, and $\mu_w = 0.5$ obtained with four different protocols. The Viscous (S2) and Settling (S1) protocol seem to behave similarly for a column of this height. The vertical stress for the Vibration protocol (V1) increases linearly with $h - y$ [see Figure 5.4 (a)]. The Mobilize protocol (M1) does not have any maximum. Janssen form is a good fit for the M1 protocol and predicts $s = 85.53$. (b) At $h = 450$, the difference in σ_{yy} between the S1 and S2 protocols start appearing. Error bars are the standard deviation obtained by running 20 different ensembles at each height.

bottom wall (Vanel and Clément, 1999) or moving side walls (Bertho et al., 2003; Ovarlez et al., 2003). The movable wall is slowly moved to mobilize the particles near the walls. We also decided to follow this method to verify if the maximum observed in Figure 5.2 (a) disappears. We use a similar method as Vanel and Clément (1999) used to measure the pressure at the bottom and will refer to this method as the "Mobilize" (M1) protocol. In this method, the bottom wall of the final S2 packing is slowly moved downwards to mobilize the grains, and then the new packing is allowed to relax. The wall is moved by 10 units of height in 1000 units of time with the bottom wall moving sinusoidally as $-\mathrm{Sin}(\pi t/4000)$ with time. Note that the speed of downward displacement in Vanel and Clément (1999) was two orders of magnitude smaller than our average speed.

Figure 5.5 (a) shows the σ_{yy} variation with the vertical coordinate for all the four protocols at $h = 225$. The maximum disappears for the M1 protocol and the behavior far away from the free surface is the same as in Figure 3 of Landry et al. (2004). We speculate that mobilizing the bottom wall dilutes the effect of the initial protocol. The Janssen form as given in equation 5.11 seems to be a good fit for the M1 protocol and predicts a decay length of $s = 85.53$. This gives $K = 0.351$ and this value is close to the values referred to in Chapter 5 of Nedderman (2005) and obtained in earlier studies (Landry et al., 2004; Zhao et al., 2018). Note that an area-based packing fraction $\phi = 0.87$ was used for obtaining the Janssen fit.

Recall that S1 protocol is just a primitive version of the S2 protocol. We notice that the S1 protocol shows similar behavior as the S2 protocol at $h = 225$. This is, however, not true at $h = 450$ [Figure 5.5 (b)]. At $h = 450$, the S2 protocol shows a much bigger peak than the S1 protocol, which leads us to believe that the time at which viscosity is introduced in the system in S2 protocol is important. In the current S2 protocol, viscosity was introduced after 50 units of time for both $h = 225$ and 450. For $h = 900$, we introduced viscosity after 500 units of time (see Figure 5.2) as settling of grains takes much more time at this height. In Landry et al. (2004), the extra viscous damping force was introduced when the kinetic energy per particle reaches $10^{-3}Mgd$, as they found that at this value the kinetic energy in their system was getting stabilized. We did not face any such issues and hence decided to introduce viscosity at later times as discussed above. One of the reasons we did not face this issue can be because of our higher viscoelastic damping constant for normal contacts. In our simulations, $\gamma_n = 500$ and in Landry et al. (2004) it was taken to be 50.
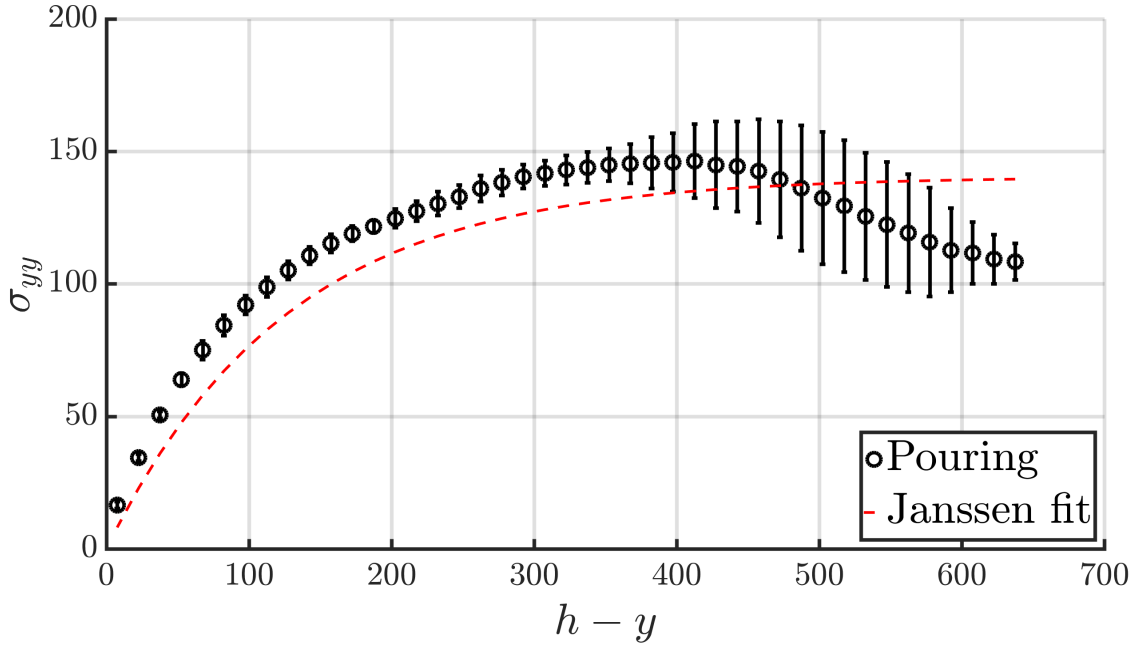
Fig. 5.6 Variation of the vertical component of stress with $h - y$ for the pouring protocol at $W = 30$ and $\mu_w = 0.5$. Error bars are the standard deviation obtained by running 20 different ensembles at each height. The Janssen form obtained by using equation 5.11 for $\phi = 0.87$ gives the decay length $s = 126.8$.

5.3.4 Pouring protocol

The behavior of the M1 protocol is closer to the Janssen's model than that of the other protocols as shown in Figure 5.5 (a). One of the widely used protocols that we have not discussed until now is the "Pouring" or raining protocol. In this protocol, an insertion region of width W and height 1 is chosen above the desired fill-height. This is done to mimic pouring of particles from a fixed height into the given container. Non-overlapping particles are placed randomly in this region to keep a volume fraction of 0.26 inside the insertion region at each time step. Inserted particles are not allowed to overlap and up to 100000 attempts are made to insert each new particle without overlaps. Landry et al. (2004) also used the same protocol for measuring total vertical stress in the granular column at different fill-heights. To compare our results with Landry et al. (2004), we use particles with diameters in the range of 1 to 1.1 and fill the $W = 30$ column with 20000 particles. Viscous damping force was used to drain the kinetic energy after all the particles have settled in the column and the total kinetic energy of the system is less than 10^{-5}. For this simulation, the parameter values for Hertzian interaction were taken

from Landry et al. (2004). Therefore, we fix $\gamma_n = \gamma_t = 50$ and all the other parameter values remain the same as in section 5.1 of this chapter.

Variation of the vertical component of stress with $h - y$ has been shown in Figure 5.6. Landry et al. (2004) and Vanel and Clément (1999) saw a hydrostatic-like region at the top of the packing until a cut-off y value in their work. We do not see any such region. However, such regions are visible in the S1 and S2 protocols and become very clear when plotted together with the V1 protocol as shown in Figure 5.5. We also see a slight dip in Figure 5.6 near the bottom of the granular column which was not observed in Landry et al. (2004). The difference can be attributed to the fact that Landry et al. (2004) measured the vertical component of the global stress tensor in their work at different fill-heights and not components of the local stress tensor. In other words, they measured the stress of the whole granular column, whereas we measured the stress in horizontal strips of 15 x W at different y for one particular column height. The comparison of the vertical stress profile with the Janssen's prediction (given by equation 5.11) gives a poor fit as shown by the dotted line in Figure 5.5. The fit predicts a decay length of $s = 126.8$.

One should note that the Pouring protocol and S1 or S2 protocol are very different. In the S1/S2 protocol, the packing at the bottom is created by particles settling gently from a small height. As discussed before, the initial zero velocity non-overlapping particles are placed in height 1 to H_{int} while using the S1/S2 protocol. The packing at the larger vertical coordinate is created by particles falling with high speed from a larger height. Whereas, in the Pouring protocol, the packing at the bottom is created by particles falling from a large height at high speed and packing at the top is created by the particles settling at smaller velocities. This important difference is the reason behind such contrasting stress profiles between the Pouring protocol and the S1/S2 protocol.

5.3.5 Bidisperse

Till now, all of our studies have been done by using monodisperse particles. A packing of monodisperse particles tends to crystallize in 2D. Now the question arises, can crystallinity in the packing be a reason for the peculiar behavior of vertical stress profile? To answer this, we study a disordered packing created by the S2 protocol. Bidisperse particles are used to create disordered packing in 2D and we compare our results of monodisperse packing with that of bidisperse packing.

We created a bidisperse packing filled with an equal number of particles of diameter $d_1 = 1$ and $d_2 = 1.2$. The granular column was created by the S2 protocol and the case of $h = 225$ was analyzed. The comparison of a bidisperse-filled granular column with monodisperse packing has been shown in Figure 5.7. The maximum observed in the
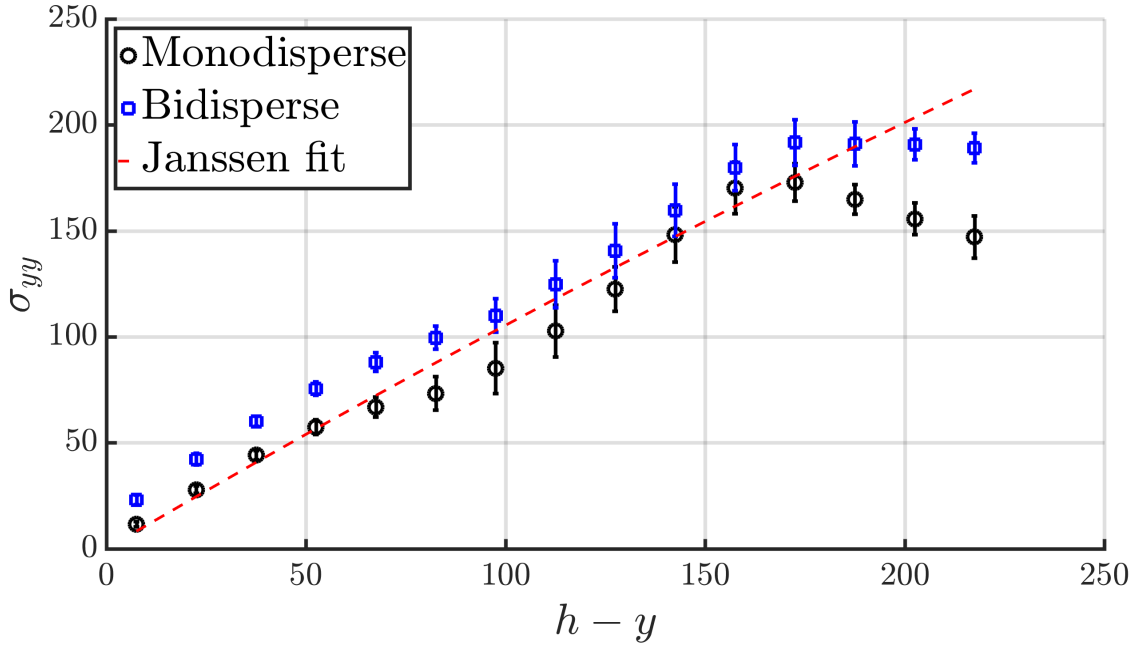
Fig. 5.7 Comparison between the same size monodisperse and bidisperse-filled granular columns suggests that the behavior seen in bidisperse packing might be different from that of monodisperse packing. The $W = 30$ container was created by the S2 protocol and $\mu_w = 0.5$ in both the cases. The maximum observed in monodisperse packing disappears in bidisperse packing. Still, the Janssen form (with $\phi = 0.87$) appears to be a poor fit for bidisperse packing created by the S2 protocol. Error bars are the standard deviation obtained by running 20 different ensembles at each height.

vertical stress for the monodisperse case disappears in the bidisperse packing at $h = 225$. We see a linear region near the top of the packing similar to the monodisperse packing, which was also observed by Vanel and Clément (1999) and Landry et al. (2004). But after this hydrostatic-like region, σ_{yy} saturates and becomes constant. Janssen's model (showed by the red-dashed curve) appears to be a poor fit for the bidisperse packing as well while using this protocol. The Janssen form predicts $s = 1017.8$ which is larger than observed in Figure 5.1 (b). In the future, we will like to study if this behavior of bidisperse packing continues at larger fill-heights or if a maximum in the vertical stress appears like in the monodisperse case.

5.4   Model

To understand the counter-intuitive result seen for the vertical stress variation with the vertical coordinate in the S1 and S2 protocols, we decide to relax all the assumptions made in the Janssen's model and start by constructing a new force balance. We consider a thin horizontal strip of height Δy and width W within our computational domain. As per the force balance, the weight of the particles in this strip must be equal to the upward shear force applied by the wall, plus the upward reaction force applied by the particles below and minus the downward force applied by the particles above. So,

$$Mgn(y)\Delta yW = (\sigma_{yy}|_{y+\Delta y} - \sigma_{yy}|_y)W + 2\sigma_{xy}|_{\text{wall}}\Delta y. \tag{5.4}$$

Here $\sigma_{xy}|_{\text{wall}}$ is the shear stress applied by the wall and $n(y)$ is the number of particles in the unit area at height y. If $\phi(y)$ is the packing fraction based on area, we have, assuming no significant compression of the particles,

$$n(y) = \frac{4\phi(y)}{\pi d^2}. \tag{5.5}$$

In the limit of $\delta y \to 0$, equation 5.4 becomes

$$\frac{4Mg\phi(y)}{\pi d^2} - \frac{d(\sigma_{yy})}{dy} - 2\frac{1}{W}\sigma_{xy}|_{\text{wall}} = 0. \tag{5.6}$$

Note, at this point, we can get Jannsen's equation by assuming ϕ to be a constant at all y and $\sigma_{xy}|_{\text{wall}} = \mu_w\sigma_{xx} = \mu_wK\sigma_{yy}$. This gives us:

$$\frac{4Mg\phi}{\pi d^2} - \frac{d(\sigma_{yy})}{dy} - 2\frac{\mu_wK}{W}\sigma_{yy}|_{\text{wall}} = 0, \tag{5.7}$$

$$\sigma_{yy} = \frac{2Mg\phi W}{\mu_wK\pi d^2}\left(1 - e^{\frac{-2\mu_wK}{W}(h-y)}\right). \tag{5.8}$$

Writing equation 5.8 in its familiar form, we get

$$\sigma_{yy} = \rho gs\left(1 - e^{-\frac{h-y}{s}}\right), \tag{5.9}$$

where $\rho = 4M\phi/\pi d^2$ and $s = W/2\mu_wK$. Equation 5.9 is the famous Janssen's equation as discussed in Chapter 1. Both equations 5.6 and 5.8 are retained in dimensional form. Non-dimensionalising the stress with Mg/d (force/length, as our system is two

dimensional) and all the length scales by d, we get:

$$\frac{4\phi}{\pi} - \frac{d(\sigma_{yy})}{dy} - \frac{2}{W}\sigma_{xy}|_{\text{wall}} = 0, \tag{5.10}$$

$$\sigma_{yy} = \frac{4\phi s}{\pi}\left(1 - e^{-\frac{h-y}{s}}\right). \tag{5.11}$$
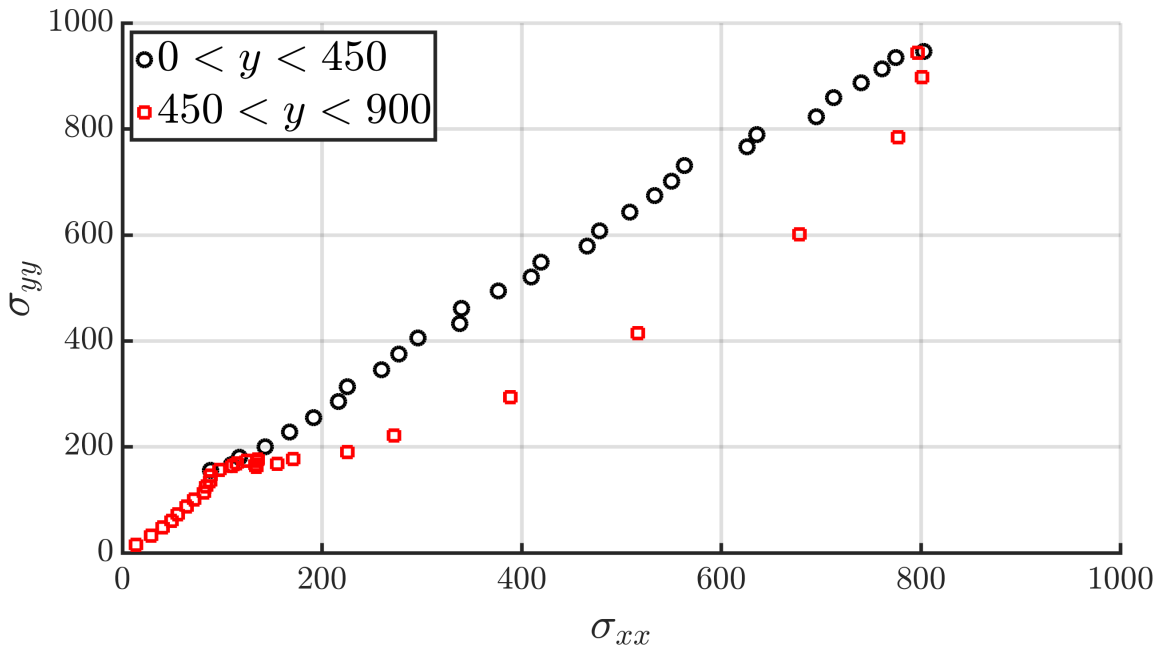
Fig. 5.8 Scatter plot of the vertical stress with the horizontal stress. The packing is created by the S2 protocol at $W = 30$ and $h = 900$. Black circles represent a region from $y = 0$ to the vertical coordinate in the column at which the maximum in the vertical stress is observed. Red squares represent the region from this vertical coordinate to the free surface of the packing.

Now, it is clear that Janssen's equation (equation 5.11) is a special case of equation 5.10 and is not valid if (i) the stress is anisotropic or (ii) the packing fraction varies with the vertical coordinate or (iii) the particles at the wall are not mobilized. We have already seen in Figure 5.3 that the behavior of horizontal stress is quite similar to the vertical stress for S2 protocol. Our tests showed that this is true for all the protocols. Figure 5.8 shows a scatter plot between vertical stress and horizontal stress for a granular column created by the S2 protocol. We realize that other than a small region in the middle of the column, $\sigma_{yy} \propto \sigma_{xx}$. The small region where this is not true is the region just before the maximum in Figure 5.2 (a), if one is going down the column from the top.
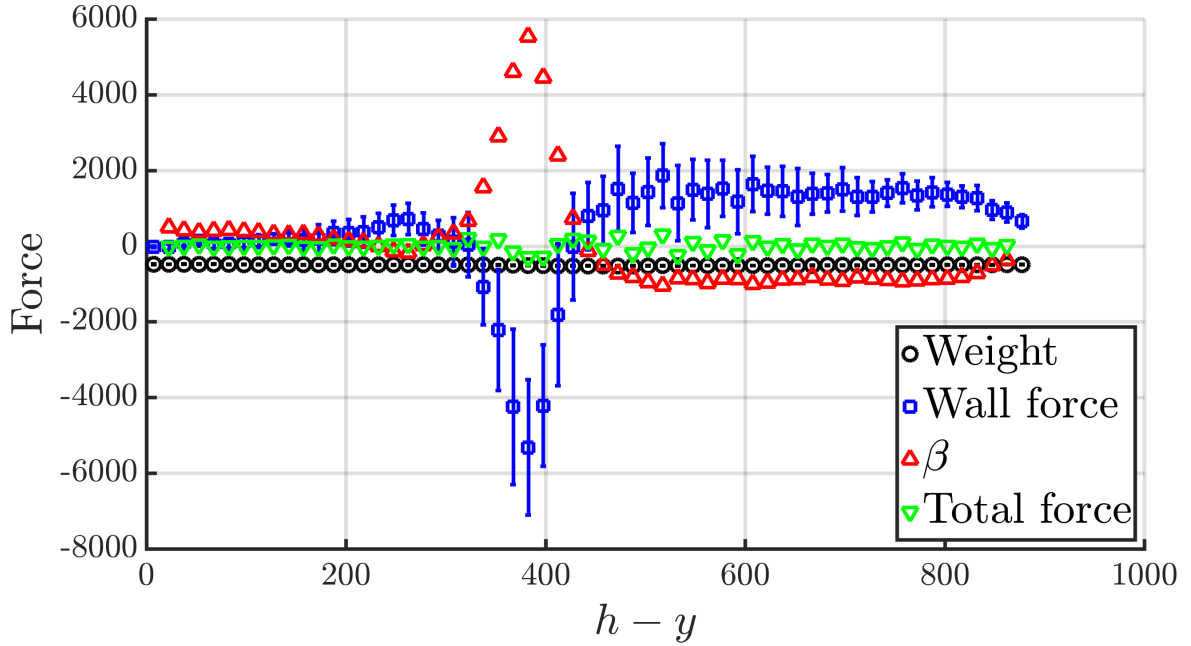
Fig. 5.9 Force balance at different vertical coordinates of the granular column. Here β is the vertical force difference from above and below of a section of thickness Δy at any y and is given by $(\sigma_{yy}|_{y+\Delta y} - \sigma_{yy}|_y)W$. Note that the compressive stress has been shown as positive in previous figures. But, while differentiating it is taken as negative and therefore we get the present behavior of β.

Equation 5.10 shows us that the gradient of vertical stress can be positive in one region and negative in another region based on how the packing fraction changes with y and how much load the side walls are carrying. Hence, studying packing fraction and wall-forces should help us in understanding the peculiar behavior of vertical stress in the column. To start, we will use this force balance to understand how wall-force changes with the vertical coordinate in comparison with the vertical stress.

Equation 5.10 shows us that the gradient of vertical stress can be positive in one region and negative in another region depending on how packing fraction is changing with y and how much load the side walls are carrying. Hence, studying packing fraction and wall-forces should help us in understanding the peculiar behavior of vertical stress in the column. First, we will use this force balance to understand how wall-force changes with the vertical coordinate in comparison with the vertical stress. Figure 5.9 shows the force balance at different vertical coordinates in a $h = 900$ granular column prepared by the S2 protocol. The net force is zero at all y as expected for a static granular column. The most important observation here is the interesting behavior of the force applied
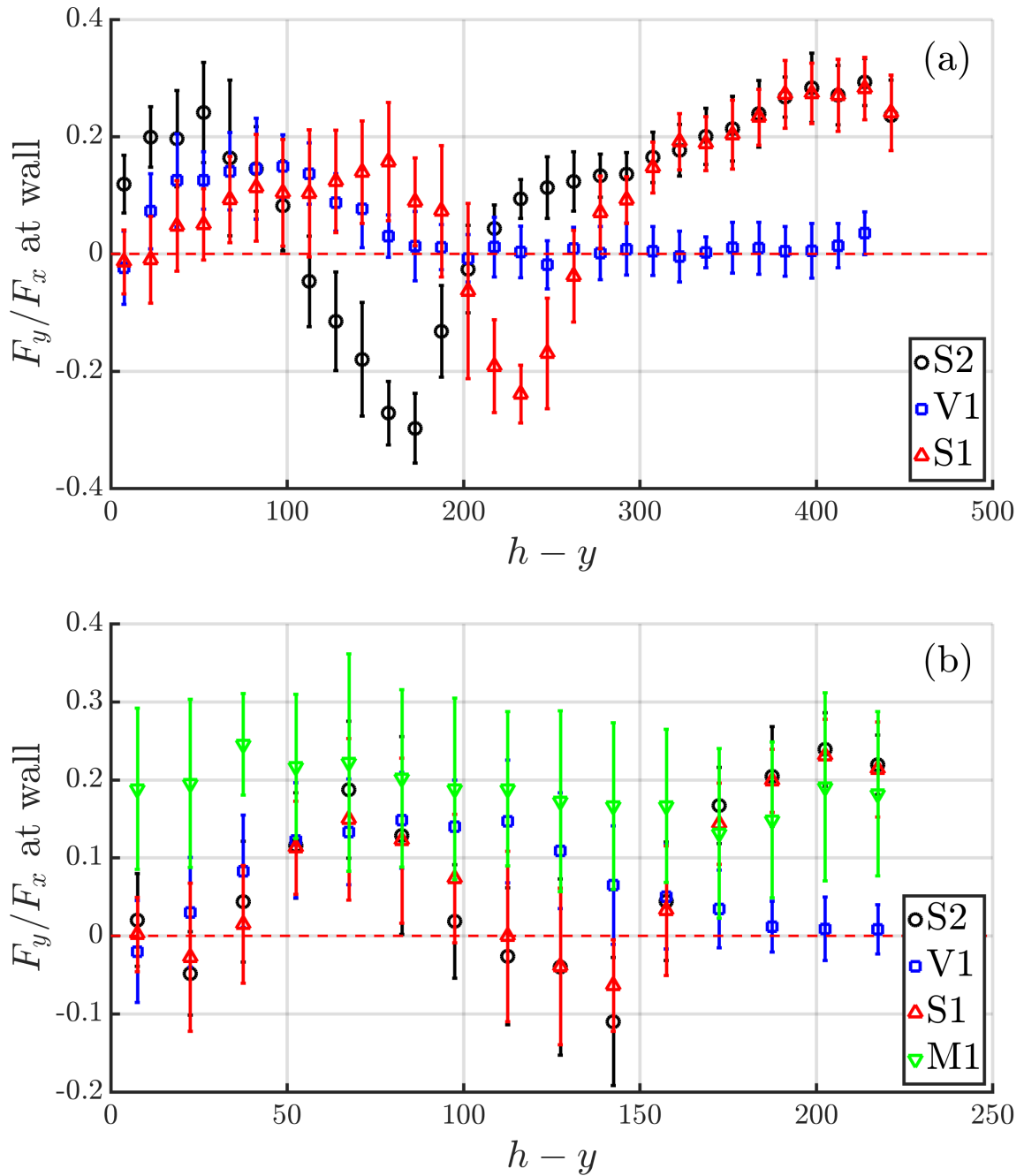
Fig. 5.10 Variation of F_y/F_x with the vertical coordinate for the S2 protocol, $W = 30$, and (a) $h = 450$ and (b) $h = 225$. F_y and F_x are the vertical and horizontal force applied by the side-walls on the particles. Note that F_x is of opposite signs on the two side walls but for clarity of this figure we take it to be always positive. Therefore, negative F_y/F_x represent a region where F_y is negative. Error bars are the standard deviation obtained by running 20 different ensembles at each height.

by the side walls. Interestingly, we find that there is a region in which the side walls are applying downward force on the column just before the maximum in σ_{yy} profile [see Figure 5.2 (a)]. This is also the region which showed a slight deviation from isotropy in Figure 5.8. Such regions can exist in a static granular system depending upon the history of the contacts in the system as is pointed out in section 5.6 of Nedderman (2005). So it is of prime importance to study the formation of these packings in the S1 and S2 protocol and we will discuss this in the coming paragraphs.

Another observation comes by comparing the ratio of the vertical force with the horizontal force applied on the particles by the side walls in different protocols as shown in Figure 5.10 for (a) $h = 450$ and (b) $h = 225$. This figure shows us that the vertical force on the walls is below the Coulomb yield limit of $\mu_w F_x$, as assumed in the Janssen's model, for all the protocols. The negative value of F_y/F_x shows that there is a region where the side-wall is applying a downward force on the particles. In the V1 protocol, there is no region in Figure 5.10 (a) and (b) where side-walls are applying downward force on the particles. From Figure 5.10 (a), it is clear that F_y/F_x is lowest for the V1 protocol in most of the region. F_y/F_x saturates to zero near the bottom surface. This is not due to the fact that the side walls are not carrying any load, but a consequence of F_x becoming large in the region close to the bottom of the column. Notice that the Mobilize protocol has a constant F_y/F_x value in Figure 5.10 (b) and therefore is closest to the Janssen's model. The M1 protocol case also has the largest F_y/F_x value amongst all the protocols suggesting that the particles are more mobilized near the side walls in this protocol. There is no region in Mobilize protocol where side walls are applying downward force on the particles. Hence, we do not see any maximum in this protocol.

The peculiar behavior of σ_{yy} in the S1 and S2 protocols can be understood by understanding how the particles are being packed in the columns when we use these protocols. Figure 5.11 shows the variation of packing fraction for different fill-heights in the S2 protocol. The behavior of packing fraction is similar to what we observed for vertical stress in the S2 protocol. In particular, the location of maximum between $h - y = 425$ to 445 for $h = 900$ is the same as that of the vertical stress. So, it is not difficult to say that an assumption of packing fraction being a constant is not quite correct. Furthermore, the two observations, the vertical stress and packing fraction, are coupled with each other in a way suggested by equation 5.10. In fact, a scatter plot between the vertical stress and the packing fraction as shown in Figure 5.12 shows a systematic behavior, approximately linear, suggesting that the coupling between the two is strong.
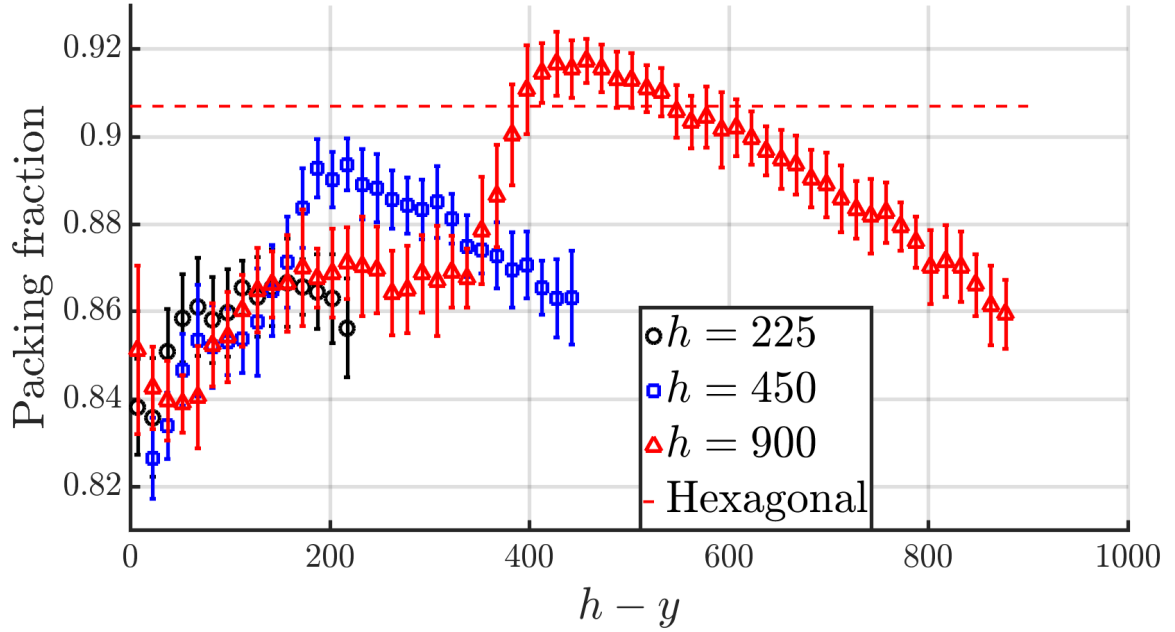
Fig. 5.11 Variation of area-based packing fraction with the vertical coordinate for different fill-heights. The packings are created by the S2 protocol at $W = 30$. The red dashed line represents hexagonal close packing in 2D. Error bars are the standard deviation obtained by running 20 different ensembles at each height.

Maxima similar to those in the vertical stress plots are seen for $h = 450$ and $h = 225$ also in Figure 5.11. No such maximum is observed for the V1 protocol as shown in Figure 5.13. As you reach closer to the bottom surface, the packing fraction increases in the V1 protocol. In fact, it goes above the hexagonal crystalline packing value of 0.907 at $h - y > 300$. This means that the particles are heavily squeezed in the granular column in the V1 protocol because of vibrations.

The maxima in Figure 5.11 and Figure 5.13 for the S2 protocol represents a region around which the particles are tightly squeezed, so much so that the packing fraction can even go beyond hexagonal crystalline packing limit for $h = 900$. Similar behavior is expected from the S1 protocol. The question is why such a region exists in the S1 and S2 protocol in the middle of the column. This can be understood from Figure 5.14, which shows us the formation of the $h = 450$ granular column by the S1 protocol. Figure 5.14 is obtained by taking a snapshot of the whole container at different time frames. At $t = 47$, the particles are still settling under gravity. The times are in non-dimensional units. At $t = 49$, the grains near the free surface start heaving/bouncing upwards, followed by the grains below the free-surface. This happens because while the particles are settling in the
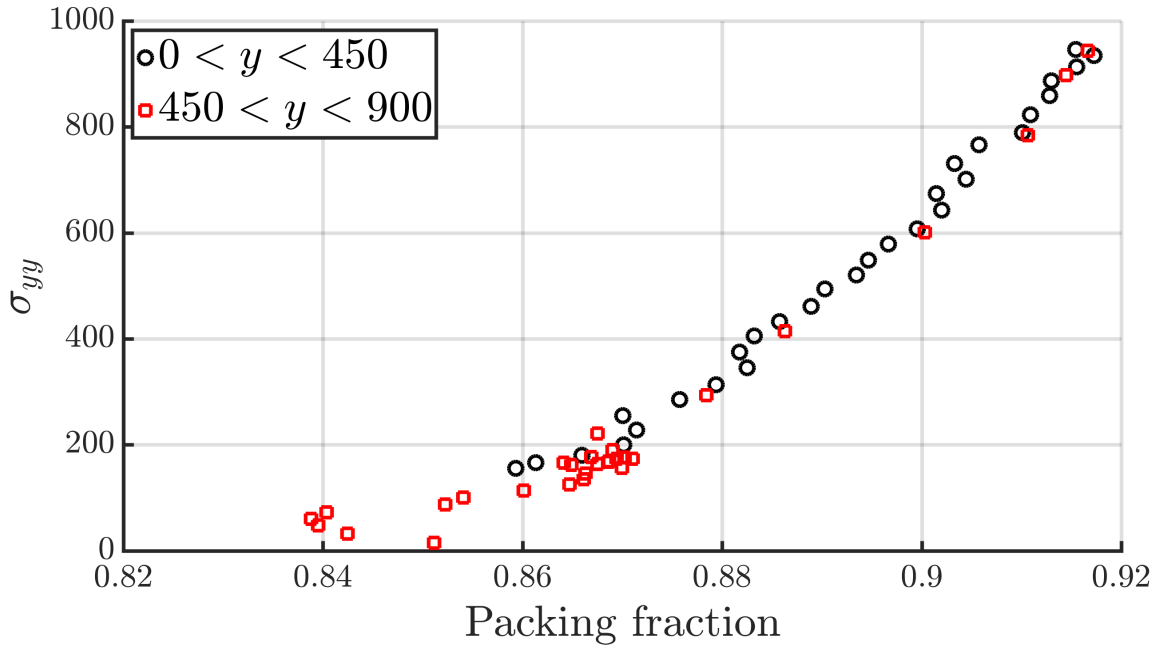
Fig. 5.12 Scatter plot of the vertical stress with the area-based packing fraction. The packing is created by the S2 protocol at $W = 30$ and $h = 900$. Black circles represent a region from $y = 0$ to the vertical coordinate in the column at which the maximum in the vertical stress is observed. Red squares represent the region from this vertical coordinate to the free surface of the packing.

container at initial times, there is a continuous bombardment of high-velocity particles happening at the top as shown in the case of $t = 47$. We provide a descriptive account below.

Remember that the S1 protocol is created by allowing particles with zero initial velocity, placed randomly between height 1 to H_{int}, to settle. The H_{int} is 800, 1600, and 3200 for $h = 225$, 450, and 900 respectively. Hence, the packing at the bottom is made from particles settling from a small height. But as we go up in the column, the structures are formed by the bombardment of high-velocity particles coming down from a greater height. This leads to the particles getting increasingly squeezed in the column as shown in Figure 5.15. The strength of the force network increases with height till all the particles have fallen. At this moment the vertical stress (and packing fraction) increases almost linearly with the vertical coordinate as shown in Figure 5.16.

This continues till $t = 49$ when all the particles have settled. At this moment, the heavily compressed region at the top has a net upward force acting on it due to this compression, and it achieves a more relaxed state by heaving up as shown in Figure 5.14.
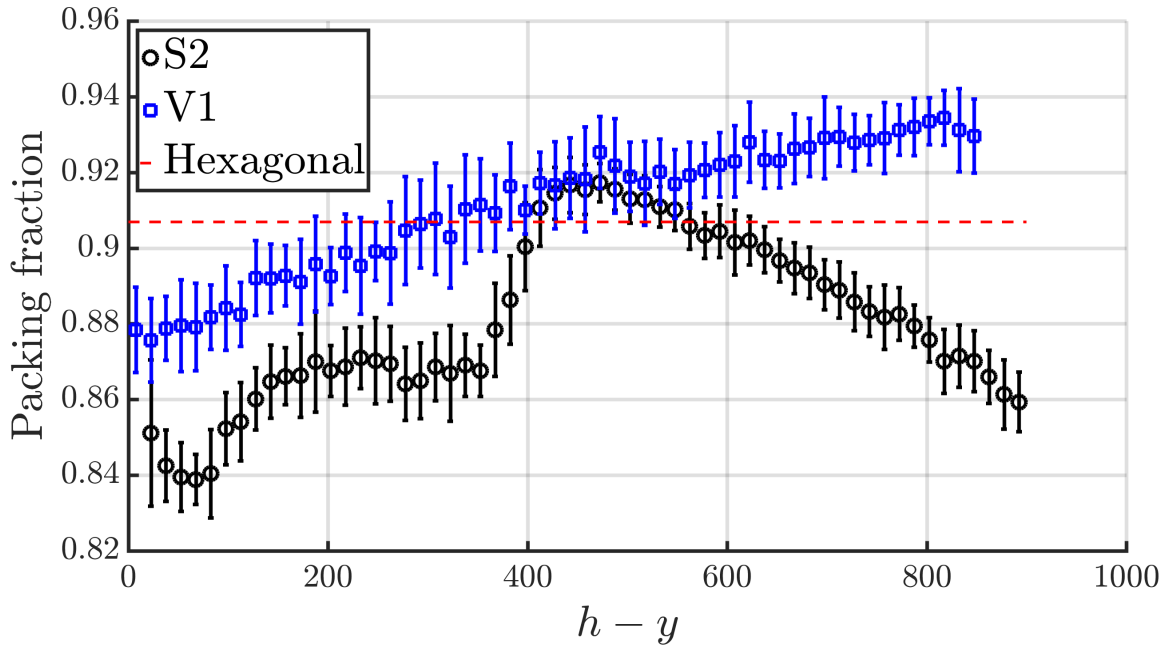
Fig. 5.13 Variation of area-based packing fraction with the vertical coordinate for the S2 and the V1 protocol at $h = 900$ and $W = 30$. The red dashed line represents hexagonal close packing in 2D. Error bars are the standard deviation obtained by running 20 different ensembles at each height.

Using the large stored elastic potential energy (due to compression), first the particles near the free surface bounce, followed by the particles just below it. The particles in the compressed region in the top part of the column are able to bounce freely during $55 > t > 49$ and falls back again during $73 > t > 55$, this time from a very small height. The particles at the bottom part of the column do not heave as the deformation in this region is smaller compared to the particles at the top and because of the space constraint.

The particles in the top part of the column settle gently after heaving, as is evident by looking at the force networks in Figure 5.15. All the strong force chains (shown in red) at the top of the column at $t < 49$ disappear at $t = 73$ and therefore the column is not under compression in this region. The stress now increases as we go down the column in this region as shown in Figure 5.16. Below this region lie the particles which are still under compression (less at the bottom, more at the top) and hence the stress decreases as we go further down. The combination of the two loads during the re-setlling process — (i) the compressive force because of which some particle in the middle of the column wants to relax and (ii) the amount of downward force, on the same middle
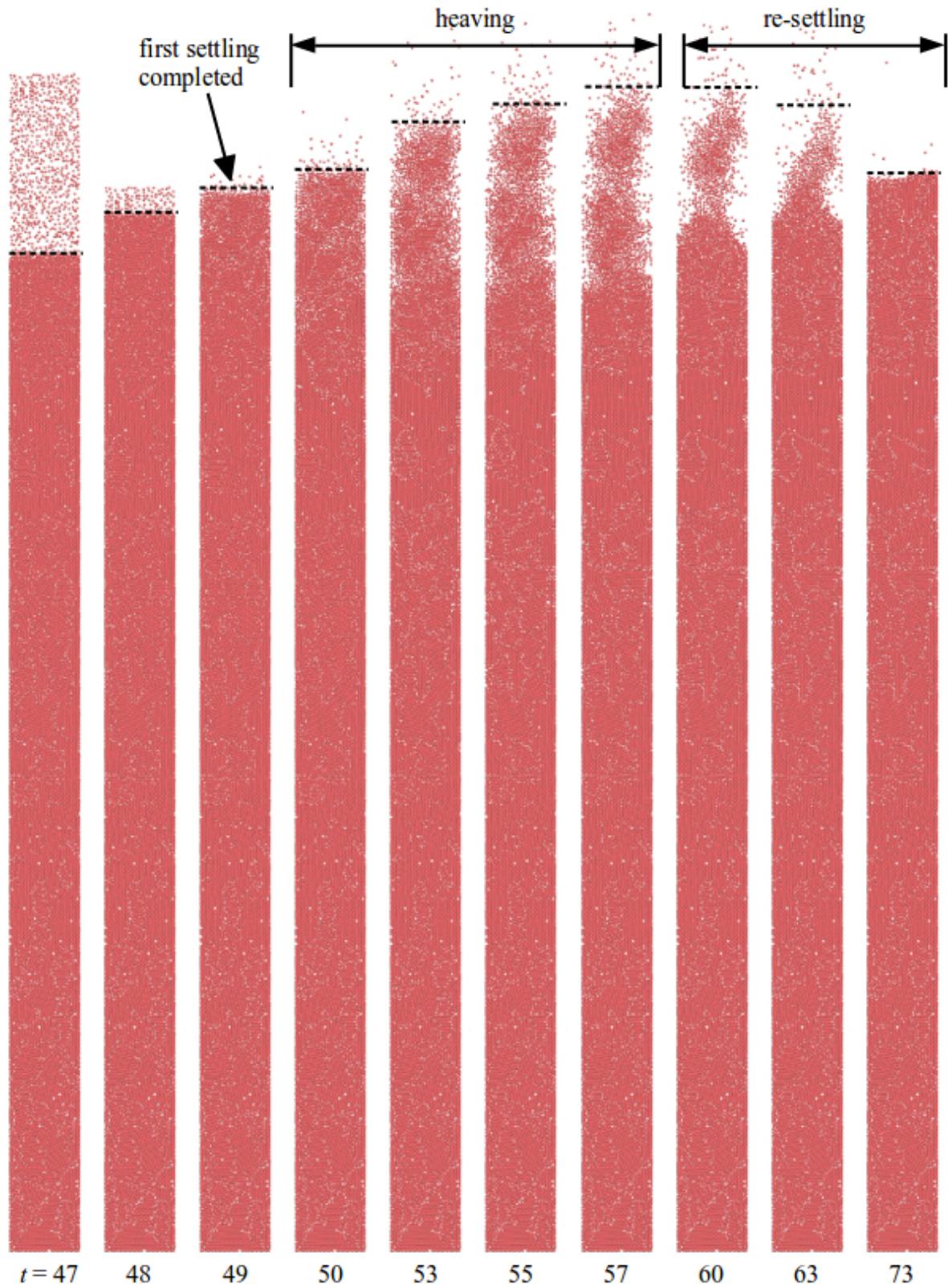
Fig. 5.14 Formation of a granular column shown for the S1 protocol with $W = 30$ and $h = 450$. The dotted line shows an approximate free surface of the packing. Numbers below the image gives the time frames t at which the image is captured. At $t = 47$, the particles are still falling under gravity. Once all the particles have settled ($t = 49$), the top part of the column heaves.
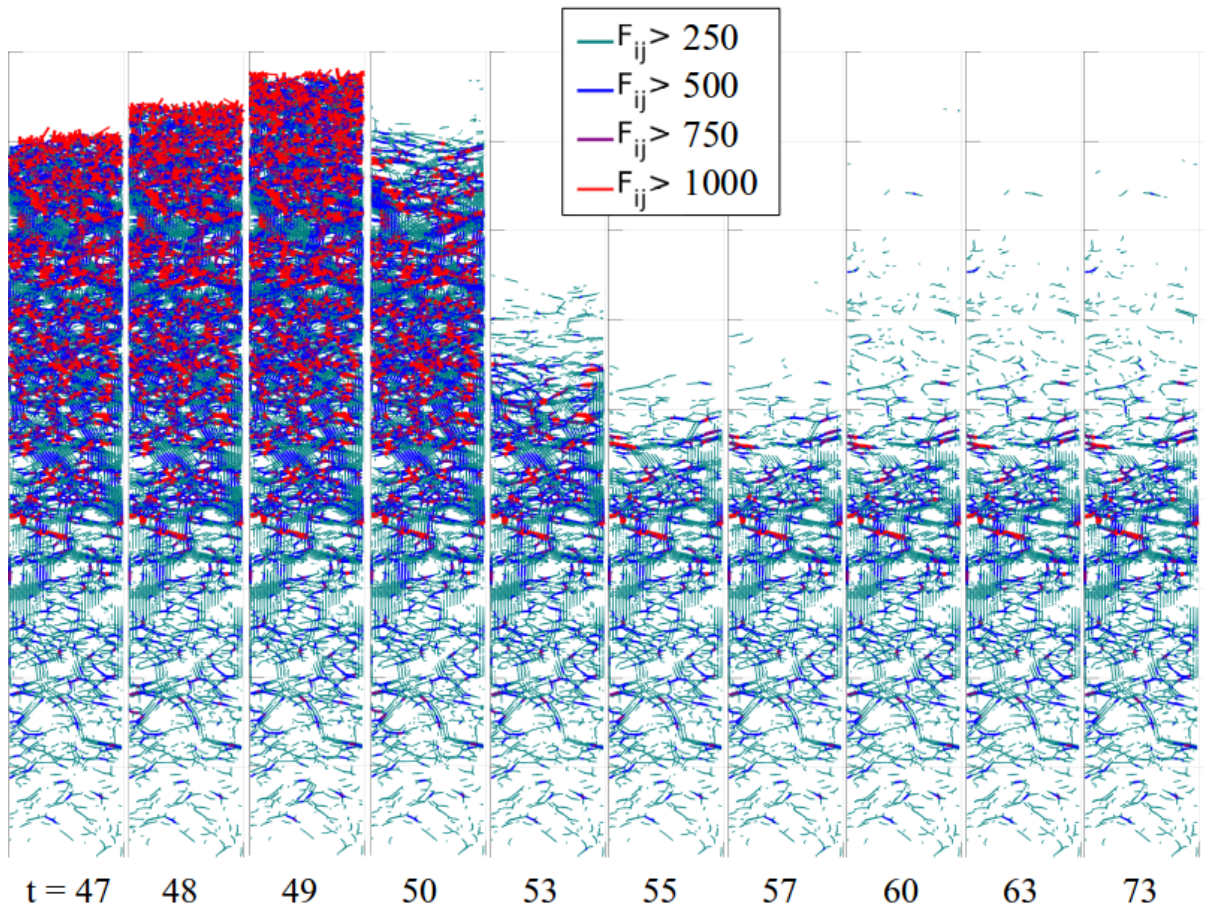
Fig. 5.15 Force network during the formation of the granular column shown for a single run of the S1 protocol, with $W = 30$ and $h = 450$. Different colors represent the magnitude of the contact forces F_{ij}; $F_{ij} < 250$ data are not shown for clarity. Numbers below the image give the time frames t at which the image is captured. At $t = 47$, the particles are still falling under gravity. Once all the particles have settled, the top part of the column heaves as shown in images at $t > 49$.
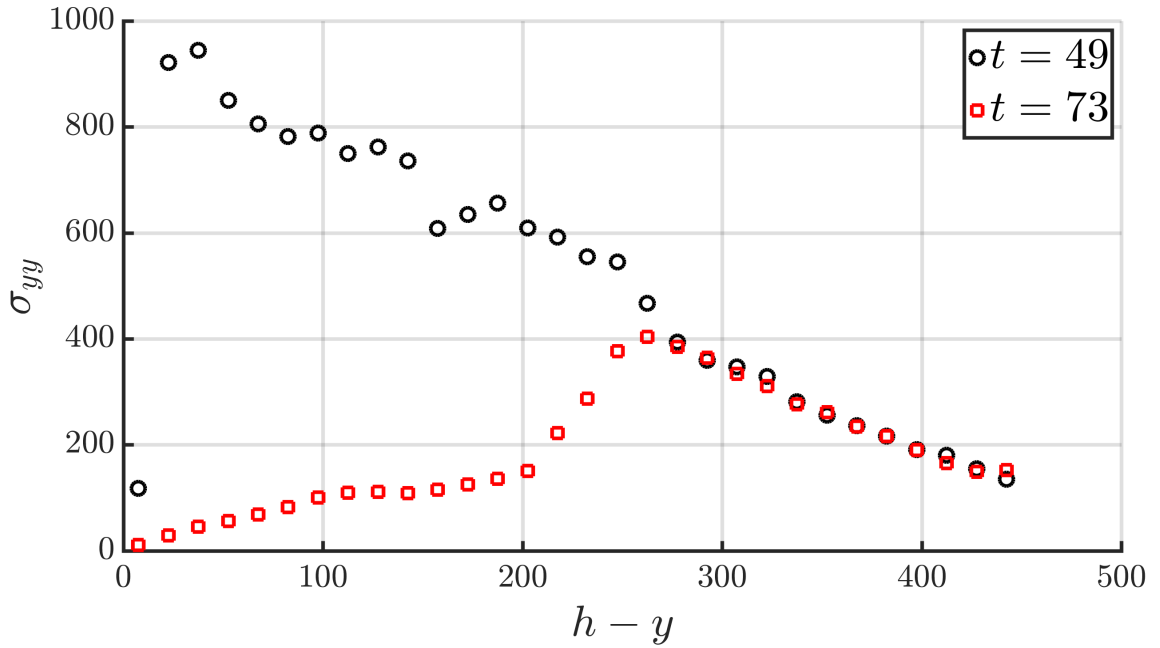
Fig. 5.16 Variation of vertical stress with the vertical coordinate for a single run of $h = 450$, S1 protocol, at two different times. $t = 49$ represents a time before heaving and $t = 73$ represents a time when heaving is finished.

layer of particles, due to resettling particles from above — decides the region where the maximum of the stress and packing fraction occurs.

As we discussed above, the particles in the middle of the column are still under compression and are attempting to relax to a lower energy state. Since they are in a state of compression (vertically and horizontally both), a spanning force network can also form, which prevents further upward motion of the particles in the middle and bottom region (Cates et al., 1998; Farr et al., 1997; Majmudar et al., 2007). The upward force applied by the particles in the middle and the particles at the bottom, trying to relax, on this force network is less than μ_w times the normal compressive force applied by the network on the wall. So, these particles apply a net upward force on the side walls and the side walls apply equal and opposite downward force on these particles as per Newton's third law. Hence, we see a region in the middle of the column with a negative wall force on the particles. The column thus freezes in this configuration. The fact that such a maximum is harder to observe at larger widths [see Figure 5.2 (b)] is indicative of the lower propensity to form a spanning force network.

As discussed in section 5.3.4, the packing at the bottom in the Pouring protocol is created by particles impacting at high velocities and at the top by gently settling or low impact speed particles. Hence, we do not see similar behavior of the S1/S2 protocol in the stress profiles in the Pouring protocol.

5.5 Variation with the horizontal coordinate

For the sake of completeness, we will also like to discuss the variation of the vertical stress with the horizontal coordinate in different protocols. This is a part which has been accorded with little attention in previous investigations. We start with the S2 protocol and see the variation of stress for different fill-heights as shown in Figure 5.17 (a). For all fill-heights, a slight increase in σ_{yy} near the center of the column is observed. This suggests that the load near the center of the column is more than that near the walls and the effect of wall-friction might not be felt completely far away from the walls. This weak maximum near the center of the column should become more prominent for larger width granular column. To verify this, the variation of σ_{yy} with the horizontal coordinate for three different widths at fill-height $h = 225$ is plotted as shown in Figure 5.17 (b). The x coordinate for larger widths has been scaled to fit in the range of 0-30 to compare with the $W = 30$ plot. As expected, the maximum becomes more pronounced at $W = 60$ compared to that at $W = 30$. Interestingly enough, a plateau-like region is observed at the center of the column at $W = 90$.

A similar comparison of the vertical stress variation with the horizontal coordinate is done for different protocols coordinate as shown in Figure 5.18. Plots for (a) $h = 225$ and (b) $h = 450$ show maximum σ_{yy} at the center of the granular column for all protocols. Similar to Figure 5.5 (a), the values of σ_{yy} at every x coordinate for the Mobilize protocol is less than that for any other protocol. But unlike Figure 5.5 (a), the V1 protocol case has similar σ_{yy} values as the V1 and S1 protocols within error bars at every x value. This changes at larger height as shown in Figure 5.18 (b), where the behavior of the S1, S2, and V1 protocols are all different.

5.6 Discussion and Future work

This chapter explained how the protocol used for preparing a granular column is very important and how it governs the local packing of the column. We discussed various protocols used for preparing the granular column — Settling, Viscous, Vibration, Pouring, and Mobilize protocol. We showed that using the S1/S2 protocol for preparation of a
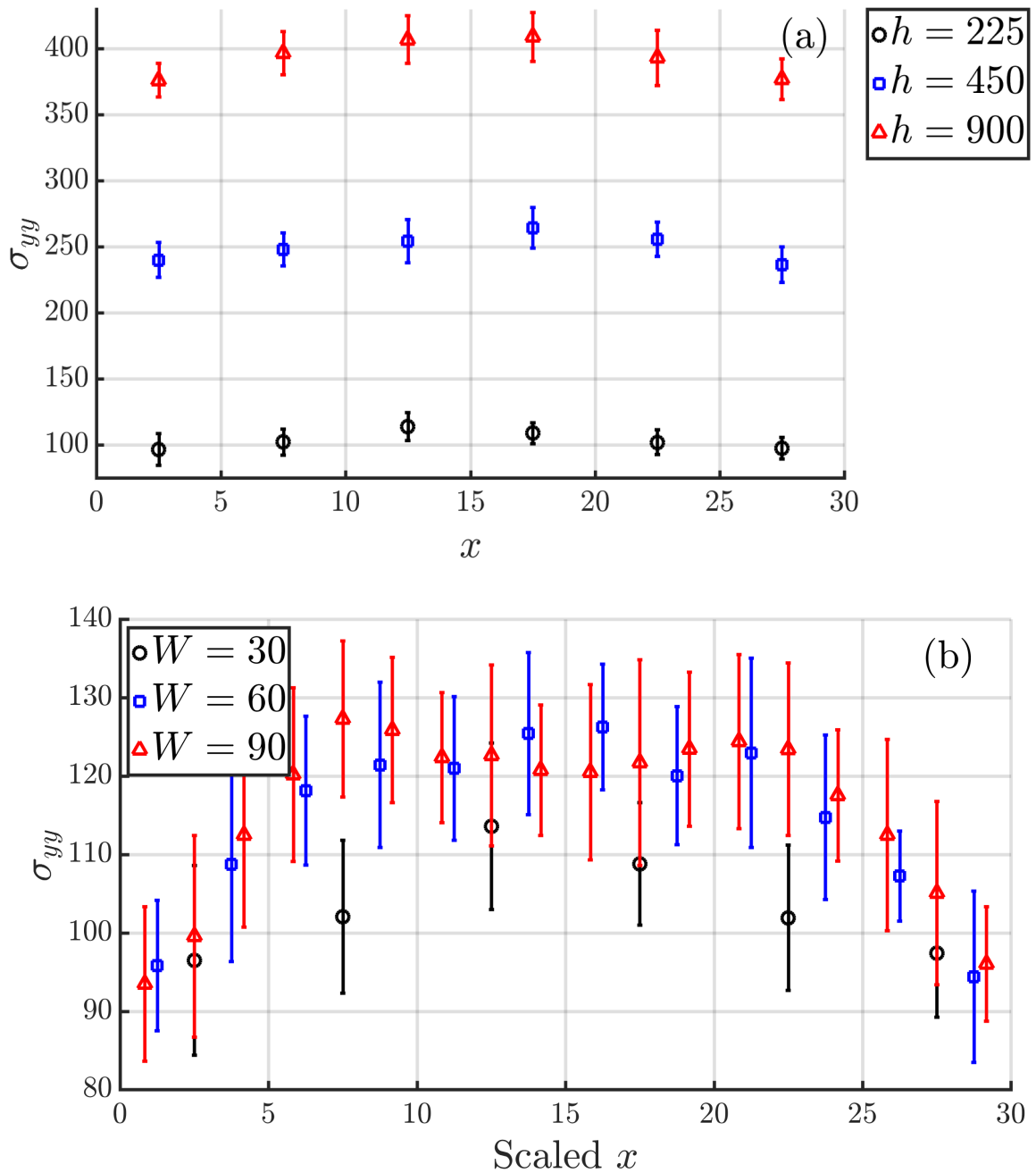
Fig. 5.17 (a) Vertical stress as a function of the horizontal coordinate for three different fill-heights at $W = 30$ and $\mu_w = 0.5$, created by the S2 method. At any x, σ_{yy} is obtained by measuring the vertical stress in vertical strips of size 5 x h. For all fill heights, we see a small increase in σ_{yy} near the center of the column and the vertical stress seems to be a little less near the side walls. (b) Variation of vertical stress with the horizontal coordinate for three different widths, $h = 225$, and $\mu_w = 0.5$. The x-axis of the figure has been scaled to the smallest width $W = 30$ for comparison. Error bars are the standard deviation obtained by running 20 different ensembles at each height.
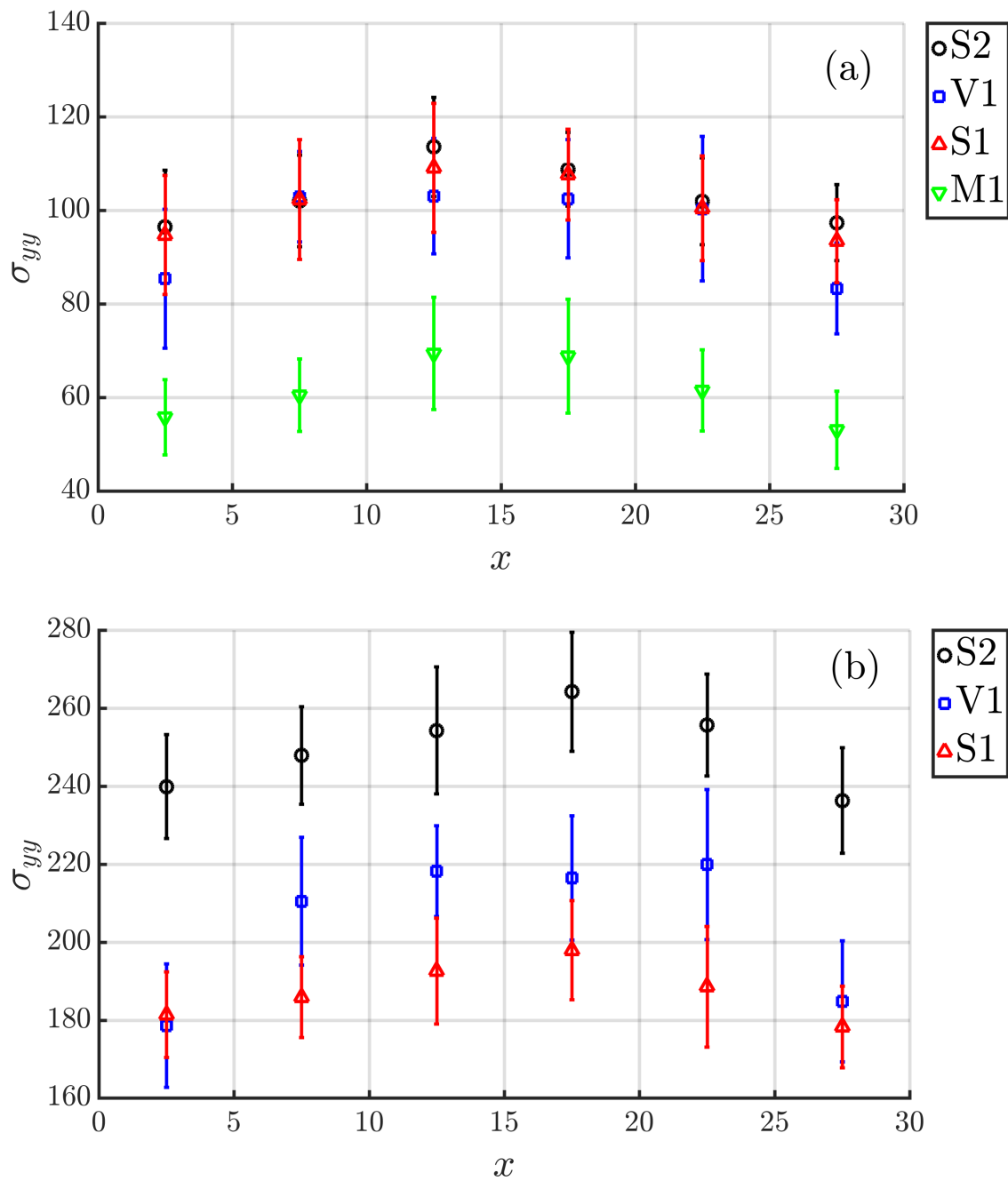
Fig. 5.18 (a) Comparison of vertical stress with the horizontal coordinate for $h = 225$, $W = 30$, and $\mu_w = 0.5$ granular column obtained with four different protocols. All the four protocols seem to show a maximum of vertical stress near the center of the column. (b) This behavior did not change at $h = 450$. Error bars are the standard deviation obtained by running 20 different ensembles at each height.

granular column creates a stress profile, which is very different from the Janssen form. We also observed that tangential forces at the walls are not always at the Coulomb yield limit. In the later part of the chapter, we explained the reason behind the peculiar behavior of stresses in the S1/S2 protocol. The main reason is that σ_{xy} need not be proportional to σ_{yy} and hence a static equilibrium of this kind is permissible. A plausible route was proposed by our argument that the combination of — (i) the impact velocity of the particles, while the packing is being formed and (ii) the heaving process after all the particles have settled — leads to the non-monotonic stress profiles in these two protocols.

In the future, we would like to test these protocols for bidisperse packings. We discussed the S2 protocol $h = 225$ packing with bidisperse spheres in the chapter, where the two diameters used were 1 and 1.2. We did not see any maximum at $h = 225$, but this can be because a lesser number of grains are required to fill height of $h = 225$ compared to a monodisperse packing with particle diameter 1. We would like to see if the maximum appears at larger fill-heights for bidisperse packing.

We would also like to solve equation 5.10 for realistic σ_{xy} profile for S1/S2 protocol. It will be exciting to see if we can estimate the height at which the maximum in the vertical stress profiles occurs in these protocols. For this purpose, we can try to vary the values of elastic constants and the viscoelastic damping constants used in the Hertzian interaction and observe how the location of the maximum changes. It would be interesting to study the variation of these protocols in a three-dimensional column.

Chapter 6

Disordered packing in 2D

We have discussed 2D granular packing and normal collisions between the spheres in a viscous fluid in previous chapters. Normal collisions in a viscous medium are governed by the Stokes number (St). Collision below a critical Stokes number (St_c) leads to completely inelastic collisions of spheres. The structure created by monodisperse spheres after such inelastic collisions at low Stokes number can be quite different from what we analyzed in Chapter 5. In this chapter, we will discuss such packings and their stability.

The goal here is to create a disordered packing by using our understanding from earlier chapters. We will be creating a packing by depositing particles at low Stokes numbers in a viscous medium. Every new particle incident on packing will deliver minimal momentum to the particles beneath. Disturbance of the structure leads to rearrangements and compaction, hence an impact that transfers almost no momentum is expected to lead to loosely-packed structures. We start by proposing a protocol to develop such two-dimensional (2D) disordered packing in the next section. In the succeeding sections, we will try to see how this 2D packing changes with the Stokes number and study overall area-based packing fraction of the structure. We will also discuss the local features of this packing and talk about the stability of the structure when individual particles are added. The collisions between particles in this more natural setting will be both normal and tangential.

6.1 Experimental set-up

To obtain this 2D disordered structure, a rectangular glass container was filled with silicone oil of dynamic viscosity $\mu = 0.0966$ Pa-s and density $\rho_f = 966$ kg/m^3. The silicone oil was obtained from Clearco products (CAS No: 63148-62-9). About 2400 dry stainless steel bearing balls of diameter $d = 1/8^{th}$ of an inch were poured gently into this
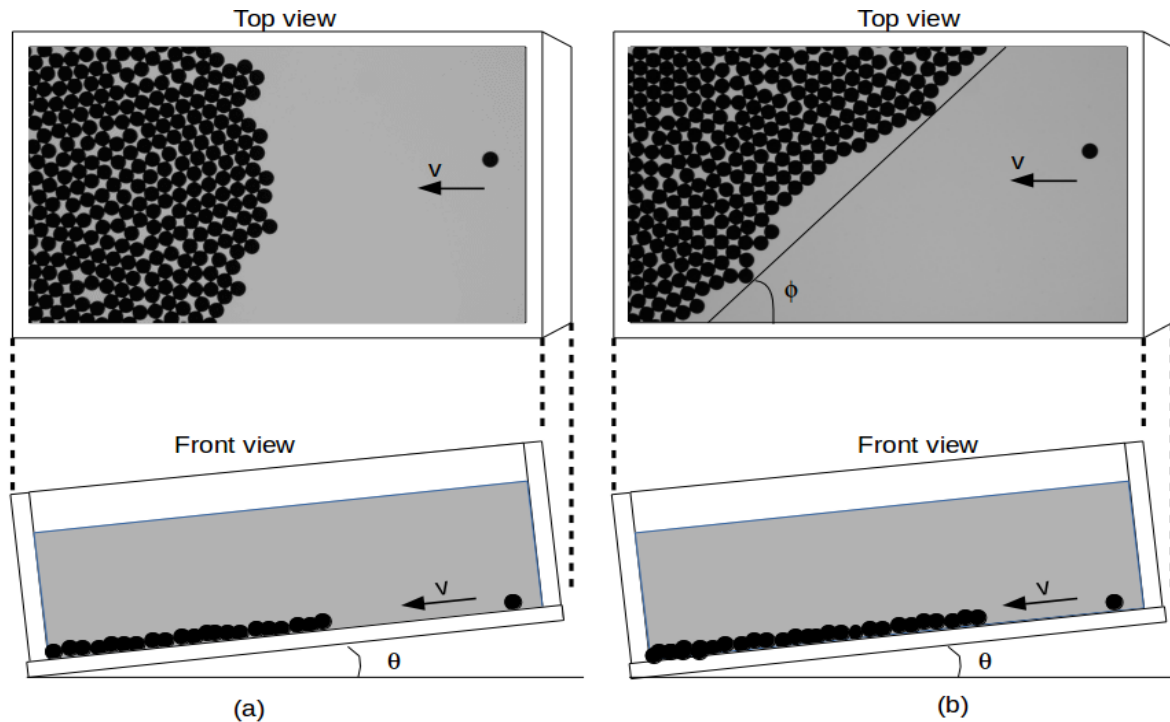
Fig. 6.1 Top and front schematic view of two different types of immersed packing: (a) packing with a horizontal free surface, "parallel packing" and (b) packing with an inclined free surface, "oblique packing". Both packings are generated by different initial conditions. Parallel packing is created by first scattering the particles to occupy the whole space of the container and then lifting one of the short sides of the container to angle θ by using a vertical jack to give the desired packing. For oblique packing, after the initial scattering of the particles, the set-up is tilted length-wise along one side till all the particles roll towards the opposite side. The particles are then allowed to settle in $\theta = 0°$ state before the container is lifted again breadth-wise as in the case of parallel packing to give the oblique packing.

container of cross-section $96.4d$ x $64.25d$ filled with fluid up to $15d$ height. This process introduced many bubbles in the fluid which escaped in a few hours. The glass container was placed over a steel frame one of whose sides was maintained at a constant height. The opposite side was mounted on a vertical jack, which allowed us to vary the elevation of this side and tilt the container along the width as shown in Figure 6.1.

To prepare a packing, the container is placed horizontally and the particles are manually scattered initially such that they remain in a single layer while occupying the whole space of the container. Then, the edge which is mounted on a vertical jack is lifted, without any jerks to the container, until we reach the desired angle. This inclination allows particles to roll towards the opposite side and create a packing. This method

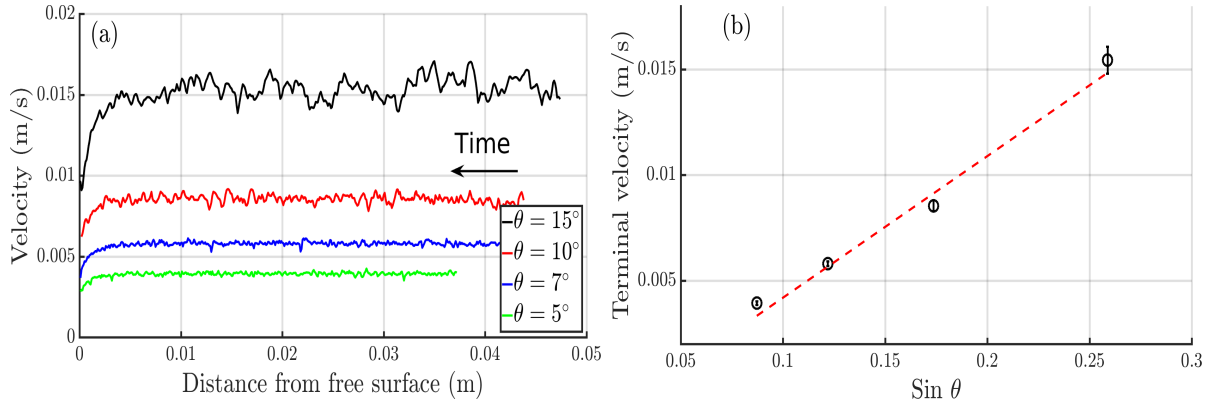Fig. 6.2 (a) Variation of velocity with distance from the free surface for different inclination angle. The data have been obtained by releasing individual wet particles one-by-one from the elevated edge of the container and letting them collide with the free-surface of the packing. Only the region close to the free surface was observed and hence the initial increase in the velocity is not shown. The time is moving forward from right to left of x-axis and 0 in the x-axis refers to the free-surface of the packing. Data were obtained from 10 trials for 5°, 7°, and 10° each, and 2 trials (due to limited data available) for 15°. The average values of the standard deviations of velocities from these trials for 5°, 7°, 10°, and 15° are 0.00028, 0.00032, 0.00075, and 0.0007 respectively. (b) The terminal velocity from (a) has been plotted against Sine of the inclination angle θ. The terminal velocity was extracted by taking the mean of the velocity data for distance > 0.01 m from the free surface as shown in (a). The error bars shown are the standard deviation of this velocity. The terminal velocity increases almost linearly as shown by the red dashed line.

leads to packing with a nearly horizontal free-surface [Figure 6.1 (a)], i.e., the top surface or the free-surface of the packing is practically parallel to the width of the container. We have termed such packings as "parallel packing". We can also create a packing with an inclined free surface by allowing particles to roll towards one of the longer sides of the container first, after being scattered, and then towards the shorter side. These packings with an inclined free surface as shown in Figure 6.1 (b) will be referred to as "oblique packing" and will be discussed in the latter part of the chapter.

We have studied the packing for four different inclination angles $\theta = 5°$, 7°, 10°, and 15°. The inclination angle in the experiment was varied gradually and it takes around 20 seconds to reach from 0° to 15°. A wide LED diffusive light source was placed under the container to increase the contrast, and high-resolution images/videos were taken from above the container using a Nikon D5300 camera. We observed the rolling motion of individual particles down the inclined surface and found that the particles roll in an approximately straight line parallel to the length of the container. To determine the

typical velocity of individual particles before they collide with the packing at different angles of inclination, the particles were released from the elevated edge of the container to roll downhill. The motion of the particles was tracked by the camera at 60 frames per second and 1920 x 1080 resolution. As discussed in Chapter 4, "Analyze particle" feature of ImageJ was used to determine the centers of these particles and finite difference scheme was used on this data to get velocity.

The velocity as a function of the length traveled is shown in Figure 6.2 (a) and (b) and we focus only on the data close to the free surface. All the individual particles reach terminal velocity before colliding with the packing as shown in Figure 6.2 (a). Also, notice the rapid decrease in the velocity before impact with the packing. This is due to the lubrication forces as discussed in Chapter 2-4. The terminal velocity, as shown in Figure 6.2 (b), is practically a linear function of Sin θ. This is expected as the force on the particles is a function of Sin θ. Small deviations from linearity might be due to the fact that the frictional force on the particle depends on Cos θ. The terminal velocity at different angles of inclination acts as the upper bound of impact velocity for that packing, as some collisions can happen at smaller velocities too during the initial formation of the packing. These terminal velocities are used to assign a Stokes number to packings created at different inclination angles, as shown in Table 6.1.

θ	St
15°	0.427 ± 0.019
10°	0.237 ± 0.007
7°	0.161 ± 0.003
5°	0.109 ± 0.003

Table 6.1 Stokes number (St) values for different angles of inclination (θ). Stokes number is calculated by using the diameter of the particle d and the terminal velocity obtained from Figure 6.2 (b). The error in the Stokes number is considered to be solely from the terminal velocity calculation [see the error bars in Figure 6.2 (b)].

The particle is believed to be rolling over a thin film of fluid above the bottom surface of the container. These particles seldom get stuck at the surface of the container at $\theta \geq 10°$. But at smaller angles ($\theta \leq 5°$) some particles can get stuck at the surface, suggesting that the slope is nearing the rolling friction coefficient limit. For this reason, we decided to limit our experiments to $\theta \geq 5°$. The dimension of the container fixes the upper limit on θ. It was fixed at 15° to keep the oil from spilling from the side of the lower elevation and still have the elevated side of the container immersed. The effect of single-particle collisions with "parallel" and "oblique" packing will be further discussed in the last part of the chapter.
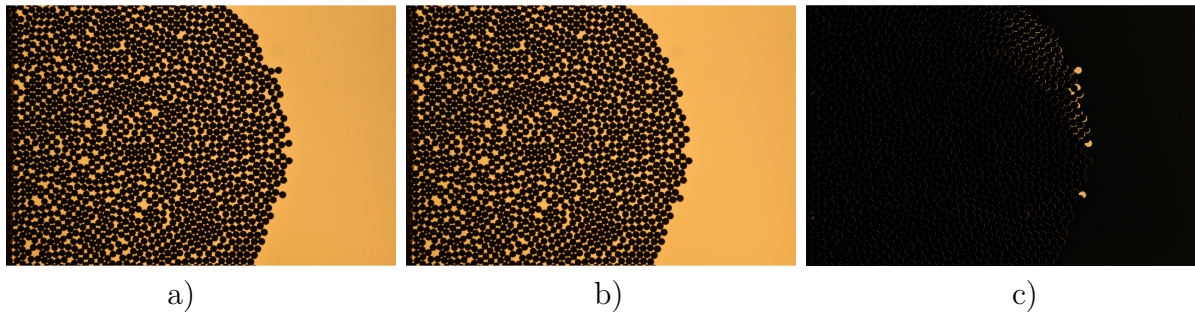
Fig. 6.3 A sample parallel packing image at 15° angle of inclination. (a) Shows the parallel packing just after all the particles have settled and can be considered as the packing at time = 0. (b) Shows the packing after 2 hours from (a). Notice some minor rearrangement at the free surface. To observe these rearrangements image (b) is subtracted from the image (a) and the net result is shown in (c). The black region means the subtraction returned zero and suggest that there was no difference in (a) and (b) far away from the free surface. The yellow color in (c) suggest that there were some minor rearrangements near the free surface.

Though there was no visible motion after a few seconds of the formation of the parallel packing, we waited for five minutes before capturing the images. The images were captured using Camera Control Pro software with a resolution of 6000 x 4000 pixels^2. All the image analysis and data processing discussed from now onward were carried out in MATLAB. A sample image of the parallel packing at 15° angle of inclination just after all the particles have settled and the packing is formed is shown in Figure 6.3 (a). Figure 6.3 (b) shows the image of the same packing after 2 hours. As can be seen, there is no visible difference in the packing in the two time frames, other than rearrangements of few particles at the free surface.

To determine the extent of this rearrangement, we subtracted Figure 6.3 (a) from Figure 6.3 (b) by using "imsubtract" feature in MATLAB and obtained Figure 6.3 (c). Any image is just an array of integers and can be subtracted like this. The subtracted array is truncated by the software to fall in the range of the integer type of the input images. The dark region in Figure 6.3 (c) represents zero intensity and suggest that Figure 6.3 (a) and Figure 6.3 (b) are identical far away from the free surface. The bright region, the color of the background, suggests that there are some small rearrangements near the free surface in the 2 hour time. These could have been caused by some jerks to the experimental set-up from external sources.

We found that five minutes are enough for such rearrangements and we waited only for five minutes because these rearrangements at the free surface do not affect the packing
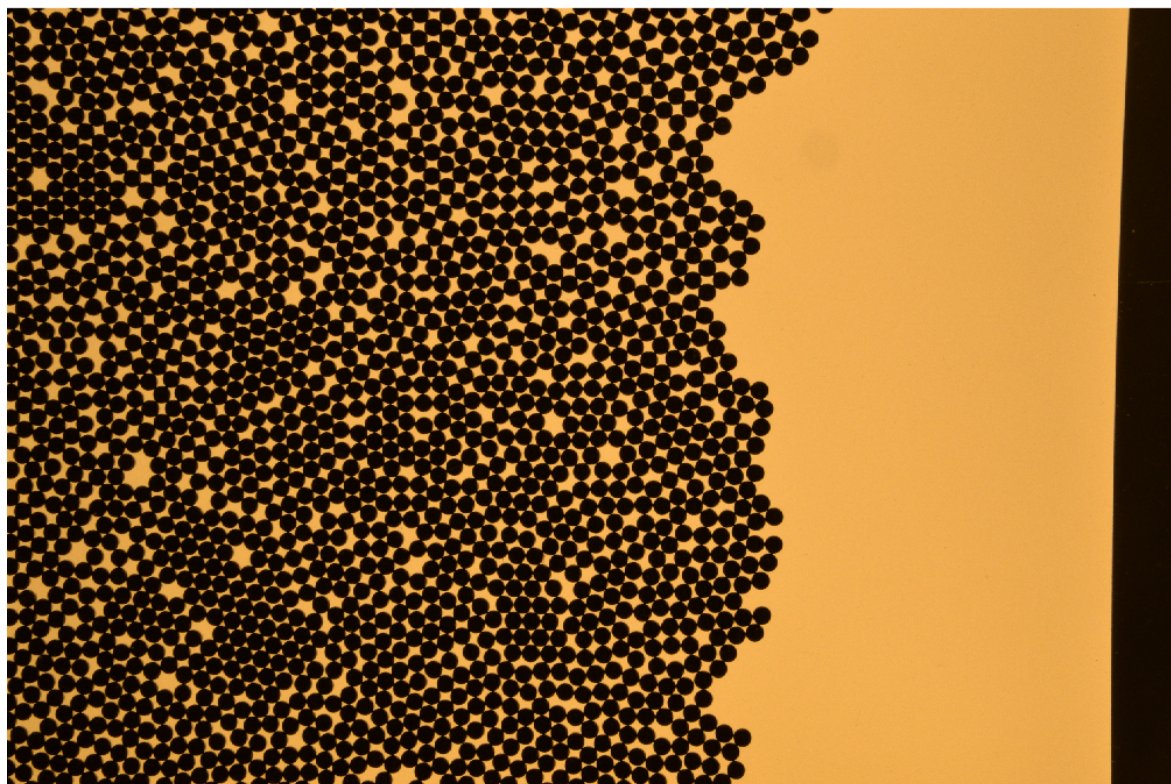
Fig. 6.4 A sample parallel packing image at 10° angle of inclination. It took approximately 15 seconds to lift the container using a vertical jack and reach from 0° to 10°. After that, we waited for all the particles to roll down and for unstable structures to collapse and give us the final stable packing.

in the interior. This shows us that the packing under observation is mechanically stable. Similar features were observed for packings created at smaller angles of inclination. Another sample image at 10° angle of inclination five minutes after the settling of the particles has been shown in Figure 6.4. Notice the disordered structure in the packing.

6.2 Radius determination

The images obtained by the camera after five minutes of the creation of the packing are thereafter analyzed to find centers and radius of individual particles using the "imfindcircles" feature in MATLAB, which uses the circular Hough transform (CHT) based algorithm to find circles. The method takes a gradient of the image and identifies the pixels with high-gradient as the edge. The pixels on this edge are termed as "candidate pixels" and are used as the centers to create circles of different radii. The point at which

most of these new circles of a fixed radius intersect is the actual center of the particle and the radius at which this happens is the best radius estimate of the particles.

The Hough transform method heavily relies on its first step, i.e., detection of edge pixels. However, a hard particle in contact with other hard particles at different orientations can hinder the accuracy of edge detection. We found that the algorithm often underestimates the radius as shown in Figure 6.5 (a) and (b) and also introduces a slight offset in the centers. The offset could be caused by the presence of the contacts or due to the lighting or imaging feature of the set-up. A little asymmetry in lighting or imaging can cause the image to have some reflection of background light from the surface of the sphere in a particular direction. The blue circles in Figure 6.5 show the circles detected by the circular Hough transform and black disks are the actual particles. Figure 6.5 (a) shows the detection at an instant when the particles have been manually scattered to occupy the complete space of the container and the container is placed parallel to the ground, whereas Figure 6.5 (b) shows the detection via CHT for a packing at 10° angle of inclination. The blue circles are not always touching where the contacts are present as shown in Figure 6.5 and hence the CHT algorithm underestimates the radius of the particles. This error in radius and offset in the centers is not more than 4 percent but becomes important if one is calculating area-based packing fraction for a region with 1500-2000 particles.

(a)   (b)
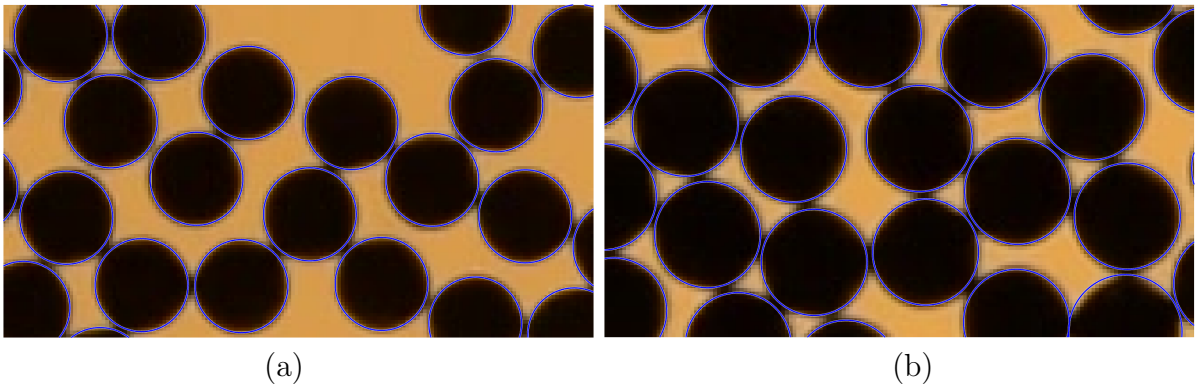
Fig. 6.5 Particles detected by the circular Hough transform (CHT) algorithm (a) after manually scattering the particles to occupy the whole space of the container at 0° angle of inclination and (b) after the formation of the packing at 10° angle of inclination. The black objects are the particles and the blue circles are obtained by CHT. As can be seen, CHT (blue circles) underestimates the radii of the particles and is therefore unable to detect all the contacts.

In general, determining contact between hard particles requires very high precision in the determination of the center as well as radius. To avoid this underestimation

of radius, we devised a new method to determine the radius. In each trial, we first detected individual particle radii by CHT and then took the mean over all the particles in the packing. Now, each particle is considered to have this mean radius, R_{Hough}. The average and standard deviation of these mean radii (R_{Hough}) over different trials at each inclination angle are shown in column 2 and 3 respectively of Table 6.2. In each trial, the radius of every particle is then increased from R_{Hough} in steps of 0.1 pixels until we detect at least one particle with six contacts, representing a hexagonal crystalline structure. A contact is established when the distance between the centers of any two particles is less than or equal to the sum of the radii of the two particles. At this point, a new radius is obtained by taking the mean center-to-center distance between the middle particle in the hexagonal structure and the six contact particles and then dividing the mean by 2.

The average of this new radius, (R_{hex}), over different trials is shown in column 3 of Table 6.2. The advantage of this method for determining the radius is that this is a local measurement, and it helps in canceling some biasing in the center-determination of CHT. Such particles with six contacts were present, though rare, at all the angles of inclination studied. However, the occurrence became even rarer as we decreased the angle. In some trials, there were actually no particles with six contacts in the packing and there were some particles with five contacts and one particle just by 1 pixel or so away from being the sixth contact. Hence in such trials where there were no particles present with six contacts, this method might have lead to overestimation of the radius.

θ	Average R_{Hough}	Average error in R_{Hough}	Average R_{hex}	Average R_3
15°	42.6	0.77	42.63	44.7
10°	45.12	0.74	46.22	47.79
7°	48.88	0.90	50.69	51.93
5°	46.7	0.84	48.95	49.99

Table 6.2 Radius in pixels obtained by different methods for different angles of inclination (θ). R_{Hough} is the mean of the individual radii obtained by the circular Hough transform in each trial at a particular angle of inclination. Error has been taken as the standard deviation at each trial. R_{hex} is the radius of the particle at which the first occurrence of any particle with six contacts is observed in the packing. R_3 is the radius of the particle at which the coordination number of the packing = 3. Averages over different trials at each inclination angle are shown.

To determine if this method overestimates the radius, we measured the average coordination number of the packing. The average coordination number is defined as the average number of contacts each particle has in the packing. We found that the average coordination number of the packing for all the angles of inclination at their particular

R_{hex} is less than 3, the lower limit of the average contacts necessary in a 2D frictional system (Andreotti et al., 2013). This is shown in Figure 6.6 where the x-axis has been normalized by R_{hex}. This suggests that R_{hex} is not an overestimation of the radius of the particle, but in fact, might still be an underestimation. The figure shows the increase in coordination number with the increase in radii of the particle, $R_{hex}(1 + \Delta)$, where Δ is increasing in steps of 0.02 from -0.06 to 0.24. We refer to the radius at which the average coordination number of the packing is 3 as R_3. This radius is shown in column 4 of Table 6.2 and is 1-2 pixels larger than R_{hex}. This radius gives a good ensemble-averaged lower bound on the radius of the particle. However, it ends up imposing an average coordination number, by assumption, on all the packings. Thus, even if packings are different, by construction they all have the same coordination.
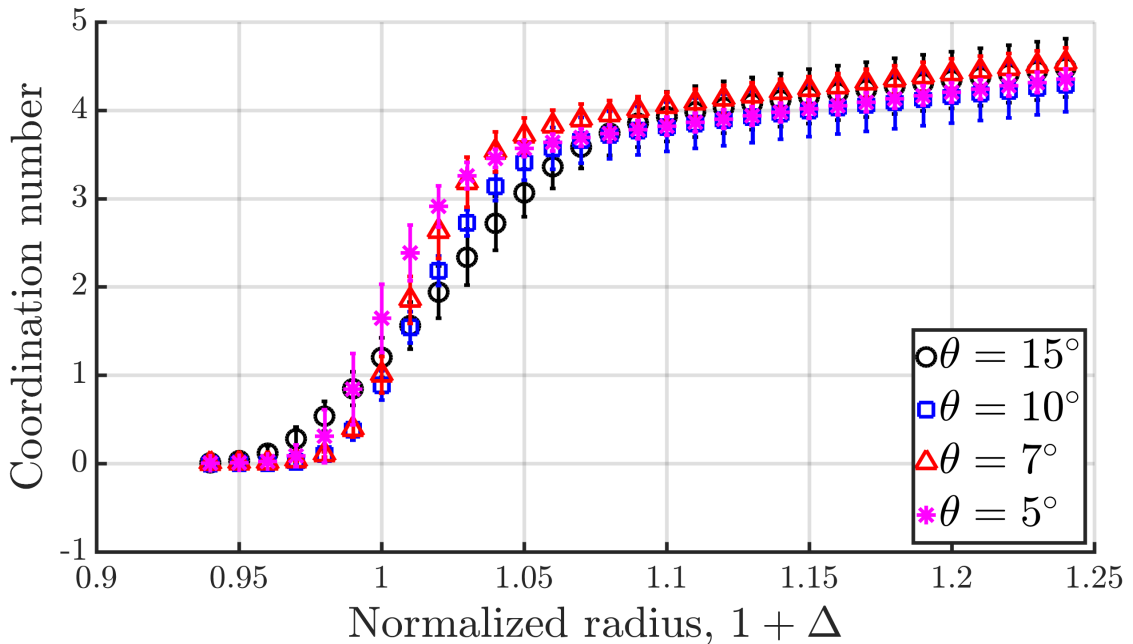
Fig. 6.6 Variation of average coordination number of the parallel packing with small fractional change (Δ) in the radius of the particle from R_{hex} for four different inclination angles. The radius of the particles has been normalized by R_{hex}. The error bars are the standard deviations of different trials at fixed angles of inclination. Notice that the coordination number is less than three for all the inclination angles at normalized radius = 1 or radius = R_{hex}.

6.3   Global Packing

Hence, all the above-mentioned approaches (R_{Hough}, R_{hex}, and R_3) to determine the radius of the particles have some advantages and some disadvantages. These different radii are used to calculate the area-based packing fraction at different inclination angles, as shown in Figure 6.7. Packing fraction is the ratio of the total area of all the particles to the total area of the boundary which envelops all the particles. This boundary area is determined by using the "boundary" feature in MATLAB. This feature creates a compact boundary around the outer-most particles and provides the area inside this boundary. The packing fraction calculated by an intermediate radius R_2 is also shown in the figure for completeness. R_2 is the radius at which the mean coordination number of the packing is two. The packing fraction for parallel packing seems to decrease with the decrement of the angle of inclination as we go above R_{hex}. This result is intuitive as one would expect the load on spheres, away from the free surface, to be less at lower inclination angles. Therefore, the random structures created at lower angles are loosely packed and are still stable.
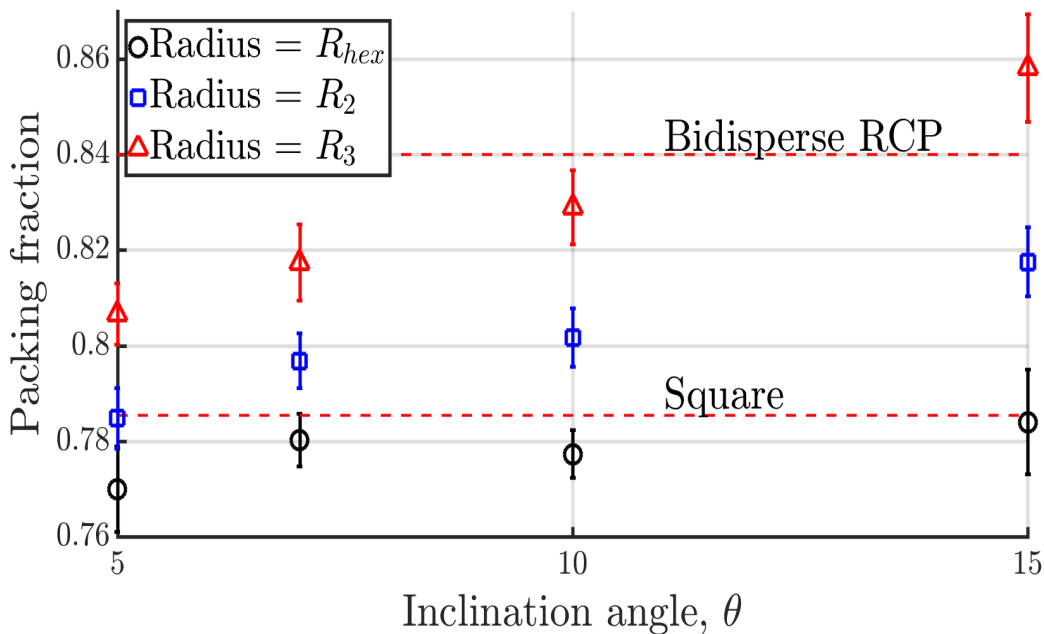
Fig. 6.7 Area-based packing fraction for four different inclination angles. Packing fraction is calculated by using three different definitions of particle radius: R_{hex}, R_2, and R_3. The dashed lines in red at $\pi/4$ and at 0.84 represent packing fraction for the square lattice, and bidisperse random close packing in 2D respectively. The error bars are the standard deviation of 9, 4, 16 and 20 trials at 5°, 7°, 10°, and 15° angle of inclination respectively.

To determine the orientational order in contacts in the packing, we measured the bond orientational order parameter ψ_4 and ψ_6 (Steinhardt et al., 1983) for all the particles. As the name suggests, ψ_4 and ψ_6 are measures of orientational symmetry amongst neighbors of a given particle and are used to quantify the degree of crystallinity present in a system. A particle will be deemed to be a neighbor of another particle if the distance between the two is less than R_3. For an ith particle, ψ_4 and ψ_6 are defined as:

$$\psi_{4_i} = \left| \frac{1}{N_b} \sum_{m=1}^{N_b} e^{4i\phi_{mi}} \right|; \tag{6.1}$$

$$\psi_{6_i} = \left| \frac{1}{N_b} \sum_{m=1}^{N_b} e^{6i\phi_{mi}} \right|, \tag{6.2}$$

where N_b is the number of neighbors and ϕ_{mi} is the angle between the x-axis and the line joining the ith particle with its mth neighbor. For a square lattice in 2D, ψ_4 will be 1 and for a hexagonal lattice in 2D ψ_6 will be 1. Both ψ_4 and ψ_6 will be small if the packing is completely random and has no orientational order.

After obtaining ψ_4 and ψ_6 for all the particles, we plotted a normalized histogram (probability distribution) at different inclination angles as shown in Figure 6.8. The probability of ψ_4 lying below 0.5 value is higher for all inclination angles, suggesting that there are very few square lattice-like structures, and the packing lacks ψ_4 orientational order. But in the ψ_6 distribution, the probability increases with the ψ_6 value and becomes maximum at 1, suggesting that there are patches of hexagonal ordering in this disordered packing. This does not necessarily mean that there are regions with hexagonal crystalline packing as ψ_6 can be 1 for a particle having less than six contacts or having vacancies if the contacts are oriented along the hexagonal axes.

To determine how the disorder changes with the inclination angle, we analyzed the Voronoi diagrams of the parallel packings, obtained by using "voronoi" package in MATLAB, as shown in Figure 6.9. A Voronoi diagram made from n generating points divides the plane into regions such that there is exactly one of the nth generating points for each region and each point inside this region is closest to its generating point than any other generating points. This diagram is created by drawing equidistant lines between two generating points. In our case, centers of the spheres will act as generating points.

To understand the Voronoi diagram, we measured the areas of the polygons and created a probability distribution of the areas. The distributions for four different inclination angles are shown in Figure 6.10. The x-axis of the figure has been normalized by the area of a regular hexagon inscribing a particle of radius R_3, in a hexagonal crystalline packing. The probability distribution of the area of Voronoi polygons for all

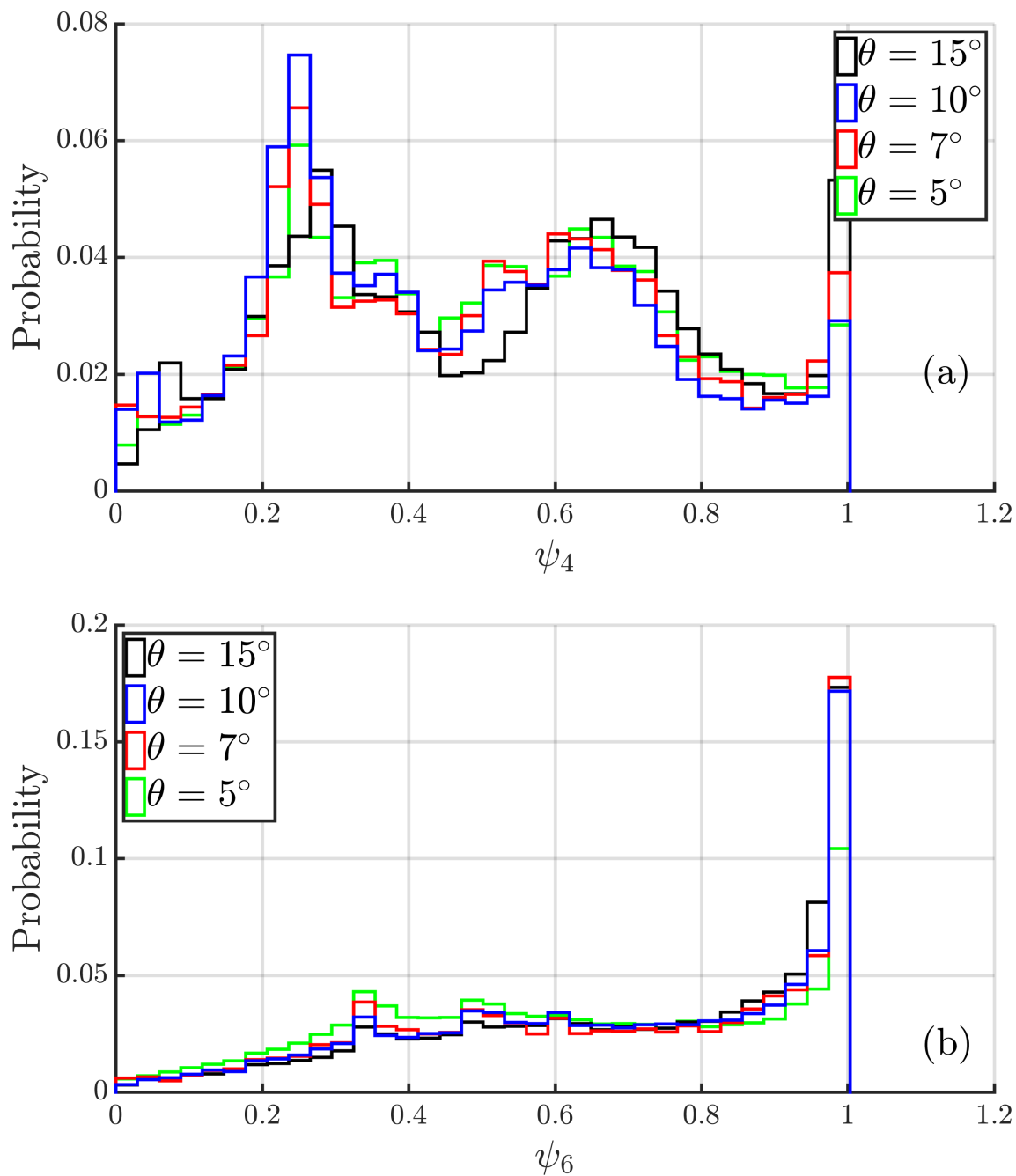Fig. 6.8 Probability distribution of bond orientational order parameter (a) ψ_4 and (b) ψ_6 for four different inclination angles. A small value on the x-axis indicates a disordered state and a large value represents crystalline order.
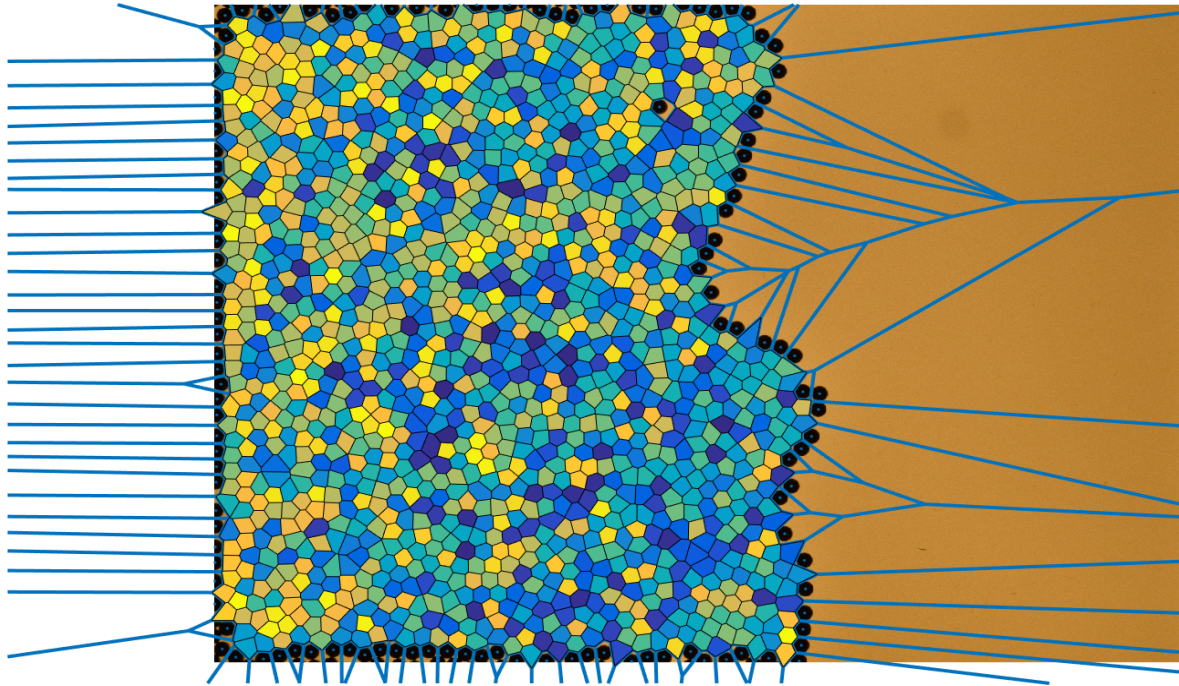
Fig. 6.9 A sample figure showing the Voronoi diagram for a parallel packing. The blue lines outside the colored tessellations show that the Voronoi polygons are not closed for particles at the boundaries of the packing (marked in black). We exclude these from the subsequent analysis. To get the estimate of the polygon areas in the bulk we are ignoring the polygons created by the boundary particles. The colors in the polygons are used just to distinguish different polygons.

the four angles of inclination follow the same behavior. The distribution rises sharply to a peak at a value greater than one and then decays exponentially and eventually gets cut-off at some large value of the normalized area. The presence of peaks near the unit value of the normalized area, for all the inclination angles, suggests that all the packings are dominated by hexagonal ordering, similar to our observation from Figure 6.8.

The distribution tells us that the particles are more compactly packed at a larger inclination angle as the peak in the distribution for larger inclination angle, $\theta = 15°$, comes at a smaller value of the area. This is expected since particles have to carry more load at a larger angle of inclination. The area for a square inscribing a particle of radius R_3 is 1.155. A large probability for an area bigger than 1.2 means that the packing has many defects or empty regions. The probability of having large polygon area is smallest for $\theta = 15°$ and hence big defects are lesser at a larger angle of inclination. The cut-off comes at a very large value of the normalized area, more than 1.4 for all
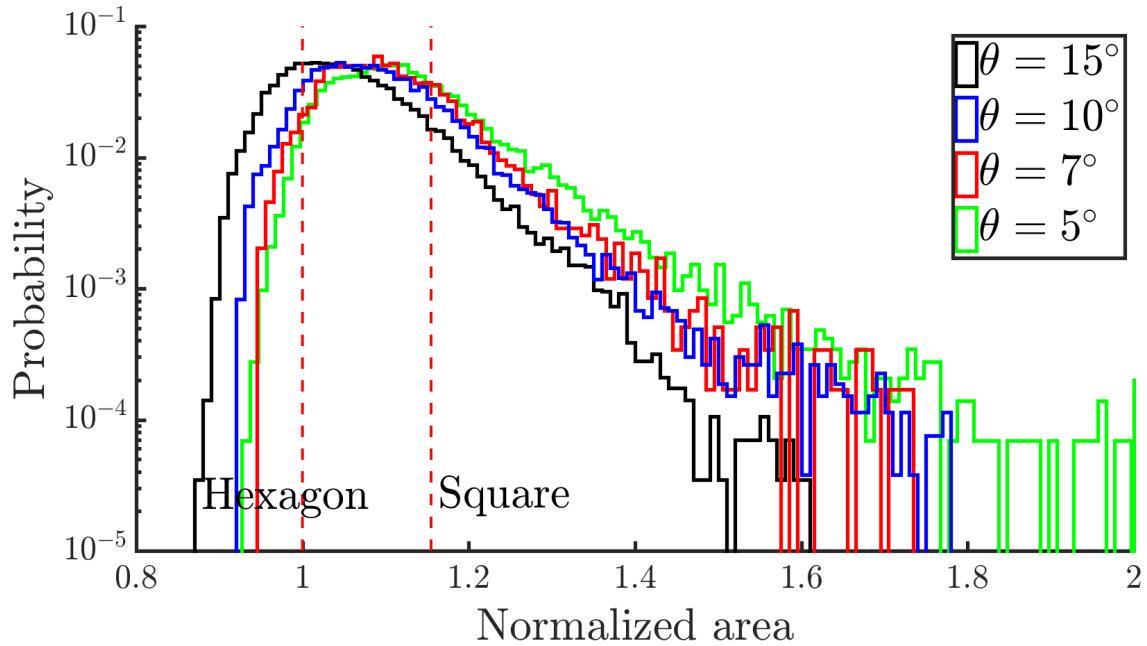
Fig. 6.10 Log-linear plot of the probability distribution of the Voronoi polygon areas for four different inclination angles. The x-axis has been normalized by the area of a regular hexagon inscribing a particle of radius R_3. The vertical dashed line at normalized area of 1 represent this area. The vertical line at $2/\sqrt{3}$ represents the normalized area for a square inscribing the same particle.

angles, suggesting that these empty regions can be large sometimes. These empty regions increase in size and quantity with decreasing θ.

6.4   Spatial variation in packing

We now ask the question of how these packings change as a function of distance from the free surface of the packing. Are the regions away from the free surface more crystalline as they carry more load? To answer these questions, we coarse-grained the packing into $5d$ x $5d$ square boxes and found the particles inside these boxes. If the center of a particle was found to lie inside the box, then the particle was considered to be inside the box. The center of the particle was found by circular Hough transform as discussed in the previous section. After finding all the particles inside a box, a compact border was drawn around the outer-most particles in each box using the "boundary" feature in MATLAB. This border envelops all the particles in the square box as shown by green lines in Figure 6.11. The area of the particles is determined by using R_3 as the radius. Using the
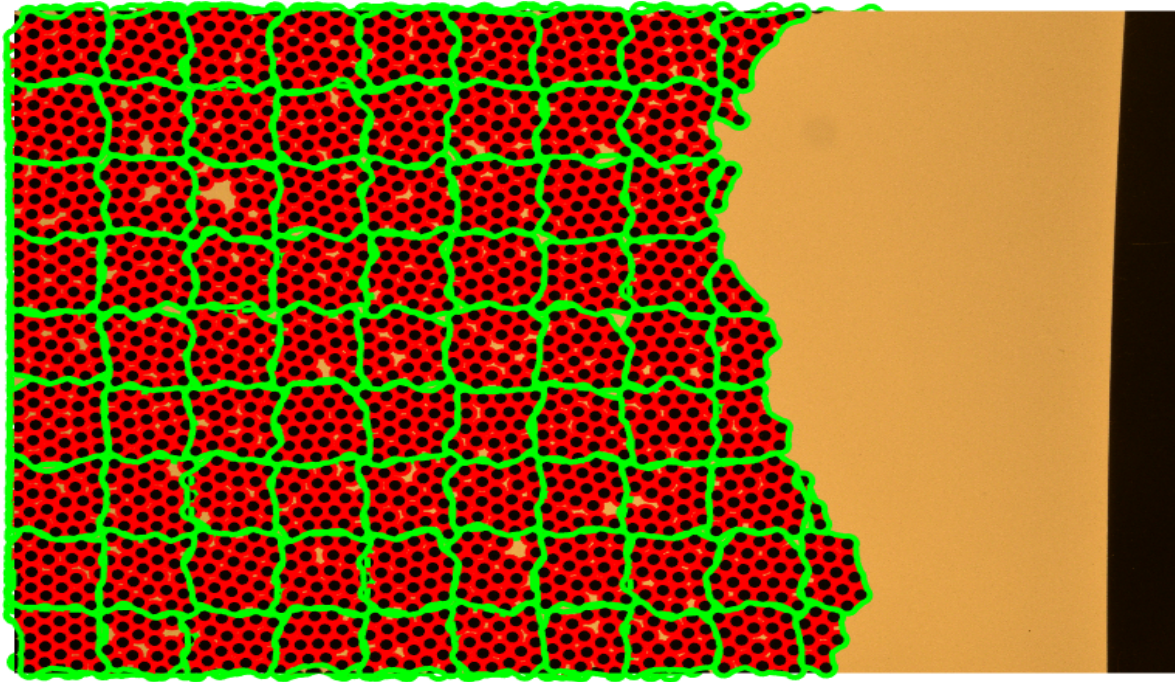
Fig. 6.11 An example of the coarse-graining in parallel packing. The packing is divided into 5d x 5d square boxes and the centers of all the particles are checked to determine the particles that lie inside the box. Once the particles inside the given box are known, a tight outer boundary is created around the particles as shown by green lines in the figure.

area occupied by the particles and the area of this border, the packing fraction for each box is determined. Note that this border was just created to determine the area-based packing fraction and the square box is still our primary coarse-grained structure, whose center is used to study the spatial variation in the packing fraction.

After determining the packing fraction in each box, we averaged the packing fraction ϕ across the width of the container and then studied the variation of ϕ with the distance from the free surface of the packing as shown in Figure 6.12. The x-axis in the plot shows distance from the free surface in units of d and the zero on the x-axis represents the free surface. As we move away from the free surface, we see an increase in the packing fraction for some distance. This is expected as the load on the particles will increase as we move away from the free surface of the packing, which can lead to more compact structures. This increase is more prominent at larger angles like $\theta = 15°$. This is the consequence of the fact that as the angle of inclination increases, the load on the particles away from the free surface also increases.

In any individual trial, the free surface was never perfectly parallel to the width of the container. This lead to fewer particles inside the boxes used for coarse-graining, near
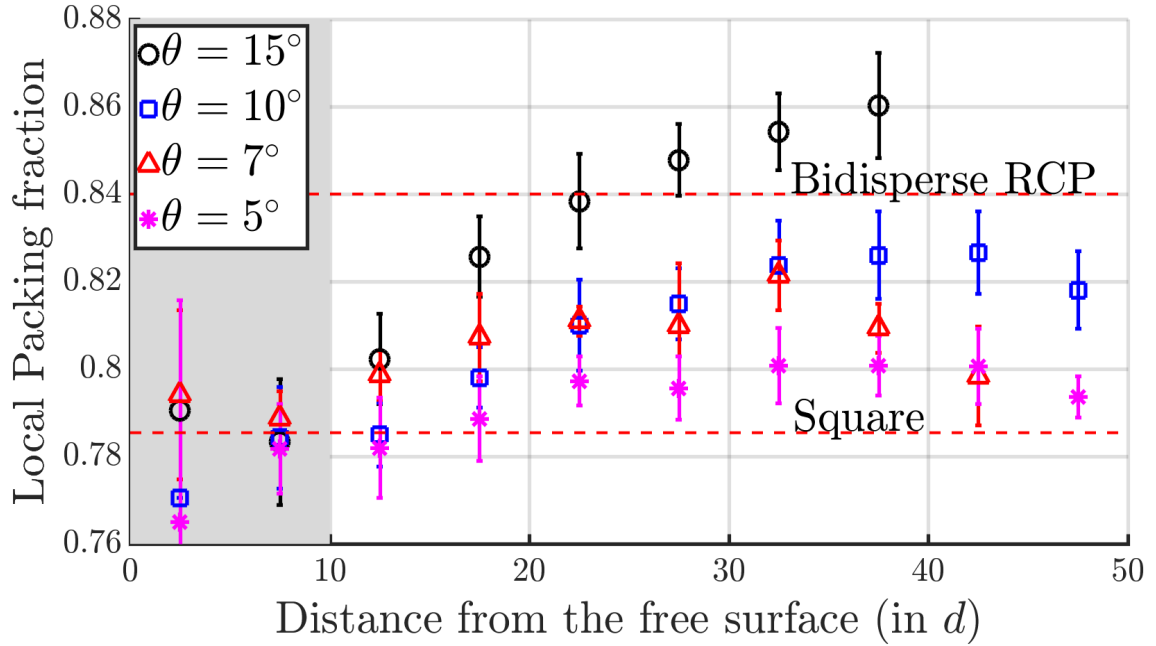
Fig. 6.12 Variation of area-based packing fraction with the distance from the free surface of the packing for four different angles of inclination θ. The packing fraction was obtained for each coarse-grained square box (Figure 6.11) and averaged across the width to study the length-wise variation. Packing fraction increases as one moves away from the free surface through most of the depth. Error bars are the standard deviations of packing densities measured from different trials at a fixed inclination angle. The two horizontal red-dashed lines at packing fraction $\pi/4$ and 0.84 represents square lattice and bidisperse random close packing in 2D respectively. Values near the free surface (distance $< 10d$) have big deviations due to poor sample size and this region has been shown in grey color.

the free surface as is evident from Figure 6.11. This region is shown in grey color in Figure 6.12 and Figure 6.13 and has big error bars due to the limited sample size. For all the angles, the packing fraction shows a tendency to saturate at large distances from the free surface. This trend is not completely clear as the height of the packing is not much larger than the width. It seems that this saturating value of packing fraction might be different for different angles of inclination.

Similar plots can be obtained for variation of the ψ_4 and ψ_6 orientational order with the distance from the free surface of the packing as shown in Figure 6.13 (a) and (b). For all the angles of inclination, the ψ_4 order seems to decrease as we move away from the free surface before saturating, whereas the ψ_6 values do not change much within the error bars. In our discussion about the probability distribution of the ψ_6 and the ψ_4
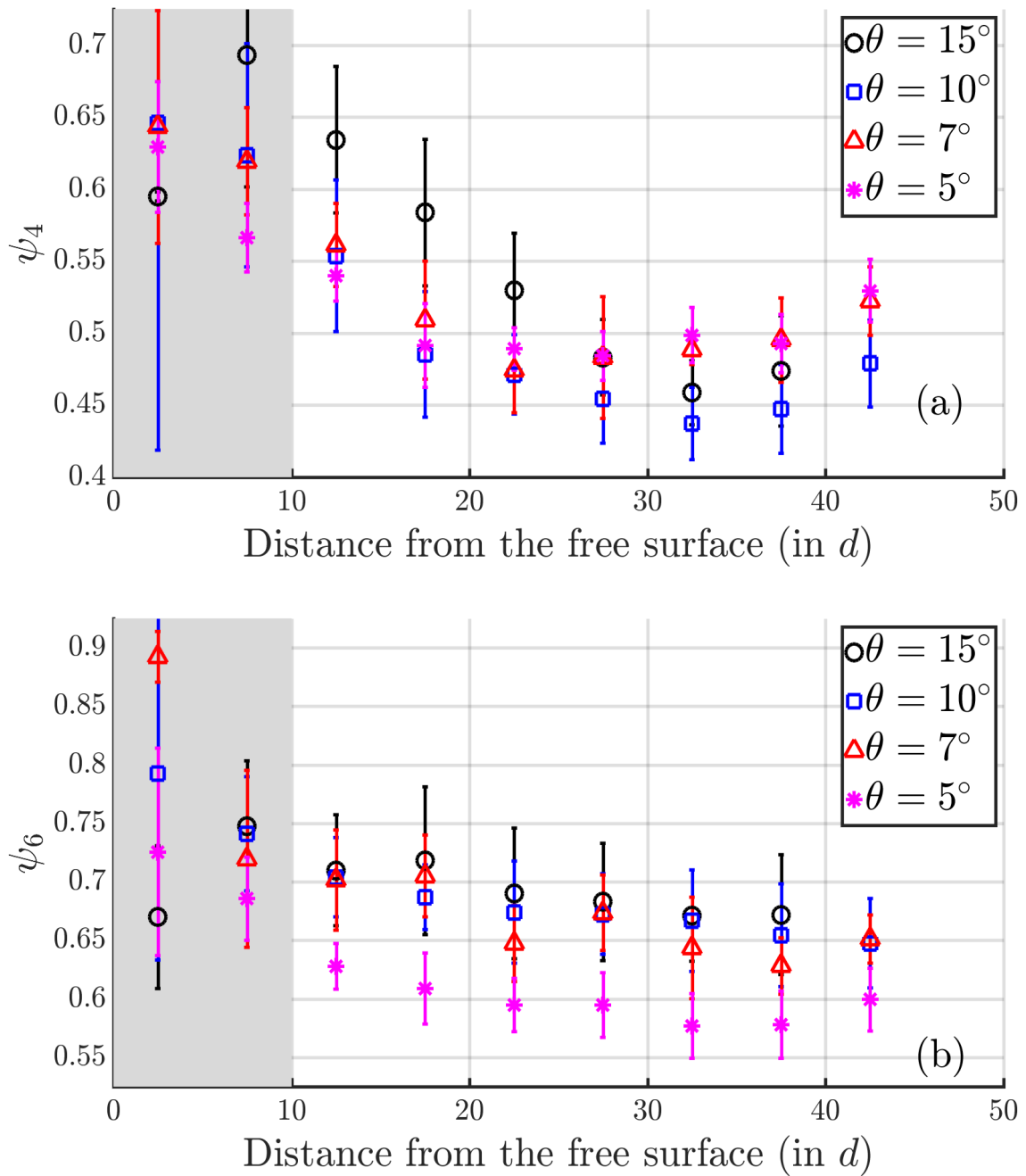
Fig. 6.13 Variation of bond orientational order (a) ψ_4 and (b) ψ_6 with the distance from the free surface of the packing at different angles of inclination θ. The ψ_4 orientational order seems to decrease as we go away from the free surface of the packing for all angles before saturating. The ψ_6 order remains almost constant within the error bars. Error bars are the standard deviations of ψ_4 and ψ_6 measured from different trials at a fixed inclination angle. Values near the free surface (distance $< 10d$) have big deviations due to poor sample size and this region has been shown in grey color.

orientational order in the previous section, we saw that the ψ_6 order is more probable. Figure 6.13 (a) and (b) gives the same idea as the y-axis values in (b) are larger than values in (a) at a particular distance from the free surface.

Figure 6.13 (a) and (b) suggest that as we move away from the free surface, the packing starts losing its ψ_4 orientational ordering and only the more preferred ψ_6 ordering remains. The ψ_6 orientation order for the smallest angle of inclination studied ($\theta = 5°$) was found to be lowest suggesting that packings created at a lower angle of inclination are more disordered. Large error bars near the free surface are due to poor sample size as discussed above.

6.5   Individual particle packing

The packings discussed previously are created by collective sedimentation. Hereafter, we rolled particles one-by-one onto such a packing to understand the stability of the packing under collisions. Figure 6.14 shows an example of a particle being rolled downhill to collide with an oblique packing. Three scenarios are possible in this situation. First, the particle rolling downhill (let's call it A) impacts another particle (let's call it B) of the packing. Particle A rolls over the particle B to settle in the next minimum.

In the second scenario, particle A rolling over particle B does not stop at particle B's side but keeps rolling over another particle (say C) that is in contact with particle B. Now, particle A can settle on particle C's side or can keep rolling further and settle next to some other particle or reach to the bottom of the oblique packing by rolling over the particles. In the third scenario — which is quite rare — particle A impacting the free surface of a delicately packed inclined pile can start an avalanche. We rolled 164 individual particles one-by-one on two different oblique packings at 15° inclination angle and found that approximate probability of first, second and third scenario occurrence is 16.5%, 78.6%, and 4.9% respectively.

The whole process of particles rolling downhill and impacting the packing was recorded in videos at 60 fps, 1920 x 1080 resolution. The recorded videos were then converted into individual frames for analysis. The second and third scenarios discussed above have been shown for the 15° angle of inclination in Figure 6.15. Figure 6.15 was created by subtracting the nth frame from $(n + m)^{th}$ frame, where m is referred to as the frame gap in the figure. The subtraction was done in the same way as in Figure 6.3. The resultant figure was converted into a binary image and the area of the bright region was calculated by using the "bwarea" feature in MATLAB. This area is referred to as the
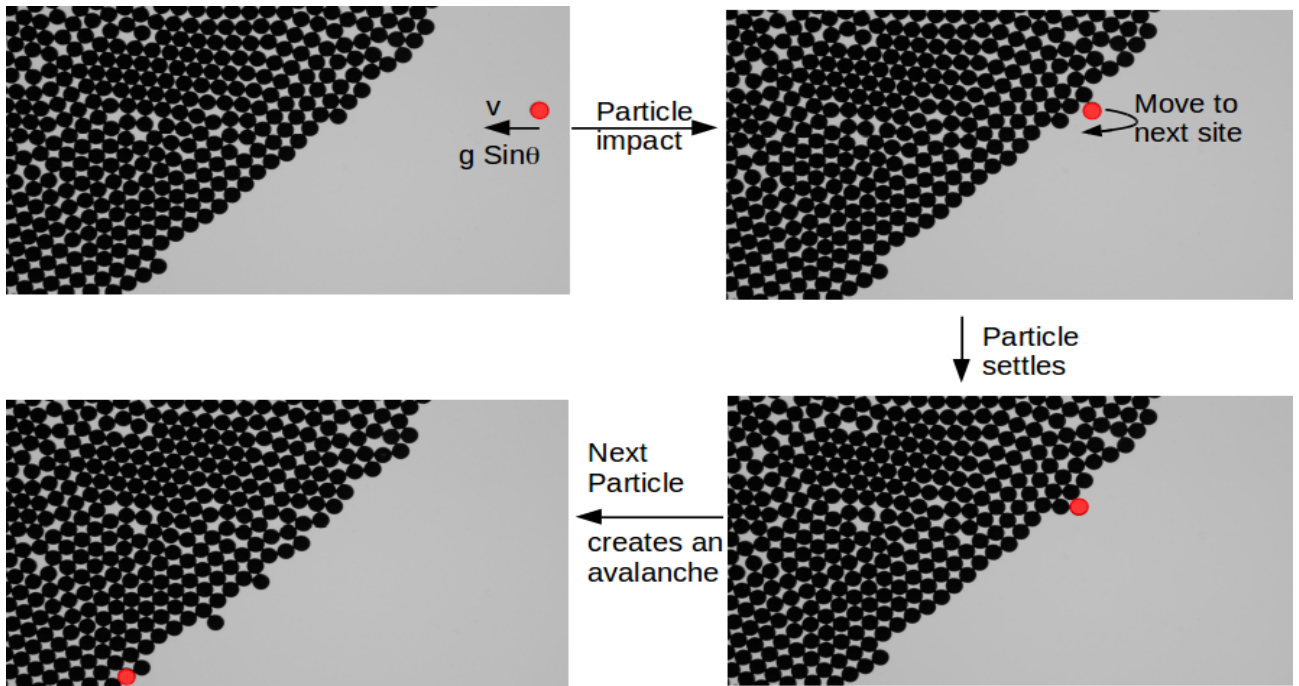
Fig. 6.14 The effect of individual spheres colliding with the packing. The figure shows the top view of an oblique packing as shown in Figure 6.1 (b). Individual spheres (shown by the red circle) are rolled downhill to collide with this packing. Three scenarios are possible: 1.) First, the red particle rolling downhill impacts another particle in the packing, rolls over this particle, and settles in the first groove (minimum), it encounters, between two particles. 2.) The red particle after impacting and rolling over the first particle does not settle in the first groove but keeps on rolling over one particle after another, thus going downhill using the inclined free surface. In the bottom right figure, the red particle has rolled over two particles, after impacting, before finally stopping. Figure 6.15 top panel depicts this scenario. 3.) The red particle after impacting the packing starts an avalanche changing the whole oblique packing structure.

"disturbance area" in Figure 6.15 and quantifies the dissimilarity between two separate frames corresponding to the changes in the packing caused by individual impacts.

Figure 6.15 (a) shows the second scenario in which a particle is rolling over other particles. It almost comes to rest when it reaches the grooves between two particles and the velocity is minimum when it is in contact with both the particles in the gap. Hence, the area between the two separated frames is also a minimum in this region. Such events are shown by the minima in the plot. The maxima in the plot indicate the moments when the tangent plane at the contact point of the rolling particle is parallel to the length of the container.
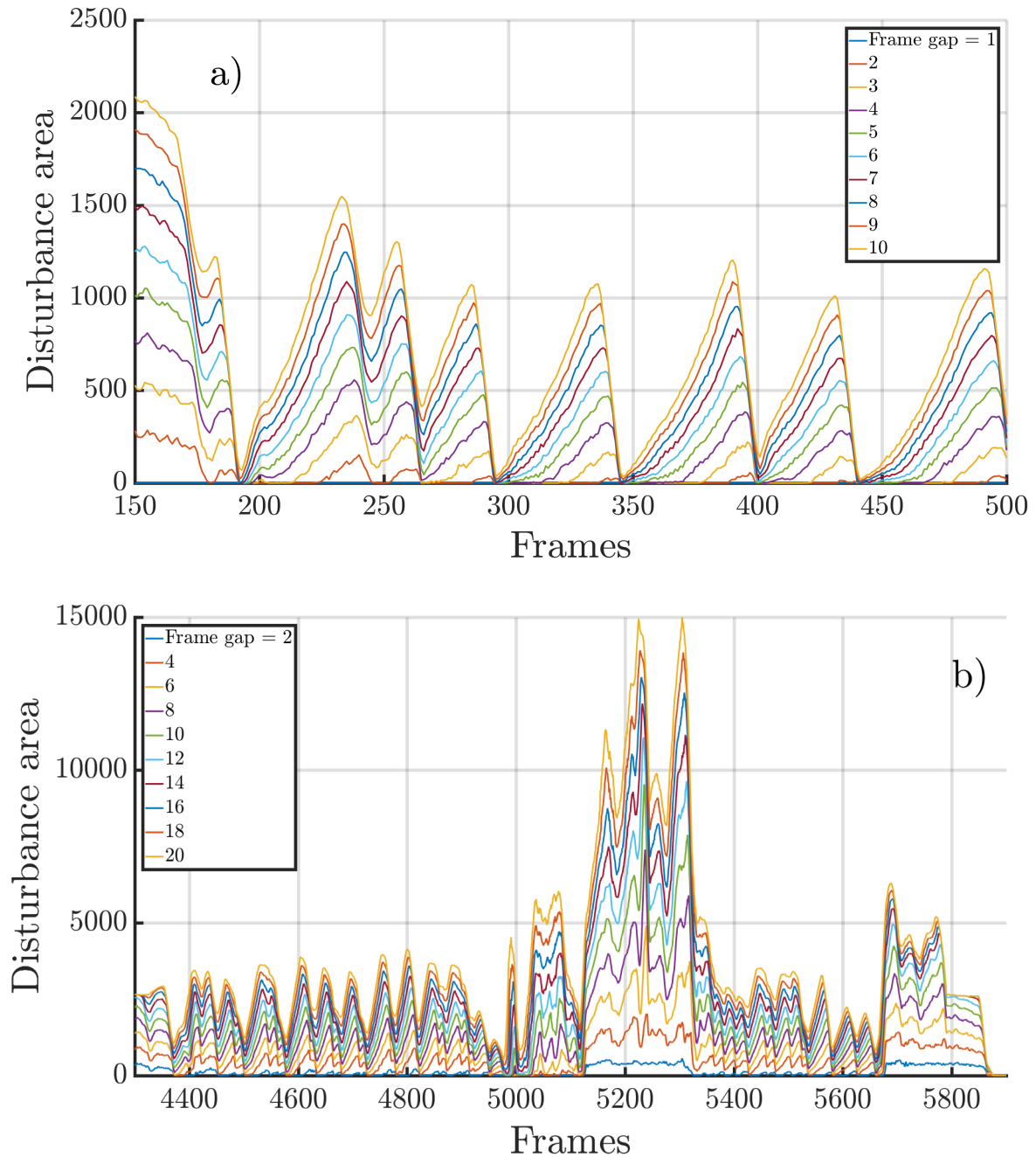
Fig. 6.15 Disturbance area created in the packing by individual particles rolling downhill and colliding with the existing oblique packing at the 15° angle of inclination. (a) In this plot, a particle rolls downhill, collide with a particle in the packing and then roll over one particle after another present at the free surface of the packing. Minima are the events when the rolling particle is in contact with two particles. (b) In the beginning, before frame 5000, the impacting particle is rolling over the free surface of the packing. Between frames 5100 to 5350, a new particle impacts the packing and starts a rare avalanche event (identified by a sudden increase to larger disturbance area), in which the whole top layer slides over the layer below it.
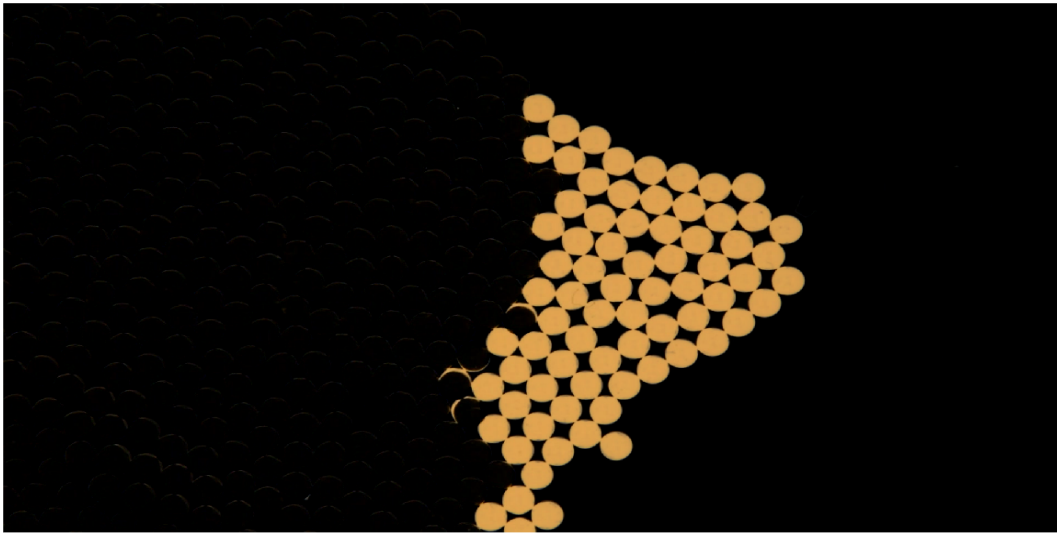
(a)
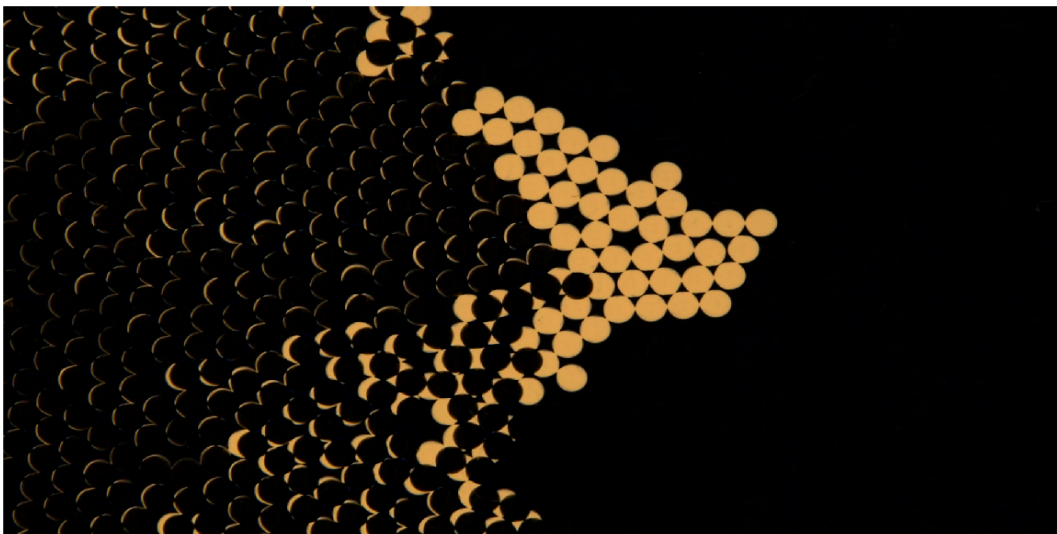
(b)

Fig. 6.16 Effect on the packing after many individual spheres are rolled downhill, one by one, to collide with the existing parallel packing. The image was obtained by taking an absolute difference between the initial packing and the final packing after many impacts. The bright full circles are the newly added particles. (a) Packing at 10° is not affected by individual impacts. (b) Packing at 5° shows many bright regions in the bulk indicating that all the particles in the original packing have undergone some movement as the result of impacts by new particles.

Figure 6.15 (b) shows the rare event of avalanche from frame 5100 to 5350. The avalanche can be as simple as one layer of particles at the free surface sliding over the other layer or it can be a major rearrangement of the first few layers near the free surface. The rearrangement is always followed by one layer sliding over another in an attempt to create hexagonal packing. Other than frames 5100 to 5350, little rearrangements follow the bigger avalanche but most of the area contribution comes from a particle rolling over the inclined free surface. Figure 6.15 (a) can be considered a zoomed-in version of Figure 6.15 (b) at regions far away from frames 5100 to 5350.

We now shift our attention to individual particles colliding with a parallel packing. We were able to obtain parallel packings of different packing fraction by varying the angle of inclination at which the packing was created. By changing the angle of inclination, we effectively changed the Stokes number at which the packing was being created. The Stokes number of individual collisions during the formation of the packing was difficult to determine and therefore we rolled down individual particles to impact the pile.

As discussed before (in Figure 6.2), particles reached terminal velocity before impacting the free surface of the packing. Stokes number St was calculated by using this terminal velocity for different angles of inclination and has been shown in Table 6.1. The St is less than 0.5 for all the angles. We currently do not have data for larger Stokes number ($St > 1$) but based on our understanding of normal collisions from previous chapters we speculate that depending on whether the impacting sphere is above or below the St_c, one would expect the sphere to either settle at the first minimum it encounters or to rebound and choose a deeper minimum. In our present experiments, we encountered only one scenario when a sphere collides with parallel packing. The sphere rolls over the particle it impacts and settles in the first minimum it encounters, in case of parallel packing. This suggests that if there is a critical Stokes number for rolling, our experiments are well below this value.

In parallel packing, if the packing fraction is very low and the particles are delicately packed, one might expect the impacting particles to do some rearrangements and increase the packing fraction. To test this, we took two snapshots one before individual impacts and another after the impacts and took the difference between the two. As can be seen from Figure 6.16 (a) and (b), individual impacts do not affect the packing at $\theta = 10°$ but local rearrangements take place after individual impacts in the packing at 5° angle of inclination. The bright full circles near the free surface in Figure 6.16 (a) and (b) are the new particles which collided with the original packing (in dark). Individual impacts make fragile structures in 5° packing more compact. The change in packing fraction after

a number of individual impacts is approximately 1.3% for packing at 5° whereas it only changes by approximately 0.4% for packing at 10° angle of inclination.

6.6   Discussion

We have developed an experimental protocol to create a disordered packing of monodisperse spheres in a 2D system by allowing particles to deposit at low Stokes number. Every time a new particle is added into the packing, it delivers almost no momentum to the particles beneath and this helps in creating a loose packing. The area-based packing fraction in this method can be decreased by decreasing the inclination angle of the container. By studying the bond orientational order of the packing, we concluded that there are patches of hexagonal ordering in this disordered looking packing. We also observed that there are larger defects or empty regions in packings created at smaller angles of inclination by calculating the probability distribution of Voronoi polygon areas.

The packing fraction was found to increase as we go away from the free surface of the parallel packing, whereas hexagonal ordering remained almost the same throughout the length. We found that an individual particle impacting the oblique packing can either stop at the first minimum it encountered or it can keep on rolling over the particles at the free surface before stopping at some n^{th} minimum. We expect our experiments to be below the critical Stokes number for rolling, as we do not see any rebound of impacting particles. In rare events, we observed that even an individual particle can create an avalanche after colliding with an oblique packing. We speculate that the avalanche event is not governed by momentum transfer, as we are operating at very low Stokes numbers. Therefore, this event points to the fragile nature of the packing as adding a point force is enough to destabilize the surface.

In parallel packing, rearrangements by impacting particles were observed only for small angles of inclination. In the future, one can try to repeat these experiments at larger Stokes number. It will be interesting to see if there indeed exists a critical Stokes number for rolling and how the packing fraction and more importantly the disorderedness of the packing changes while crossing this critical number.

Appendix A

Hertzian calculation

For a perfect normal collision between two smooth, perfectly elastic spheres of radii R_i, masses m_i, Young's modulus E_i, and Poisson ratio ν_i (i=1,2), the closest approach of the spheres during mechanical contact can be calculated by Hertzian theory (Landau and Lifshitz, 1986) and is given by

$$b = \left(\frac{m_{\textit{eff}}}{k}\right)^{2/5} v^{4/5}, \tag{A.1}$$

where b is the maximum overlap of the spheres ($b =$ distance between the centers of the sphere subtracted from $(R_1 + R_2)$) and v is the relative velocity between the spheres just before contact. Here $m_{\textit{eff}}$ is the reduced mass of the spheres and is given by

$$\frac{1}{m_{\textit{eff}}} = \frac{1}{m_1} + \frac{1}{m_2}, \tag{A.2}$$

k is the effective modulus of the spheres, given by

$$k = \frac{4}{5D_0}\sqrt{\frac{R_1 R_2}{R_1 + R_2}}, \tag{A.3}$$

where

$$D_0 = \frac{3}{4}\left(\frac{1 - \nu_1^2}{E_1} + \frac{1 - \nu_2^2}{E_2}\right). \tag{A.4}$$

In our electrical set-up, one of the spheres has been replaced by a plate, so $1/R_2 = 0$ and $1/m_2 = 0$.

For a smooth sphere of diameter 15.4 mm, the depth of the contact formed due to the collision of the sphere with the plate for an impact velocity corresponding to the
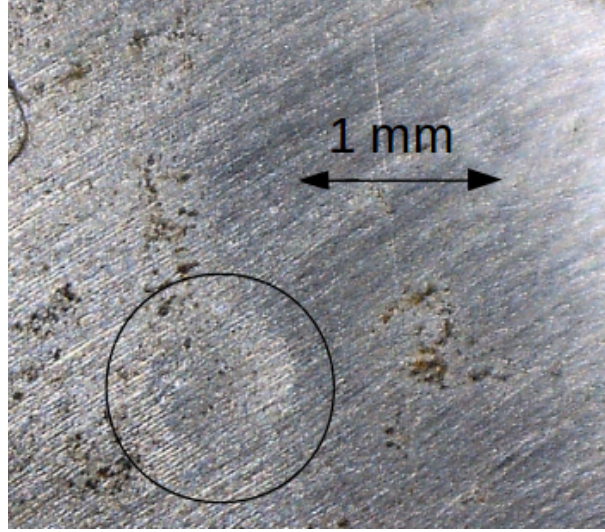
Fig. A.1 Craters are visible inside the marked circle. The sizes of the crater on the plate is around 700 μm for $St = 28$.

velocity for $St = 28$ is ≈ 13.5 μm. The radius of the contact area is then given by

$$a = \sqrt{2Rb}. \tag{A.5}$$

This gives the diameter of the contact area $= 2a \approx 900$ μm. Of course, due to lubrication forces, the actual impact velocity will be much lower, so these calculations considerably over predict the size of the crater made.

A different possibility is that instead of the radius of the sphere setting the geometry of the collision, the local radius of curvature set by the roughness of the sphere is the relevant radius. If the characteristic height of bumps is q and the characteristic lateral size is l, the local radius of curvature will be given by

$$R_{eff} = \frac{1}{2q}\left(\frac{l}{2}\right)^2. \tag{A.6}$$

For $q = 1$ μm and $l = 100$ μm, $R_{eff} = 900$ μm. If we use this radius in Hertzian calculation for collision, we get the depth and radius of the contact area to be ≈ 20 μm and 200 μm, respectively.

At the largest Stokes numbers, we see that the sphere's impact on the plate leaves small craters (Figure A.1) ≈ 700 μm, thus the Hertzian calculation must be replaced by a calculation involving material plasticity. Finally, we recall that all these estimates have

used the Stokes number computed without wall effects, thus the actual impact velocity will be lower. These estimates, therefore, overpredict the size of the region of contact.

References

B. Andreotti, Y. Forterre, and O. Pouliquen. *Granular media: between fluid and solid.* Cambridge University Press, 2013.

R. J. Angel, M. Bujak, J. Zhao, G. D. Gatta, and S. D. Jacobsen. Effective hydrostatic limits of pressure media for high-pressure crystallographic studies. *Journal of Applied Crystallography*, 40(1):26–32, 2007.

J. Ashmore, C. del Pino, and T. Mullin. Cavitation in a lubrication flow between a moving sphere and a boundary. *Phys. Rev. Lett.*, 94(12):124501, 2005.

G. Barnocky and R. H. Davis. Elastohydrodynamic collision and rebound of spheres: experimental verification. *Phys. Fluids*, 31(6):1324, 1988.

G. Barnocky and R. H. Davis. The influence of pressure-dependent density and viscosity on the elastohydrodynamic collision and rebound of two spheres. *Journal of Fluid Mechanics*, 209:501–519, 1989.

J. Bernal and J. Mason. Packing of spheres: co-ordination of randomly packed spheres. *Nature*, 188(4754):910, 1960.

J. G. Berryman. Random close packing of hard spheres and disks. *Physical Review A*, 27 (2):1053, 1983.

Y. Bertho, F. Giorgiutti-Dauphiné, and J.-P. Hulin. Dynamical janssen effect on granular packing with moving walls. *Physical review letters*, 90(14):144301, 2003.

S. K. Birwa, G. Rajalakshmi, R. Govindarajan, and N. Menon. Solid-on-solid contact in a sphere-wall collision in a viscous fluid. *Physical Review Fluids*, 3(4):044302, 2018.

I. Bratberg, K. Måløy, and A. Hansen. Validity of the janssen law in narrow granular columns. *The European Physical Journal E*, 18(3):245–252, 2005.

H. Brenner. The slow motion of a sphere through a viscous fluid towards a plane surface. *Chemical engineering science*, 16(3-4):242–251, 1961.

M. Cates, J. Wittmer, J.-P. Bouchaud, and P. Claudin. Jamming, force chains, and fragile matter. *Physical review letters*, 81(9):1841, 1998.

C. Cawthorn and N. Balmforth. Contact in a viscous fluid. part 1. a falling wedge. *Journal of Fluid Mechanics*, 646:327–338, 2010.

R. Chand, M. A. Khaskheli, A. Qadir, Y. Sandali, and Q. Shi. Influence of spontaneous percolation on apparent mass at the bottom of a janssen granular column. *Physica A: Statistical Mechanics and its Applications*, 393:96–100, 2014.

T. Chastel and A. Mongruel. Squeeze flow between a sphere and a textured wall. *Physics of Fluids*, 28(2):023301, 2016.

P. Chaudhuri, L. Berthier, and S. Sastry. Jamming transitions in amorphous packings of frictionless spheres occur over a continuous range of volume fractions. *Physical review letters*, 104(16):165701, 2010.

R. Y. Chu. Pressure viscosity characteristics of lubricating oils. *J. Inst, Petrol.*, 46(461): 147, 1962.

R. G. Cox and H. Brenner. The slow motion of a sphere through a viscous fluid towards a plane surface—ii small gap widths, including inertial effects. *Chemical Engineering Science*, 22(12):1753–1777, 1967.

B. Dahneke. The capture of aerosol particles by surfaces. *Journal of colloid and interface science*, 37(2):342–353, 1971.

B. Dahneke. The influence of flattening on the adhesion of particles. *Journal of Colloid and Interface Science*, 40(1):1–13, 1972.

B. Dahneke. Measurements of bouncing of small latex spheres. *Journal of Colloid and Interface Science*, 45(3):584–590, 1973.

R. H. Davis. The rate of coagulation of a dilute polydisperse system of sedimenting spheres. *Journal of Fluid Mechanics*, 145:179–199, 1984.

R. H. Davis. Elastohydrodynamic collisions of particles. *PhysicoChem. Hydrodyn.*, 9:41, 1987.

R. H. Davis, J.-M. Serayssol, and E. J. Hinch. The elastohydrodynamic collision of two spheres. *J. Fluid Mech.*, 163:479, 1986.

R. H. Davis, D. A. Rager, and B. T. Good. Elastohydrodynamic rebound of spheres from coated surfaces. *Journal of Fluid Mechanics*, 468:107–119, 2002.

C. Donahue, C. Hrenya, R. Davis, K. Nakagawa, A. Zelinskaya, and G. Joseph. Stokes' cradle: normal three-body collisions between wetted particles. *Journal of Fluid Mechanics*, 650:479–504, 2010.

K. Dong, R. Yang, R. Zou, and A. Yu. Role of interparticle forces in the formation of random loose packing. *Physical review letters*, 96(14):145505, 2006.

D. Dowson and T. Whomes. Paper 8: side-leakage factors for a rigid cylinder lubricated by an isoviscous fluid. In *Proceedings of the Institution of Mechanical Engineers, Conference Proceedings*, volume 181, pages 165–176. SAGE Publications Sage UK: London, England, 1966.

R. Farr, J. R. Melrose, and R. Ball. Kinetic theory of jamming in hard-sphere startup flows. *Physical Review E*, 55(6):7203, 1997.

G. R. Farrell, K. M. Martini, and N. Menon. Loose packings of frictional spheres. *Soft Matter*, 6(13):2925–2930, 2010.

R. C. Flagan and J. H. Seinfeld. *Fundamentals of Air Pollution Engineering*. Prentice-Hall, Inc., 1988.

E. Gal, G. Tardos, and R. Pfeffer. A study of inertial effects in granular bed filtration. *AIChE journal*, 31(7):1093–1104, 1985.

P. Gondret, E. Hallouin, M. Lance, and L. Petit. Experiments on the motion of a solid sphere toward a wall: From viscous dissipation to elastohydrodynamic bouncing. *Phys. Fluids*, 11(9):2803, 1999.

P. Gondret, M. Lance, and L. Petit. Bouncing motion of spherical particles in fluids. *Phys. Fluids*, 14(2):643, 2002.

R. Govindarajan and R. Narasimha. Stability of spatially developing boundary layers in pressure gradients. *Journal of Fluid Mechanics*, 300:117–147, 1995.

A. N. Grubin. Investigation of the contact of machine components. *Central Scientific Research Inst. Tech. & Mech. Eng.*, 1949.

B. Hamrock. Fundamentals of fluid film lubrication. *NASA Reference Publication*, 1255, 1991.

J. Hilton and P. Cleary. Granular flow during hopper discharge. *Physical Review E*, 84 (1):011307, 2011.

H. M. Jaeger and S. R. Nagel. Physics of the granular state. *Science*, 255(5051):1523–1531, 1992.

H. M. Jaeger, S. R. Nagel, and R. P. Behringer. Granular solids, liquids, and gases. *Reviews of modern physics*, 68(4):1259, 1996.

A. Janda, I. Zuriguel, and D. Maza. Flow rate of particles through apertures obtained from self-similar density and velocity profiles. *Physical review letters*, 108(24):248001, 2012.

H. Janssen. Janssen, ha, and z. vereins, 1895, dtsch. eng. 39 (25), 1045. *Dtsch. Eng*, 39: 1045, 1895.

M. Jerkins, M. Schröter, H. L. Swinney, T. J. Senden, M. Saadatfar, and T. Aste. Onset of mechanical stability in random packings of frictional spheres. *Physical review letters*, 101(1):018301, 2008.

G. G. Joseph, R. Zenit, M. L. Hunt, and A. M. Rosenwinkel. Particle–wall collisions in a viscous fluid. *J. Fluid Mech.*, 433:329, 2001.

H. King, R. White, I. Maxwell, and N. Menon. Inelastic impact of a sphere on a massive plane: Nonmonotonic velocity-dependence of the restitution coefficient. *EPL*, 93(1): 14002, 2011.

L. D. Landau and E. M. Lifshitz. *Theory of Elasticity*. Elsevier New York, 1986.

J. W. Landry, G. S. Grest, L. E. Silbert, and S. J. Plimpton. Confined granular packings: structure, stress, and forces. *Physical review E*, 67(4):041303, 2003.

J. W. Landry, G. S. Grest, and S. J. Plimpton. Discrete element simulations of stress distributions in silos: crossover from two to three dimensions. *Powder technology*, 139 (3):233–239, 2004.

L. G. Leal. *Advanced Transport Phenomena: Fluid Mechanics and Convective Transport Processes*. Cambridge University Press, 2007.

N. Lecoq, F. Feuillebois, N. Anthore, R. Anthore, F. Bostel, and C. Petipas. Precise measurement of particle–wall hydrodynamic interactions at low reynolds number using laser interferometry. *Physics of Fluids A: Fluid Dynamics*, 5(1):3–12, 1993.

N. Lecoq, R. Anthore, B. Cichocki, P. Szymczak, and F. Feuillebois. Drag force on a sphere moving towards a corrugated wall. *Journal of Fluid Mechanics*, 513:247–264, 2004.

J. Liu, Q. Shi, X. Liang, L. Yang, and G. Sun. Size dependence of effective mass in granular columns. *Physica A: Statistical Mechanics and its Applications*, 388(4): 379–384, 2009.

F. Löffler. Problems and recent advances in aerosol filtration. *Separation Science and Technology*, 15(3):297–315, 1980.

T. Majmudar, M. Sperl, S. Luding, and R. P. Behringer. Jamming transition in granular systems. *Physical review letters*, 98(5):058001, 2007.

T. S. Majmudar and R. P. Behringer. Contact force measurements and stress-induced anisotropy in granular materials. *Nature*, 435(7045):1079, 2005.

C. Mankoc, A. Janda, R. Arevalo, J. Pastor, I. Zuriguel, A. Garcimartín, and D. Maza. The flow rate of granular materials through an orifice. *Granular Matter*, 9(6):407–414, 2007.

C. Merrigan, S. K. Birwa, S. Tewari, and B. Chakraborty. Ergodicity breaking dynamics of arch collapse. *Physical Review E*, 97(4):040901, 2018.

H. E. Merritt. Worm gear performance. *Proceedings of the Institution of Mechanical Engineers*, 129(1):127–194, 1935.

A. Mongruel. Near-wall hydrodynamic interactions between a settling sphere and a wall. In *Journal of Physics: Conference Series*, volume 392, page 012011. IOP Publishing, 2012.

A. Mongruel, C. Lamriben, S. Yahiaoui, and F. Feuillebois. The approach of a sphere to a wall at finite reynolds number. *Journal of Fluid Mechanics*, 661:229–238, 2010.

R. M. Nedderman. *Statics and kinematics of granular materials*. Cambridge University Press, 2005.

C. S. O'Hern, S. A. Langer, A. J. Liu, and S. R. Nagel. Random packings of frictionless particles. *Physical Review Letters*, 88(7):075507, 2002.

G. Y. Onoda and E. G. Liniger. Random loose packings of uniform spheres and the dilatancy onset. *Physical review letters*, 64(22):2727, 1990.

G. Ovarlez and E. Clément. Elastic medium confined in a column versus the janssen experiment. *The European Physical Journal E*, 16(4):421–438, 2005.

G. Ovarlez, C. Fond, and E. Clément. Overshoot effect in the janssen granular column: a crucial test for granular mechanics. *Physical Review E*, 67(6):060302, 2003.

A. Payatakes and L. Gradoń. Dendritic deposition of aerosol particles in fibrous media by inertial impaction and interception. *Chemical Engineering Science*, 35(5):1083–1096, 1980.

S. Plimpton. Fast parallel algorithms for short-range molecular dynamics. *Journal of computational physics*, 117(1):1–19, 1995.

A. Qadir, H. Guo, X. Liang, Q. Shi, and G. Sun. Effect of the ratios of diameter of silo to bead on the pressure screening in granular columns. *The European Physical Journal E*, 31(3):311–314, 2010.

O. Reynolds. On the theory of lubrication and its application to mr. beauchamp tower's experiments, including an experimental determination of the viscosity of olive oil. *Proc. R. Soc. Lond.*, 40(242-245):191, 1886.

G. Scott and D. Kilgour. The density of random close packing of spheres. *Journal of Physics D: Applied Physics*, 2(6):863, 1969.

N. Shah, S. Birwa, B. Carballo-Ramirez, M. Pleau, N. Easwar, and S. Tewari. Effects of wall friction on flow in a quasi-2d hopper. In *APS Meeting Abstracts*, 2017.

L. E. Silbert, D. Ertaş, G. S. Grest, T. C. Halsey, D. Levine, and S. J. Plimpton. Granular flow down an inclined plane: Bagnold scaling and rheology. *Physical Review E*, 64(5): 051302, 2001.

M. Sperl. Experiments on corn pressure in silo cells–translation and comment of janssen's paper from 1895. *Granular Matter*, 8(2):59–65, 2006.

P. J. Steinhardt, D. R. Nelson, and M. Ronchetti. Bond-orientational order in liquids and glasses. *Physical Review B*, 28(2):784, 1983.

B. P. Tighe and M. Sperl. Pressure and motion of dry sand: translation of hagen's paper from 1852. *Granular Matter*, 9(3-4):141–144, 2007.

L. Vanel and E. Clément. Pressure screening and fluctuations at the bottom of a granular column. *The European Physical Journal B-Condensed Matter and Complex Systems*, 11(3):525–533, 1999.

L. Vanel, P. Claudin, J.-P. Bouchaud, M. Cates, E. Clément, and J. Wittmer. Stresses in silos: comparison between theoretical models and new experiments. *Physical review letters*, 84(7):1439, 2000.

W. M. Visscher and M. Bolsterli. Random packing of equal and unequal spheres in two and three dimensions. *Nature*, 239(5374):504, 1972.

P. Wen, G. Wang, D. Hao, N. Zheng, L. Li, and Q. Shi. Bottom stresses of static packing of granular chains. *Physica A: Statistical Mechanics and its Applications*, 419:457–463, 2015.

F.-L. Yang and M. Hunt. Dynamics of particle-particle collisions in a viscous liquid. *Physics of Fluids*, 18(12):121506, 2006.

L. Yang, J. R. T. Seddon, T. Mullin, C. Del Pino, and J. Ashmore. The motion of a rough particle in a stokes flow adjacent to a boundary. *J. Fluid Mech.*, 557:337, 2006.

R. Zenit and M. L. Hunt. Mechanics of immersed particle collisions. *J. Fluids Eng.*, 121 (1):179, 1999.

Z. Zhang, L. Liu, Y. Yuan, and A. Yu. A simulation study of the effects of dynamic variables on the packing of spheres. *Powder Technology*, 116(1):23–32, 2001.

H. Zhao, X. An, Y. Wu, and Q. Qian. Dem modeling on stress profile and behavior in granular matter. *Powder Technology*, 323:149–154, 2018.